FACULTAD DE CIENCIAS

PONTIFICIA UNIVERSIDAD CATÓLICA DE VALPARAÍSO

IFIS

EX UMBRA IN SOLEM

Thesis submitted for the degree of Doctor of Physical Sciences:

"Numerical and experimental methods to study rheological properties in microfluidic systems"

Author:

Elías Santacruz Yunga

Thesis advisors:

Prof. Claudia Trejo Soto (tutora)

Prof. Eric Plaza Pirela (cotutor)

Valparaíso, Agosto 2025

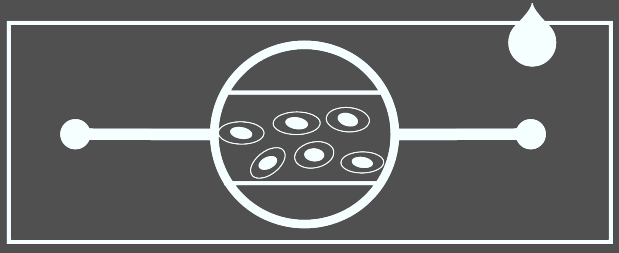

Laboratorio de Biorreología y Microfluídica

CONSTANCIA DE VALIDACIÓN Y CONFIDENCIALIDAD DE MONOGRAFÍA A REPOSITORIO ACADÉMICO

1.- IDENTIFICACIÓN DEL TRABAJO ACADÉMICO

Tipo de monografía (marcar una opción): ☐ Memoria o trabajo de título; ☒ Tesis de Postgrado;

Título del trabajo: Métodos numéricos y experimentales para el estudio de propiedades reológicas en sistemas microfluídicos

Nombre del candidato(a): Elías Jeffersson Santacruz Yunga

Carrera / Grado: Doctorado en Ciencias Físicas

Campus: Casa Central Valparaiso ; **Departamento**: Física

2.- VALIDACIÓN DEL PROFESOR GUÍA/DIRECTOR DE TESIS

Yo, Claudia Andrea Trejo Soto, en mi calidad de profesor(a) guía/director(a) del trabajo académico mencionado anteriormente **DEJO CONSTANCIA** que:

- He revisado esta versión del documento y corresponde a la versión final aprobada del trabajo.
- El trabajo cumple con los requisitos académicos y de formato establecidos por la institución

3.- EVALUACIÓN DE CONFIDENCIALIDAD POR PROPIEDAD INDUSTRIAL

☒ El trabajo **NO contiene información que amerite confidencialidad** y puede ser publicado de inmediato en repositorio con acceso abierto.

☐ El trabajo **CONTIENE** información con potenciales implicancias de propiedad industrial o intelectual y requiere un periodo de confidencialidad (embargo) por:

☐ 6 meses; ☐ 12 meses; ☐ 2 años; ☐ 3 años; ☐ 5 años; ☐ 10 años

Fundamentación de la necesidad de confidencialidad (obligatorio si se solicita embargo):

4.- FIRMAS

Profesor(a) guía o director(a) de memoria o tesis:

Fecha: 08/08/2025 ; **Firma:** _____

Estudiante o Candidato(a):

Fecha: ; **Firma:** _____

Este formulario debe ser insertado como página 2 de la memoria o tesis, completado y firmado por estudiante y profesor(a) antes de la entrega en portal PRISMA de Biblioteca USM.

Laboratorio de Biorreología y Microfluídica, Instituto de Física, Pontificia Universidad Católica de Valparaíso, Av. Universidad 330 (Curauma) - tel: (+56) 32 227 4884 / fax: (+56) 32 227 4886

Página web del laboratorio de Biorreología y Microfluídica:
https://sites.google.com/site/ctrejosoto/home/Laboratory

correo electrónico de autor: elias.santacruz@pucv.cl

Acknowledgments

I thank Prof. Claudia for opening the doors of her laboratory to me, for being attentive to the results with weekly meetings, for always supporting and advising me not only in the academic field, but also Alejandro, who always sends me memes. I thank Prof. Eric, for trusting me since my undergraduate studies, for supporting me to be able to do this graduate course, for allowing me to enter the world of research and for being a great person. I thank Felipe, who since I arrived in Chile helped me in everything I needed, guided me and gave me advice. I thank Aaron, for being a good friend, always willing to help. I thank Pablo and Fran, who made me feel part of their family, always worried about me and never left me alone. I thank my mommy, who always fought to get me ahead, I have no words to thank everything she has done for me, to my daddy who always cared about our welfare. To my grandmother, who continues to give me strength to move forward, even though she is no longer physically with us. Her love and teachings continue to guide my path. And finally, to my best friend and life partner, Diana. Thank you for seeing in me what even I could not see myself, for reminding me who I am when I need it most and for your words that always bring me back to reality. Your unconditional support, your inspiration and your presence in my life are a priceless gift. There are no words to express how grateful I am and how happy it makes me to have you at my side.

Dedicado a:

Mi esposa, mi mami y mi abuelita...

“ El éxito es la suma de pequeños esfuerzos repetidos día tras día.”

Robert Collier

Contents

List of Figures

Abstract

Microfluidic systems have gained significant attention in recent years due to their ability to handle small sample volumes with high precision, making them essential in biomedical, chemical, and materials science applications. A key phenomenon governing microfluidic behavior is surface tension, which plays a critical role in controlling fluid interfaces and droplet formation. This thesis focuses on the study of filling phenomena in microfluidic systems using the Smoothed Particle Hydrodynamics (SPH) method, a mesh-free computational technique well-suited for simulating free-surface flows and multiphase interactions, and validates the numerical results through experimental measurements.

To improve the accuracy of SPH simulations in capturing surface tension effects, we introduce a scalable pair potential model inspired by molecular cohesion forces. The model is calibrated using the Young-Laplace equation and employs a scaling factor that depends on particle resolution and fluid volume. Comparative tests, such as spherization of a fluid cube, free-fall experiments, droplet oscillation, also validated the model against theoretical and experimental results. Simulations are carried out through different levels of discretization to evaluate numerical stability and accuracy.

In addition, the proposed method is applied to microfluidic flow simulations, particularly in microchannel environments where viscosity and interfacial effects play a crucial role. The study aims to improve rheological characterization using microfluidic platforms by integrating computational and experimental approaches. Image-based analysis is employed to track the propagation of the fluid front, allowing accurate determination of viscosity. The impact of flow losses in microchannels is also investigated by minimizing connecting tubes to refine in-channel rheometry methodologies.

The results of this thesis contribute to advancing the design of microfluidic devices and provide a robust numerical framework for modeling surface tension in SPH simulations. This research has broad implications for droplet physics, fluid front dynamics in microchannels, and microfluidic engineering applications.

1 Introduction

In recent decades, numerical simulation has become an essential tool for advancing the study of fluid dynamics [1, 2]. By enabling the analysis of complex and highly dynamic phenomena without the constraints of costly or impractical experiments, computational modeling has expanded the boundaries of scientific and engineering research. Among the various numerical methods available, Smoothed Particle Hydrodynamics (SPH) stands out for its versatility and robustness [3, 4]. Its mesh-free and Lagrangian nature allows SPH to accurately model problems involving free surfaces, large deformations, and multiphase interactions [5–8], making it a promising technique for addressing challenges in areas such as microfluidics, biological fluid simulations, and interfacial phenomena. This chapter provides an overview of Computational Fluid Dynamics (CFD), introduces the SPH methodology, discusses its limitations in surface tension modeling, and presents the motivation for developing improved numerical and experimental strategies to study fluid behavior in microscale systems.

1.1 Computational Fluid Dynamics Overview

Computational Fluid Dynamics (CFD) is a tool that numerically approximates partial differential equations (PDEs) with algebraic equations, allowing for the discretization of both the continuous flow domain and the conservation equations. This computational approach enables numerical experiments to obtain valuable information such as velocity fields, heat and mass transfer, and the chemical reactions involved in various processes. To apply CFD, it is necessary to discretize the continuous flow domain, which can be accomplished using several numerical methods. Among the most important are the finite difference method (FDM), the finite volume method (FVM), and the finite element method (FEM).

The finite difference method (FDM) was the first technique used to obtain numerical solutions to the Navier-Stokes (NS) equations. This method operates in Cartesian coordinates and requires structured meshes. While conceptually simple, FDM presents disadvantages due to its complex implementation in irregular geometries, which limits its application mainly to simple domains. For this reason, its use is less frequent in industrial applications [9].

The finite volume method (FVM) is based on the direct discretization of the conservation equations in their integral form over control volumes, eliminating the need for coordinate transformations. FVM offers a significant advantage because it can handle

both structured and unstructured meshes, making it ideal for simulations involving complex geometries. As a result, FVM is currently the most widely used method in the industry for CFD applications [10].

The finite element method (FEM) is a generalized approach for solving the Navier-Stokes and Euler equations. FEM involves dividing the computational domain into finite elements of regular geometric shapes, such as triangles or quadrilaterals in two-dimensional problems, and tetrahedra or hexahedra in three-dimensional cases. This strategy enables the creation of unstructured meshes, which are particularly useful for simulating complex geometries and non-Newtonian fluids [11].

Various software solutions implement these numerical methods to solve problems in both academic and industrial settings. Commercial examples include ANSYS Fluent, PHOENICS, STAR-CCM+, ADINA-CFD,ConSol, and ABAQUS. In parallel, open-source platforms such as FEniCS, FreeFEM++, OpenFOAM, FREECFD, OpenFVM, and ELMER are widely used in research environments. Additionally, many research centers and universities develop custom codes or improve existing algorithms to meet specific scientific and engineering needs.

In terms of physical description, there are three primary approaches to represent fluid behavior based on the Navier-Stokes equations: the Eulerian, Lagrangian, and Eulerian-Lagrangian or mixed methods. The Eulerian approach evaluates phase properties from one control volume to another within a fixed coordinate system, making it well-suited for studying fluid interactions across defined spatial domains. The Lagrangian approach, by contrast, uses a moving coordinate system where elements are represented as particles, allowing for the direct study of interactions between particles within their domain of influence. Lastly, the mixed or Eulerian-Lagrangian method combines concepts from both frameworks, enabling simulations that involve both continuous phases and dispersed particles [12].

1.2 Smoothed Particle Hydrodynamics (SPH)

Smoothed Particle Hydrodynamics (SPH) is a mesh-free Lagrangian method originally proposed by Lucy [13] and independently by Gingold and Monaghan [14] for simulating astrophysical phenomena such as stellar evolution. SPH discretizes the fluid domain into particles that carry physical properties and move according to conservation equations. This particle-based representation allows SPH to naturally handle large deformations, free surfaces, and complex topological changes, which are challenging for mesh-based methods.

Since its inception, SPH has been adapted and extended to a wide range of problems in fluid dynamics, solid mechanics, and multiphase flows. Its Lagrangian nature facilitates accurate tracking of interfaces and transient phenomena, making it particularly suitable for simulating multiphase flows and fluid-structure interactions [15, 16]. Recent advances have further improved its accuracy, numerical convergence, and stability,

broadening its applicability across engineering and computational sciences [17].

SPH has been employed in various applications such as dam-break problems, free-surface flows, sediment transport, and biological fluid simulations [4]. Yang et al. (2021) [18] highlighted the challenges of using SPH for multiphase flows with large density ratios, a situation often encountered in microfluidic environments where free surfaces and interface dynamics are critical. Despite its numerous advantages, SPH faces difficulties in accurately modeling interfacial phenomena such as surface tension, especially in multiscale simulations where traditional SPH models struggle with resolution dependency and stability.

1.2.1 SPH and Surface Tension Modeling

Surface tension plays a crucial role in microfluidic systems by governing interfacial interactions between fluids. The Young-Laplace model describes surface tension as resulting from a balance of attractive and repulsive forces at a curved fluid interface [19]. Laplace's law relates the pressure difference ΔP across the interface to the surface tension γ and the radius of curvature R:

$$\Delta P = \frac{2\gamma}{R}. \tag{1.1}$$

At the molecular level, surface tension arises due to an imbalance of cohesive forces, with molecules at the surface experiencing fewer neighboring interactions compared to those within the bulk liquid, creating a net inward force. This leads to the minimization of surface area, resulting in characteristic fluid geometries such as droplets and bubbles [20].

Simulating surface tension accurately in SPH remains challenging. Various strategies have been proposed, including Continuum Surface Force (CSF) models [8], pairwise interaction potentials [21, 22], and Lennard-Jones-type potentials [23]. However, many approaches suffer from limitations in accuracy and stability, particularly at multiple scales. Addressing these limitations is crucial for advancing SPH simulations in microfluidics.

In SPH, each phase must be discretized using its own set of particles. However, it has been noted that the conservation of momentum term in SPH can produce an intrinsic surface tension even when two phases have different densities. This intrinsic surface tension occurs with values that are not grounded in physical measurements [24]. To address this, two models have been proposed in SPH to simulate surface tension: Continuum Surface Force (CSF) and Internal Pairwise Force (IPF) models. The CSF model, derived from grid-based numerical methods, requires precise estimation of the interface curvature to represent surface tension adequately. In contrast, the IPF model proves to be more robust, as it is built on a molecular dynamic foundation, considering pairwise interaction forces between particles within a cutoff distance to produce surface tension (See Fig. 1.1 [25–29].

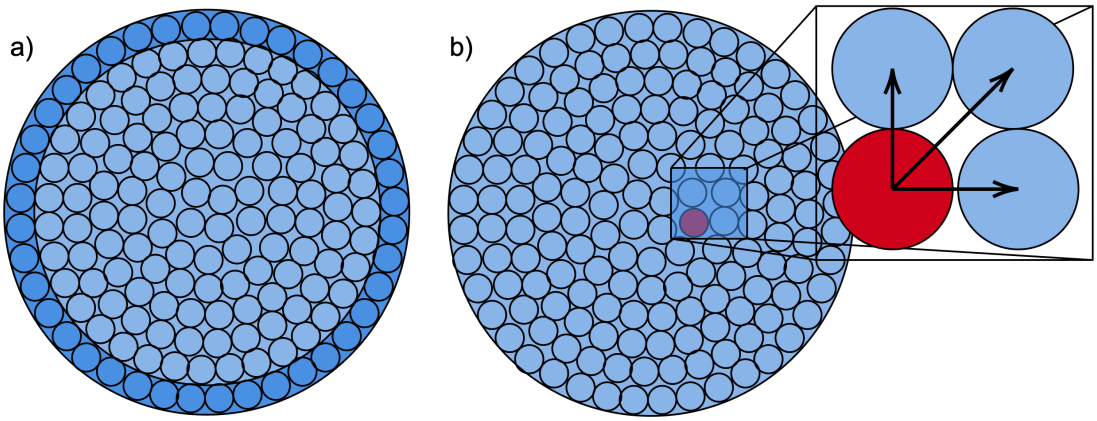

Figure 1.1: a) Representation of how the CSF method works, b) Representation of how the IPF method works.

The work by Tartakovsky and Arai [28, 29] compares and proposes tools for simulation using IPF models. They define a virial pressure, which means that in IPF simulations, the absolute value of the pressure field is the pressure indicated by the equation of state plus the virial pressure, which is always negative. In the work by Howard and Tartakovsky [30], they found a limit of $3\,r_c$ (the r_c cutoff radius in our work) beyond which the pairwise forces term is valid.

These models propose that cohesive forces exist on a macroscopic scale, acting between small fluid volumes. These forces depend on whether the fluid is single-phase or multiphase, on the volume discretization scale, on the type of fluid, on the external pressure, and on the total mass of the simulated fluid element. Currently, there is no universal calibration factor that allows these forces to be applied in SPH simulations across all scenarios.

Morris [31] initially introduced a CSF-based surface tension model in SPH, which was subsequently applied in various studies [7, 32–36]. However, the complexity of the calculations makes it challenging to integrate them into an analytical mechanical framework. In contrast, the IPF model, being energy-based, can be more easily incorporated into such a framework. IPF is suitable for calculating surface tension while maintaining the physical consistency of the discrete particle system [37]. The first IPF model was introduced by Monaghan [5], and Tartakovsky and Meakin proposed a modern implementation of the IPF model in SPH [38], with these derived models being widely used [6, 39, 40].

Additionally, surface tension is fundamental in small-scale free surface problems, where fluid behavior is significantly influenced by internal forces outweighing body forces [41]. The relationship between surface tension and system scale can be charac-

terized by the Bond number, which expresses the ratio of body forces (usually gravity) to surface tension. For droplets with small Bond numbers, rupture or separation is unlikely, as the influence of gravity is much weaker compared to surface tension, even under normal gravity conditions [42].

1.3 Microfluidics

Microfluidic systems have experienced rapid advancements over the past decade, particularly in the fields of engineering, science, and technology, due to their numerous advantages. One of their most critical benefits is the ability to work with extremely small sample volumes, which is invaluable in applications where sample availability is limited, such as clinical diagnostics or pharmaceutical research [43, 44]. Additionally, microfluidic systems are renowned for their simplicity in fabrication and operation, contributing to their accessibility and versatility across various disciplines.

A distinctive advantage of microfluidics is its ability to achieve precise control over fluid behavior at microscopic scales. This precision enables the study of phenomena such as laminar flow, droplet formation, and particle manipulation within confined geometries—phenomena difficult to observe at the macroscale [45]. For instance, laminar flow in microchannels ensures that mixing occurs predominantly through diffusion, allowing precise control of chemical reactions and the creation of concentration gradients essential for biological studies [46].

Microfluidic experiments often focus on droplet-based systems, where individual droplets serve as isolated microreactors. These systems enable high-throughput screening for applications like drug discovery, allowing thousands of reactions to be conducted in parallel [47]. Droplet-based microfluidics has been particularly effective in performing single-cell analysis, encapsulating individual cells within droplets to investigate their response to various stimuli [48]. It has also been applied in genetic analysis and the study of rare biological events.

Another prominent area of experimentation is the manipulation of fluids using external forces such as electric fields, magnetic fields, or acoustic waves. Techniques like electrokinetics and magnetophoresis enable precise control over the movement and separation of particles or cells within microchannels, contributing to the development of lab-on-a-chip devices capable of complex tasks such as cell sorting, DNA extraction, and pathogen detection [49].

Experiments in microfluidics also extend to the study of multiphase flows, where two or more immiscible fluids interact within confined spaces. These studies are crucial for understanding surface tension, interfacial dynamics, and emulsion formation [50]. Moreover, advanced imaging and analytical techniques have been integrated with microfluidics, enabling real-time monitoring and quantification of fluid behavior at the microscale [51]. This combination has facilitated sophisticated experiments such as tracking cell migration in response to chemical gradients and visualizing microbubble

formation in controlled environments.

Microfluidic platforms have also been used to investigate blood rheology by analyzing the mechanical properties of red blood cell membranes [52]. These techniques have provided insights into blood behavior under pathological conditions such as β-thalassemia and iron deficiency, using front microrheometry [53]. Viscosity normalization according to hematocrit and shear rate has been explored, offering valuable data for biomedical applications [54].

1.4 Numerical Simulations and Microfluidics

Understanding and predicting fluid behavior at microscopic scales is essential for advancing scientific and industrial applications. Processes such as biological fluid transport [55], inkjet printing [56], and aerosol formation [57] involve complex fluid interactions that are difficult to study experimentally. In microfluidics, where confinement effects, multiphase flows, and interfacial phenomena are dominant, traditional numerical methods often struggle to provide accurate and stable predictions [58, 59]. Therefore, robust and versatile computational techniques are required to complement experimental observations and guide device design.

Smoothed Particle Hydrodynamics (SPH) has emerged as a powerful tool for simulating microfluidic systems due to its mesh-free Lagrangian nature [4, 14, 60, 61]. Unlike mesh-based approaches, SPH represents fluids as discrete particles that move and interact according to conservation laws. This formulation makes SPH particularly suitable for capturing free surfaces, large deformations, and multiphase flows, all of which are central to microfluidic phenomena [2, 16, 62].

In the context of microfluidics, SPH has been successfully applied to simulate droplet generation, coalescence, and coating flows in microchannels. For instance, Sibilla et al. (2020) [63] modeled a microfluidic device for the conformal coating of pancreatic islets using SPH multiphase formulations, validating their results against experimental data. This study demonstrated the potential of SPH in capturing detailed microfluidic behaviors, including particle-level interactions and interface dynamics. Its Lagrangian framework allows for natural tracking of fluid interfaces and avoids the numerical diffusion often associated with Eulerian methods. Furthermore, SPH facilitates the modeling of complex geometries common in microfabricated devices without the need for remeshing, making it highly adaptable to microfluidic applications.

Despite these advantages, applying SPH to microfluidics presents unique challenges. Microfluidic systems typically operate under low Reynolds numbers, where viscous forces dominate, and capillary effects govern flow behavior. Accurate reproduction of flow profiles, pressure gradients, and wall interactions requires careful calibration of the numerical scheme, including boundary conditions, particle resolution, and viscosity modeling. Additionally, the small scale of microfluidic systems demands high computational accuracy to capture subtle interfacial effects and shear-dependent flow

properties.

This thesis uses SPH to simulate flow behavior in microchannels while modeling surface tension, focusing on the accurate reproduction of rheological properties such as viscosity and shear rate under confined conditions. A novel scalable pair potential model is implemented to enhance the representation of cohesive interactions within fluid elements, facilitating the study of fluids in microfluidic environments. The model aims to capture the essential dynamics of microscale flows, enabling detailed investigations into pressure-driven flows, droplet transport, and front propagation in rectangular channels.

By integrating SPH with experimental methodologies, this research seeks to validate simulation results against real microfluidic experiments, establishing a reliable computational framework for the design and analysis of next-generation microfluidic devices.

1.5 Objectives and Thesis Structure

1.5.1 Objectives

The primary objective of this thesis is:

"To develop and validate a pairwise interaction force model using the Smoothed Particle Hydrodynamics (SPH) methodology, capable of accurately simulating fluid surface tension, and to apply this model in microchannel simulations to extract relevant physical and rheological properties of fluids."

The specific objectives derived from this goal are:

1. To develop a pairwise interaction force model within the SPH framework to accurately simulate surface tension effects in multiphase flows.

2. To validate the proposed interaction model through a series of benchmark tests, including droplet spherization, pendant drop tests, and oscillation analyses, comparing results with theoretical and experimental data.

3. To integrate and optimize the validated model for the simulation of fluid behavior in microfluidic environments, focusing on realistic boundary conditions and interfacial dynamics.

4. To perform microfluidic simulations to analyze rheological properties such as viscosity, surface tension, and energy dissipation, and assess the model's applicability to experimental microfluidic flows.

5. To compare simulation results with experimental observations obtained from microchannel experiments to validate the applicability of the proposed model in real-world microfluidic conditions.

1.5.2 Thesis Structure

This thesis introduces a scalable pair potential into the SPH framework to model cohesive forces within droplets and simulate surface tension across different fluids and discretization scales. Chapter I presents the motivation, research background, and objectives of the study. Chapter II provides the theoretical foundations necessary to understand fluid behavior, interfacial physics, and the Smoothed Particle Hydrodynamics (SPH) methodology. Chapter III details the implementation of the SPH simulation code, including numerical techniques and computational optimizations, building on the pair potential proposed by Wang et al. [23] to model surface tension under various conditions. Chapter IV describes the formulation and implementation of the internal force model that emulates fluid cohesion, presenting the validation process through various benchmark tests such as droplet spherization, oscillation analysis, and droplet deposition. Chapter V presents and analyzes microfluidic simulations, comparing them with theoretical and experimental results to evaluate the accuracy of the proposed SPH-based model in the simulation of microfluidic flows and interfacial interactions. Chapter VI focuses on the application of the developed model in experimental microfluidic systems. It includes experimental procedures for channel fabrication, front detection via image processing, and validation of the simulation model using experimental data.

This research contributes a novel scalable methodology for surface tension modeling in SPH, improving its integration with experimental microfluidic data and providing a concrete advancement in numerical rheometry and microscale flow simulations. The outcomes of this work are expected to enhance the design and analysis of microfluidic devices, with applications extending to biomedical engineering, droplet dynamics, and advanced fluid simulations.

2 Theoretical Background

2.1 Transport Phenomena

To understand the basis for the study of fluid dynamics, it is essential to discuss a general equation that describes the transport of a physical quantity Φ (e.g., mass, momentum, or energy) within a control volume. This equation captures the rate of change of Φ per unit time and volume and is commonly referred to as the equation of transport phenomena [64, 65].

The quantity Φ represents the total amount of the property of interest within a control volume, while ϕ is the specific property per unit mass, expressed as $\phi = \frac{\Phi}{M}$, where (M) is the mass of the control volume. The mass M itself is given by $M = \rho V$, with ρ representing the fluid density and V the size of the control volume. The general form of the transport phenomena equation is expressed as:

$$\frac{\partial}{\partial t}(\rho\phi) = -\nabla \cdot (\rho\phi\mathbf{v}) - \nabla \cdot (J_\phi) + S_\phi \tag{2.1}$$

In this equation, $\frac{\partial}{\partial t}(\rho\phi)$ represents the unsteady accumulation term, describing the rate of change of Φ within the control volume over time. The term $-\nabla \cdot (\rho\phi\mathbf{v})$ captures the convective transport of Φ, which quantifies the net movement of the property due to the bulk motion of the fluid. The molecular transport term, $-\nabla \cdot (J_\phi)$, describes the flux of Φ driven by microscopic mechanisms such as diffusion or heat conduction, with J_ϕ representing the flux vector. Finally, S_ϕ accounts for any internal generation or destruction of Φ within the control volume, such as heat generation by chemical reactions or energy dissipation due to viscous effects.

The equation of transport phenomena (Eq. 2.1) provides a unified framework for analyzing the behavior of fluid systems. Each term in the equation can be derived from the fundamental conservation laws:

- **Mass Conservation:** Governed by the continuity equation.
- **Momentum Conservation:** Derived directly from Newton's Second Law applied to a fluid element.
- **Energy Conservation:** Represented by the first law of thermodynamics applied to a control volume.

Fig. 2.1 illustrates a control volume where transport processes take place. It depicts the interaction of convective transport, molecular diffusion, and source terms that collectively govern the evolution of Φ as it passes through the system.

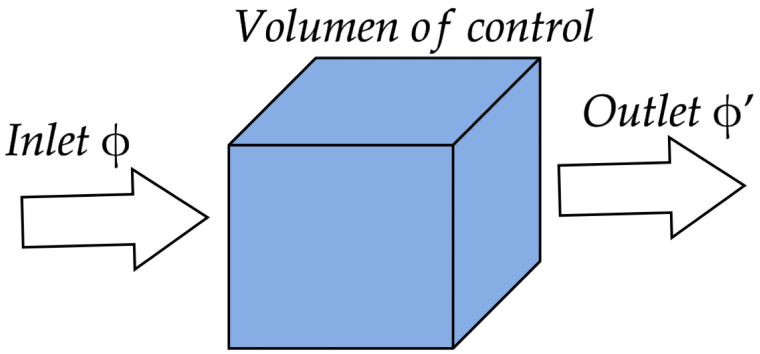

Figure 2.1: Diagram illustrating the transformation of Φ inside a control volume, where the inlet value Φ changes to Φ' at the outlet as a result of transport processes.

In this thesis, we will focus exclusively on the conservation of mass and momentum, as our simulations and experiments are conducted under constant pressure and temperature conditions. The assumption of constant thermodynamic properties simplifies the analysis by allowing us to omit energy conservation equations, thereby concentrating on the fluid's dynamic behavior.

2.2 Continuity Equation

In the specific case of isothermal fluids, where the temperature remains constant throughout the system, we focus on analyzing how mass changes per unit time and volume within a control volume. For this scenario, the conserved quantity Φ corresponds to the mass M. By applying the equation $\left(\phi = \frac{\Phi}{M}\right)$, which defines the specific quantity ϕ as the total quantity Φ divided by the mass of the control volume, we find that:

$$\phi = 1$$

This simplification leads to a more explicit expression for the transport of mass. Substituting $\phi = 1$ into Eq. 2.1, we derive the general equation for the change in mass per unit time and volume:

$$\frac{\partial}{\partial t}(\rho) = -\nabla \cdot (\rho \mathbf{v}) - \nabla \cdot (J) + S \tag{2.2}$$

where ρ is the density of the fluid, $\mathbf{v}$ represents the velocity vector, J denotes the molecular flux due to particle collisions, and S accounts for any internal generation or destruction of mass [65, 66].

In this case, the principle of mass conservation dictates that there is no molecular transport due to particle collisions ($J = 0$) and no internal generation or destruction of mass ($S = 0$). These assumptions are valid for the study of continuous, incompressible isothermal fluids, as there are no sources or sinks of mass within the control volume. Consequently, the transport equation simplifies to the fundamental conservation of mass equation:

$$\frac{\partial}{\partial t}(\rho) = -\nabla \cdot (\rho \mathbf{v}) \tag{2.3}$$

Eq. 2.3 describes the principle of mass conservation, stating that any change in density within the control volume must be exactly balanced by the net flux of mass entering or leaving the volume. This is a cornerstone of fluid dynamics and is particularly relevant in the analysis of incompressible fluids, where the density ρ remains constant, further simplifying the equation to:

$$\nabla \cdot \mathbf{v} = 0.$$

This condition, known as the incompressibility condition, implies that the divergence of the velocity field is zero, signifying that the volume of fluid elements remains unchanged during flow [67].

2.3 Momentum Conservation

The conservation of momentum in fluid dynamics is derived from the general transport equation (Eq 2.1), considering momentum as the conserved quantity, defined as $p = M\mathbf{v}$, where M is the mass and $\mathbf{v}$ is the velocity vector. Consequently, the specific quantity ϕ is $\mathbf{v}$. Substituting this into the general transport equation yields the momentum conservation equation:

$$\frac{\partial}{\partial t}(\rho \mathbf{v}) = -\nabla \cdot (\rho \mathbf{v}\mathbf{v}) - \nabla \cdot (J_{\mathbf{v}}) + S_{\mathbf{v}} \tag{2.4}$$

where ρ is the fluid density, $-\nabla \cdot (\rho \mathbf{v}\mathbf{v})$ represents the convective transport of momentum due to the bulk motion of the fluid, $-\nabla \cdot (J_{\mathbf{v}})$ accounts for molecular momentum flux due to viscosity, and $S_{\mathbf{v}}$ represents external forces per unit volume acting on the system, such as gravitational forces [67, 68].

To analyze the term $-\nabla \cdot (J_{\mathbf{v}})$, we examine the forces acting on an infinitesimal fluid element, as shown in Fig. 2.2.

The force due to hydrostatic pressure acts perpendicular to the face x_1, while shear forces (due to friction) act in all directions. The force per unit area T_1 on face x_1 can

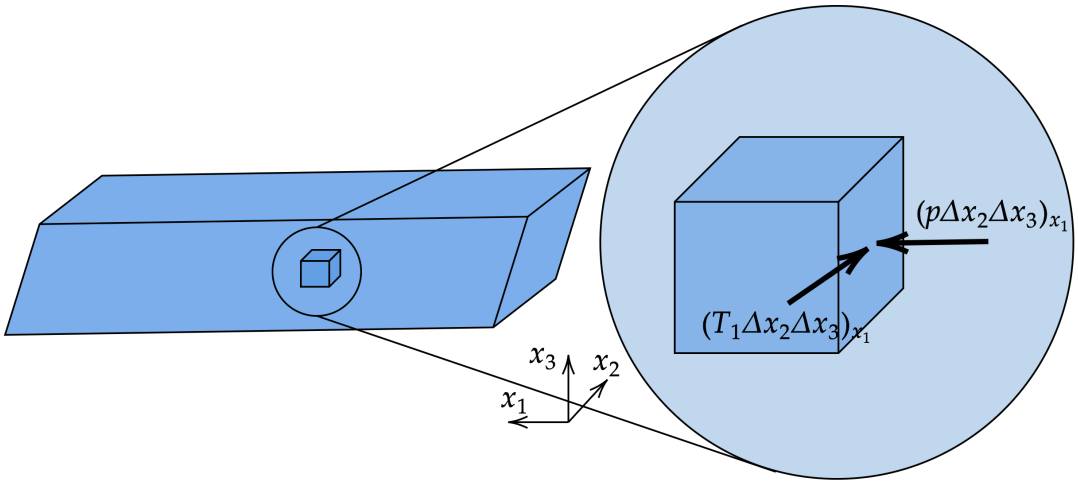

Figure 2.2: Schematic representation of an infinitesimal control volume within a fluid domain. The diagram illustrates the control volume with dimensions Δx_1, Δx_2, and Δx_3, highlighting the normal stress component T_1 and the pressure force p acting on the face perpendicular to the x_1 direction.

be decomposed as $T_1 = \tau_{11}\hat{i} + \tau_{12}\hat{j} + \tau_{13}\hat{k}$, where $\hat{i}, \hat{j}, \hat{k}$ are the unit vectors along the coordinate axes. Therefore, the net force per unit volume on face x_1 is:

$$\frac{F}{\Delta V} = \frac{\partial P}{\partial x_1}\hat{i} - \left(\frac{\partial \tau_{11}}{\partial x_1}\hat{i} + \frac{\partial \tau_{12}}{\partial x_1}\hat{j} + \frac{\partial \tau_{13}}{\partial x_1}\hat{k}\right) \tag{2.5}$$

For all the faces of the control element, the force per unit volume becomes:

$$\frac{F}{\Delta V} = \left(\frac{\partial}{\partial x_1}, \frac{\partial}{\partial x_2}, \frac{\partial}{\partial x_3}\right)\rho - \left(\frac{\partial}{\partial x_1}, \frac{\partial}{\partial x_2}, \frac{\partial}{\partial x_3}\right)\begin{pmatrix}\tau_{11} & \tau_{12} & \tau_{13}\\ \tau_{21} & \tau_{22} & \tau_{23}\\ \tau_{31} & \tau_{32} & \tau_{33}\end{pmatrix} \tag{2.6}$$

$$-\nabla \cdot (J_{\mathbf{v}}) = \frac{F}{\Delta V} = -\nabla p - \nabla \cdot \tau \tag{2.7}$$

Substituting Eq. 2.7 into Eq. 2.4 and noting that $S_{\mathbf{v}}$ is related to external forces per unit time and volume acting on the system (ρf), we obtain:

$$\frac{\partial}{\partial t}(\rho \mathbf{v}) = -\nabla \cdot (\rho \mathbf{v}\mathbf{v}) - \nabla p - \nabla \cdot \tau + \rho f \tag{2.8}$$

2.4 Newtonian Fluids

Newtonian fluids are characterized by a linear relationship between the shear stress and the strain rate. This behavior is mathematically represented by the stress tensor

derived by Stokes, which depends on the velocity gradient $\tau = f\left(\frac{\partial \mathbf{v}}{\partial x_i}\right)$. For an isotropic Newtonian fluid, the stress tensor is given by Eq. 2.9 [64, 65]:

$$\tau_{ij} = -\eta\left(\frac{\partial v_j}{\partial x_i} + \frac{\partial v_i}{\partial x_j}\right) + \left(\frac{2}{3}\eta - k\right)(\nabla \cdot \mathbf{v})\,\delta_{ij} \tag{2.9}$$

In this equation η represents the dynamic viscosity of the fluid, which quantifies the fluid's resistance to shear deformation, k is the bulk viscosity, associated with the resistance to volumetric deformation, and δ_{ij} is the Kronecker delta, ensuring the isotropy of the stress tensor.

The indices i and j denote the direction of the applied force and the normal direction of the fluid face, respectively. The first term in Eq. 2.9 corresponds to the shear stress due to velocity gradients, while the second term accounts for the effects of compressibility.

In the case of incompressible flows, where the density ρ, dynamic viscosity η, and volumetric viscosity k remain constant, the continuity equation imposes the condition of mass conservation:

$$\nabla \cdot \mathbf{v} = 0 \tag{2.10}$$

Substituting this condition into Eq. 2.9, the stress tensor simplifies to:

$$\tau_{ij} = -\eta\left(\frac{\partial v_j}{\partial x_i} + \frac{\partial v_i}{\partial x_j}\right) \tag{2.11}$$

This reduced form highlights that the stress tensor is entirely determined by the velocity gradients and the fluid's viscosity. In matrix form, it can be written as:

$$\tau = -\eta\begin{pmatrix} 2\frac{\partial v_1}{\partial x_1} & \frac{\partial v_2}{\partial x_1} + \frac{\partial v_1}{\partial x_2} & \frac{\partial v_3}{\partial x_1} + \frac{\partial v_1}{\partial x_3} \\ \frac{\partial v_1}{\partial x_2} + \frac{\partial v_2}{\partial x_1} & 2\frac{\partial v_2}{\partial x_2} & \frac{\partial v_3}{\partial x_2} + \frac{\partial v_2}{\partial x_3} \\ \frac{\partial v_1}{\partial x_3} + \frac{\partial v_3}{\partial x_1} & \frac{\partial v_2}{\partial x_3} + \frac{\partial v_3}{\partial x_2} & 2\frac{\partial v_3}{\partial x_3} \end{pmatrix} = -\eta(\nabla \mathbf{v} + \nabla \mathbf{v}^T) \tag{2.12}$$

The divergence of the stress tensor is a key term in the Navier-Stokes equations. By calculating the divergence of Eq. 2.11, we obtain:

$$\nabla \cdot \tau = -\eta \nabla^2 \mathbf{v} \tag{2.13}$$

This result indicates that the stress tensor divergence for a Newtonian fluid depends on the Laplacian of the velocity field, with the dynamic viscosity μ as the proportionality constant.

The Navier-Stokes equations describe the motion of a Newtonian fluid by combining the conservation of momentum with the stress tensor divergence. Using the material derivative $\frac{D}{Dt}$, the momentum conservation equation is expressed as:

$$\rho\frac{D\mathbf{v}}{Dt} = -\nabla p + \nabla \cdot \tau + \rho \mathbf{f} \tag{2.14}$$

Substituting Eq. 2.13 into Eq. 2.14, the Navier-Stokes equation for incompressible flows becomes:

$$\rho \frac{D\mathbf{v}}{Dt} = -\nabla p + \eta \nabla^2 \mathbf{v} + \rho \mathbf{f} \tag{2.15}$$

Here, ρ is the fluid density, p is the pressure field, $\mathbf{f}$ represents body forces acting on the fluid (e.g., gravity).

The Navier-Stokes equation encapsulates the balance of inertial forces, pressure gradients, viscous forces, and external body forces, providing a comprehensive description of fluid motion in various engineering and scientific applications [68, 69].

2.5 Newtonian Shear Rate

The shear rate is a fundamental quantity in fluid dynamics, describing the rate at which adjacent layers of fluid move with respect to each other. It plays a critical role in understanding flow characteristics in microfluidic systems, non-Newtonian fluids, and other domains of fluid mechanics [68, 70]. Starting from the Navier-Stokes equation, under the assumptions of negligible external forces and a steady-state flow, the Stokes equation can be derived as follows [64]:

$$\eta \nabla^2 \mathbf{v} = \nabla P \tag{2.16}$$

where η is the dynamic viscosity of the fluid, $\mathbf{v}$ is the velocity vector and ∇P is the pressure gradient driving the flow.

By solving this differential equation and applying the boundary conditions $\mathbf{v}(b/2) = \mathbf{v}(-b/2) = 0$ (no-slip condition at the channel walls), the velocity profile is obtained:

$$\mathbf{v}(y) = \frac{1}{2} \frac{\nabla P}{\eta} \left(\left(\frac{b}{2} \right)^2 - y^2 \right) \tag{2.17}$$

This parabolic velocity profile is characteristic of laminar flow in rectangular channels [71]. The shear rate, which quantifies the rate of deformation of the fluid layers, is defined as:

$$\dot{\gamma} = \frac{\delta \mathbf{v}}{\delta y} \tag{2.18}$$

By substituting the velocity profile from Eq. 2.17 into Eq. 2.18, the shear rate is determined:

$$\dot{\gamma} = \frac{(\nabla P)\, b}{2\eta} \tag{2.19}$$

To relate this to the flow rate Q, we note that the flow rate is defined as the integral of the velocity profile across the cross-sectional area of the channel:

$$Q = \int_{-b/2}^{b/2} \mathbf{v}(y) \cdot d\mathbf{A} \tag{2.20}$$

Substituting the velocity profile from Eq. 2.17 into Eq. 2.20 and performing the integration yields [70]:

$$Q = \frac{1}{12} \left(\frac{wb^3}{\eta} \right) \nabla P \tag{2.21}$$

where w is the width of the channel and b is the height. Combining Eq. 2.19 and Eq. 2.21, we establish a direct relationship between the shear rate and the flow rate:

$$\dot{\gamma} = 6 \frac{Q}{wb^2} \tag{2.22}$$

In scenarios where the velocity is assumed to be uniform across the channel section (a simplification often used in practical calculations), the flow rate can be expressed as $Q = ||\vec{v}||A$, where A is the cross-sectional area. Substituting this into Eq. 2.22 gives the expression for the average shear rate in the channel:

$$\dot{\gamma} = 6 \frac{||\mathbf{v}||}{b} \tag{2.23}$$

2.6 Non-Newtonian Fluids

Non-Newtonian fluids exhibit a nonlinear relationship between shear stress and strain rate, deviating from the classical Newtonian behavior [72]. Unlike Newtonian fluids, whose viscosity remains constant regardless of the applied shear rate, non-Newtonian fluids display a wide range of behaviors depending on the flow conditions. These fluids are widely encountered in industrial applications, biological systems, and natural phenomena, making their study essential in fluid mechanics and engineering.

Non-Newtonian fluids can be categorized into different types based on their rheological properties:

- **Shear-thinning fluids:** Also known as pseudoplastic fluids, shear-thinning fluids experience a decrease in viscosity with an increase in shear rate. This behavior is commonly observed in polymer solutions, paints, and biological fluids such as blood [73]. Shear-thinning behavior allows these fluids to flow more easily under applied stress, making them useful in applications such as inkjet printing, lubrication, and biomedical diagnostics.

- **Shear-thickening fluids:** In contrast to shear-thinning fluids, shear-thickening (or dilatant) fluids exhibit an increase in viscosity when subjected to higher shear

rates. This behavior is observed in suspensions such as cornstarch in water, wet sand, and certain industrial slurries [74]. Shear-thickening properties are utilized in the design of impact-resistant materials, protective gear, and advanced coatings.

- **Bingham plastics:** These fluids possess a yield stress, meaning that they behave as a solid until the applied shear stress exceeds a critical threshold, after which they flow like a viscous liquid [75]. Examples include toothpaste, mud, and some food products such as ketchup. The ability to resist deformation under low stress makes Bingham plastics ideal for applications requiring controlled flow, such as in construction materials and drilling fluids.

- **Viscoelastic fluids:** These fluids exhibit both viscous and elastic properties, depending on the timescale of deformation. Under slow deformations, they behave like viscous fluids, while under rapid deformations, they exhibit elastic behavior [72]. Viscoelasticity is commonly observed in polymer melts, biological fluids like mucus, and synthetic gels. This property is crucial in applications such as biomedical implants, soft robotics, and rheological modifiers in consumer products.

The classification and understanding of non-Newtonian fluids are essential for designing efficient industrial processes, developing novel materials, and optimizing biomedical applications. Advanced rheological models are often employed to describe their complex behavior, allowing for better predictions and control of their flow properties.

2.6.1 Viscosity Models

The viscosity of non-Newtonian fluids is described by various models that characterize their flow behavior under different shear conditions. These models are fundamental for predicting and analyzing the behavior of complex fluids in both engineering and biomedical applications. Before introducing these models, it is essential to define the scalar shear rate ($\dot{\gamma}$) in terms of the strain rate tensor ($\dot{\varepsilon}$), particularly when addressing complex flow scenarios. The rate of strain tensor is given by:

$$\dot{\varepsilon} = \frac{1}{2}\left(\nabla \mathbf{v} + \nabla \mathbf{v}^T\right) \tag{2.24}$$

where $\nabla \mathbf{v}$ is the velocity gradient tensor, and $\nabla \mathbf{v}^T$ is its transpose. This symmetric tensor represents the local deformation rates of fluid elements.

The magnitude of the shear rate $\dot{\gamma}$ is then computed using the second invariant of $\dot{\varepsilon}$, defined as:

$$\dot{\gamma} = \alpha\sqrt{\dot{\varepsilon} : \dot{\varepsilon}} \tag{2.25}$$

where ":" denotes the double contraction (inner product) of the tensor with itself, and α is a scaling constant, often taken as $\sqrt{2}$ to ensure consistency with simple shear flow definitions. Explicitly, the double contraction is computed as:

$$\dot{\varepsilon} : \dot{\varepsilon} = \sum_{i,j} \dot{\varepsilon}_{ij} \dot{\varepsilon}_{ij} \tag{2.26}$$

This scalar quantity $\dot{\gamma}$ provides a measure of the overall rate of deformation in the fluid and is used in generalized Newtonian models to relate shear stress and viscosity [76].

- **Power-Law Model:** Also known as the Ostwald–de Waele relationship, this model expresses the shear stress (τ) as a function of the shear rate ($\dot{\gamma}$):

$$\tau = K\dot{\gamma}^n \tag{2.27}$$

  Here, K is the consistency index, indicating the fluid's apparent viscosity, and n is the flow behavior index. For $n < 1$, the fluid exhibits shear-thinning behavior (pseudoplastic), while $n > 1$ corresponds to shear-thickening behavior (dilatant). When $n = 1$, the fluid behaves as a Newtonian fluid with constant viscosity. The power-law model is widely used due to its simplicity; however, it is valid over a limited range of shear rates and may not accurately predict viscosity at very low or high shear rates [76].

- **Herschel-Bulkley Model:** This model extends the power-law model by incorporating a yield stress (τ_0), representing the stress required to initiate flow:

$$\tau = \tau_0 + K\dot{\gamma}^n \tag{2.28}$$

  The Herschel-Bulkley model effectively describes viscoplastic fluids that behave as solids under low stress conditions and flow as liquids when the applied stress exceeds the yield stress. It is commonly applied to materials like toothpaste and certain clays [77].

- **Carreau-Yasuda Model:** This model provides a more comprehensive description of non-Newtonian behavior across a wide range of shear rates:

$$\eta(\dot{\gamma}) = \eta_\infty + (\eta_0 - \eta_\infty)\left[1 + (\lambda\dot{\gamma})^a\right]^{(n-1)/a} \tag{2.29}$$

  In this equation, $\eta(\dot{\gamma})$ is the shear-rate-dependent viscosity, η_0 and η_∞ are the zero-shear-rate and infinite-shear-rate viscosities, respectively, λ is a time constant, a is a dimensionless parameter, and n is the power-law index. The Carreau-Yasuda model is particularly useful for modeling polymer solutions and biological fluids, capturing both shear-thinning and Newtonian plateaus at low and high shear rates [72].

- **Cross Model:** Similar to the Carreau-Yasuda model, the Cross model describes the transition from Newtonian behavior at low shear rates to non-Newtonian behavior at higher shear rates:

$$\eta(\dot{\gamma}) = \eta_\infty + \frac{\eta_0 - \eta_\infty}{1 + (\lambda\dot{\gamma})^m} \tag{2.30}$$

  Here, m is a dimensionless parameter that influences the rate of transition between the two viscosity plateaus. The Cross model is often applied to characterize the flow behavior of various non-Newtonian fluids, including polymer melts and suspensions [78].

We will focus on the power-law model to describe the viscosity behavior of the studied fluids. This model provides a straightforward representation of non-Newtonian flow without requiring additional parameters such as a yield stress.

2.7 Microfluidics Framework

The study of fluid dynamics in microchannels is crucial for applications in lab-on-a-chip devices, biomedical diagnostics, and chemical processing systems [70, 79]. From a theoretical standpoint, the flow through a microchannel can be described by solving Eq. 2.31, which relates the pressure difference across the system, the flow rate, and the resistance of the system:

$$\Delta P = R\,Q \tag{2.31}$$

This equation establishes a relationship between the pressure difference ΔP, the flow resistance R, and the flow rate Q [64]. The flow resistance is a function of the system's geometric and physical properties, such as the length and geometry of the channel and connecting tubes, as well as the viscosity of the fluid. By solving this equation, we can predict how the dynamics of the fluid will evolve as experimental parameters are varied, providing insights into the behavior of flow in microchannels [80].

The total resistance of the system is given by the combined resistance of the microchannel and the connecting tubes, as described by Eq. 2.32:

$$R = R_m + R_t \tag{2.32}$$

The resistance of the microchannel can be expressed as:

$$R_m = \frac{12\eta x(t)}{b^3 w\left(1 - 0.63\frac{b}{w}\right)} \tag{2.33}$$

where η is the viscosity of the fluid, $x(t)$ is the length of the fluid column in the microchannel at time t, b is the height of the channel, and w is the width of the channel,

the factor $(1 - 0.63\frac{b}{w})$ represents a correction applied to account for the confinement effects in rectangular microchannels with finite height and width (3D confinement).

Similarly, the resistance of the connecting tubes is given by:

$$R_t = \frac{8\eta}{\pi} \sum_i \frac{L_i}{r_i^4} \tag{2.34}$$

Here L_i and r_i are the length and radius of the i-th tube, respectively. Substituting the resistances into Eq. 2.31 and considering that the flow rate Q is constant throughout the system due to mass conservation, we obtain [81]:

$$\frac{\Delta P}{\eta} = bw\dot{x(t)} \left[\frac{8}{\pi} \left(\sum_i \frac{L_i}{r_i^4} \right) + \frac{12x(t)}{b^3 w \left(1 - 0.63\frac{b}{w}\right)} \right] \tag{2.35}$$

In our case, the pressure difference corresponds to the inlet pressure of the system minus the capillary pressure, which is a function of the radii of curvature, the contact angle of the fluid with the channel walls (θ), and the surface tension (γ). The capillary pressure is given by [70]:

$$P_L = 2\,\gamma\, cos(\theta) \left(\frac{1}{b} + \frac{1}{w} \right) \tag{2.36}$$

Solving the differential equation (Eq.2.35) for a single tube yields the position of the fluid front $x(t)$ as a function of time:

$$\begin{aligned} x(t) = \frac{b^3 w \left(1 - 0.63\,\frac{b}{w}\right)}{12} \Bigg\{ \Bigg[\Bigg(\frac{8}{\pi}\frac{L}{r^4} + \frac{12}{b^3 w \left(1 - 0.63\,\frac{b}{w}\right)} x_0 \Bigg)^2 \\ + \frac{24}{b^3 w^2 \left(1 - 0.63\,\frac{b}{w}\right)} \frac{\Delta P}{\eta} (t - t_0) \Bigg]^{1/2} - \frac{8}{\pi}\frac{L}{r^4} \Bigg\}. \end{aligned} \tag{2.37}$$

This solution provides critical insights into the time-dependent behavior of the fluid within the system. Fig. 2.3 shows theoretical curves generated from Eq. 2.37 for two sets of parameters.

For Parameter 1, the resistance of the connecting tube (Eq. 2.34) is negligible compared to the resistance of the microchannel (Eq. 2.33). Consequently, most energy loss occurs within the microchannel, leading to a decrease in velocity as the fluid progresses. In contrast, for Parameter 2, the tube's resistance dominates, causing the velocity to remain constant within the microchannel. These results illustrate the critical role of geometric and physical parameters in microfluidic systems [79, 80].

Rearranging the equation in terms of the shear rate $\dot{\gamma}$ (Eq.2.23),substituting in the Eq. 2.35 we obtain:

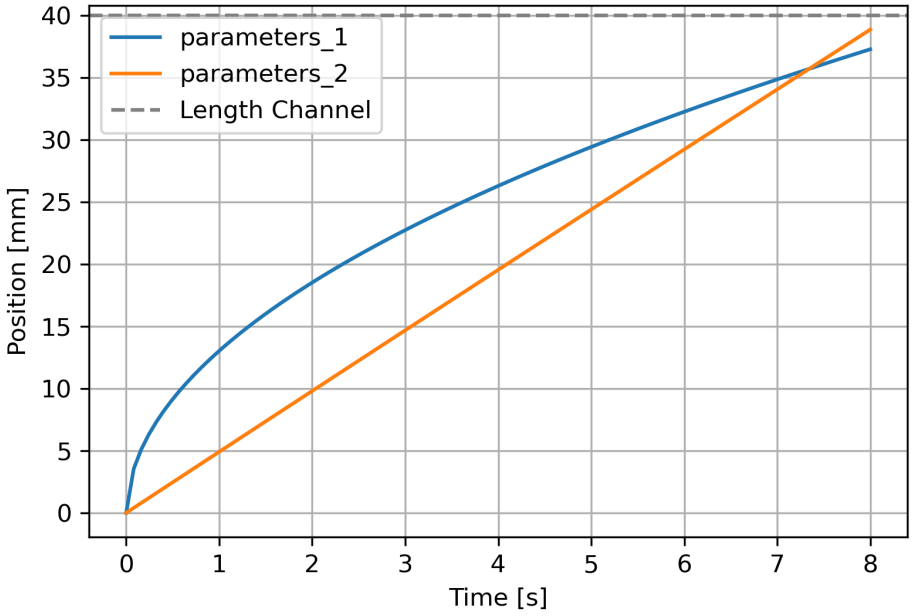

Figure 2.3: Theoretical curves from Eq. (2.37) for two parameter sets. Both use $L = 60\,\text{cm}$, $r = 127\,\mu\text{m}$, and $l_c = 4\,\text{cm}$. Parameter 1 corresponds to a microchannel with $b = 17\,\mu\text{m}$, $w = 100\,\mu\text{m}$, and an injection pressure of 11760 Pa. Parameter 2 corresponds to $b = 150\,\mu\text{m}$, $w = 1\,\text{mm}$, and an injection pressure of 4900 Pa.

$$\frac{\Delta P}{\left[\frac{4}{3\pi}\left(\frac{Lb^2w}{r^4}\right) + \frac{2x(t)}{b\left(1-0.63\frac{b}{w}\right)}\right]} = \eta\,\dot{\gamma} \tag{2.38}$$

From this expression, we can identify the stress τ acting on the fluid as:

$$\tau = \frac{\Delta P}{\left[\frac{4}{3\pi}\left(\frac{Lb^2w}{r^4}\right) + \frac{2x(t)}{b\left(1-0.63\frac{b}{w}\right)}\right]} \tag{2.39}$$

Since viscosity is defined as the ratio of stress to shear rate, the effective viscosity η for Newtonian fluids can be expressed as:

$$\eta = \frac{\Delta P}{\left(\dot{x(t)}\right)\left[\frac{8}{\pi}\left(\frac{Lb^2w}{r^4}\right) + \frac{12x(t)}{b^2\left(1-0.63\frac{b}{w}\right)}\right]} \tag{2.40}$$

Non-Newtonian fluids exhibit complex rheological behavior, where the shear stress is

not proportional to the shear rate. According to the power-law model, the shear stress τ is related to the shear rate $\dot{\gamma}$ as [76]:

$$\tau = K(\dot{\gamma})^n \tag{2.41}$$

where K is the consistency index and n is the flow behavior index. By solving for the velocity gradient:

$$\left(\frac{\tau}{K}\right)^n = \frac{d\mathbf{v_x}(y)}{dy} \tag{2.42}$$

Integrating both sides over the channel height:

$$\mathbf{v_x}(y) = \left(\frac{\Delta P}{KL}\right)^n \int_y^{b/2} y^{1/n} dy \tag{2.43}$$

Solving the integral results in the velocity profile:

$$\mathbf{v_x}(y) = \left(\frac{\Delta P}{KL}\right)^{1/n} \left(\frac{n}{1+n}\right) \left(\left(\frac{b}{2}\right)^{1+\frac{1}{n}} - (y)^{1+\frac{1}{n}}\right) \tag{2.44}$$

Now, assuming that the shear rate is a function of stress, i.e., $\dot{\gamma} = f(\tau)$, we obtain:

$$\frac{dv_x(y)}{d\tau} = \left(\frac{dv_x(y)}{dy}\right)\left(\frac{dy}{d\tau}\right) = \dot{\gamma}\left(\frac{dy}{d\tau}\right) = f(\tau)\left(\frac{dy}{d\tau}\right) \tag{2.45}$$

Thus, integrating, the velocity expression becomes:

$$\mathbf{v_x}(y) = \left(\frac{L}{\Delta P}\right) \int_0^{\tau_{h/2}} f(\tau) d\tau \tag{2.46}$$

The volumetric flow rate Q can be determined by integrating the velocity profile over the cross-sectional area:

$$
\begin{aligned}
Q &= \int_{-b/2}^{b/2} \mathbf{v_x}(y)\, da = \int_{-b/2}^{b/2} \left(\frac{L}{\Delta P}\right) \int_0^{\tau_{h/2}} f(\tau)\, d\tau\, w\, dy \\
&\rightarrow Q = \frac{2wL}{\Delta P} \int_0^{b/2} \int_0^{\tau_{h/2}} f(\tau)\, d\tau\, dy \\
&= \frac{2wL}{\Delta P} \int_0^{\tau_{h/2}} f(\tau)\, d\tau \int_0^{\tau} \frac{L}{\Delta P}\, d\tau \\
&= 2w \left(\frac{L}{\Delta P}\right)^2 \int_0^{\tau_{h/2}} \tau\, f(\tau)\, d\tau
\end{aligned}
\tag{2.47}
$$

If $n = 1$ and $f(\tau) = \dot{\gamma}$, substituting into Eq.2.47 and Eq. 2.44 yields the Newtonian flow rate and velocity profile equations.

Continuing from Eq.2.47, we manipulate the equation further:

$$
\begin{aligned}
Q &= 2w \left(\frac{L}{\Delta P}\right)^2 \int_0^{\tau_{h/2}} \tau\, f(\tau)\, d\tau \\
&\rightarrow \frac{Q}{2w} \left(\frac{\Delta P}{L}\right)^2 = \int_0^{\tau_{h/2}} \tau\, f(\tau)\, d\tau
\end{aligned}
\tag{2.48}
$$

From differentiation and mathematical manipulation, we obtain:

$$
\begin{aligned}
2\tau_w \left(\frac{4Q}{2wb^2}\right) + \tau_w^2 \frac{d}{d\tau_w} \left(\frac{4Q}{2wb^2}\right) &= \tau_w f(\tau_w) \\
\dot{\gamma_w} = \frac{1}{\tau_w} \left[\tau_w \left(\frac{4Q}{2wb^2}\right) + \tau_w^2 \frac{d}{d\tau_w} \left(\frac{4Q}{2wb^2}\right)\right] \\
\dot{\gamma_w} = \frac{4Q}{wb^2} \left[1 + \frac{wb^2}{4Q} \tau_w \frac{d}{d\tau_w} \left(\frac{2Q}{wb^2}\right)\right]
\end{aligned}
\tag{2.49}
$$

Using logarithmic differentiation properties:

$$
\frac{d\ln(\tau_w)}{d\tau_w} = \frac{1}{\tau_w}, \quad \frac{d\ln(\dot{\gamma_a})}{d\dot{\gamma_a}} = \frac{1}{\dot{\gamma_a}}
\tag{2.50}
$$

Substituting these expressions results in:

$$
\dot{\gamma_w} = \frac{4Q}{wb^2} \left[1 + \frac{1}{2} \frac{d\ln(\dot{\gamma_a})}{d\ln(\tau_w)}\right]
\tag{2.51}
$$

Since $\frac{d\ln(\dot{\gamma}_a)}{d\ln(\tau_w)} = \frac{1}{n}$, simplifying yields the well-known Rabinowitsch-Mooney correction for non-Newtonian fluids [82]:

$$\dot{\gamma}_w = \frac{1}{3}\dot{\gamma}_a \left[\frac{2n+1}{3n}\right] \tag{2.52}$$

2.8 The Washburn Effect

The Washburn effect describes the spontaneous infiltration of a liquid into a capillary or porous medium driven by capillary forces. This phenomenon is quantitatively described by the Washburn equation, which relates the penetration length l of the liquid to time t [83, 84]:

$$l = \sqrt{\frac{\gamma r \cos\theta}{2\eta} t} \tag{2.53}$$

Here γ denotes the liquid's surface tension, r represents the radius of the capillary, θ is the contact angle between the liquid and the capillary wall, and η signifies the dynamic viscosity of the liquid.

This equation indicates that the penetration depth is proportional to the square root of time, emphasizing the influence of surface tension, viscosity, and capillary dimensions on the infiltration process.

Originally formulated by Edward W. Washburn in 1921, the equation has been instrumental in understanding capillary action in various systems [83]. In microfluidics devices, controlling fluid movement through microchannels relies on principles described by the Washburn effect. Designing channels with specific dimensions and surface properties enables precise manipulation of small fluid volumes for diagnostics and chemical analysis [85, 86].

Recent work by Berthier et al. [86] extends the classical Washburn equation to composite microchannels with arbitrary cross-sections. Their generalization accounts for variations in channel geometry, allowing for a more precise prediction of capillary-driven flows in microfluidic systems. By incorporating geometric variations, Berthier et al. demonstrate that the effective capillary pressure and viscous resistance depend on the specific cross-sectional shape of the channel. Their model provides a more comprehensive approach to predicting liquid infiltration, improving the design of microfluidic devices used in biomedical and analytical applications. This generalization enhances our ability to design optimized microchannels for applications such as point-of-care diagnostics, inkjet printing, and controlled drug delivery.

While the Washburn equation provides a foundational understanding, it assumes ideal conditions, such as constant viscosity and negligible gravitational effects. Real-world applications may require modifications to account for factors like evaporation, fluid inertia, and complex pore structures. The extended model proposed by Berthier

et al. [86] helps address some of these limitations, making it a valuable tool in modern microfluidic research. Nonetheless, the Washburn effect remains a cornerstone in the study of capillary phenomena, offering critical insights into fluid behavior in confined geometries.

2.9 Young-Laplace Equation and Law of Laplace

The Young-Laplace (Y-L) equation, presented in Eq. 2.55, relates the pressure difference ΔP across a curved fluid interface to the surface tension γ and the radius of curvature R [87, 88]. In the context of this research, the Y-L equation is utilized to determine the surface tension of the simulated droplet.

$$\Delta P = \gamma \left(\frac{1}{R_1} + \frac{1}{R_2} \right) \tag{2.54}$$

By solving this equation for γ, the surface tension across the droplet's curved interface can be calculated. This relationship is often referred to as the Law of Laplace. The surface tension value serves as a calibration parameter for simulations when the other variables are known, as it is a measurable physical property.

The Law of Laplace, shown explicitly in Eq. 2.55, states that the pressure inside a droplet or bubble is inversely proportional to its radius of curvature. To implement this law, it is essential to consider the droplet as a perfect sphere in air, neglecting the effects of gravity.

$$\Delta P = \frac{2\gamma}{R} \quad \rightarrow \quad \gamma = \frac{R\Delta P}{2} \tag{2.55}$$

2.10 Bond Number

Surface tension plays a critical role in fluid dynamics, particularly at small scales where the surface-area-to-volume ratio is high. At the microscale, surface tension dominates, acting to minimize the surface area of the fluid. The Bond number (Bo), a dimensionless parameter, provides a quantitative measure of the relative contributions of surface tension (γ) and body forces (typically ρ and g). It enables a comprehensive understanding of the interplay between these forces in microscale fluid dynamics [89].

In systems with small Bond numbers ($Bo < 1$), the influence of gravity is negligible, and the interface curvature described by Laplace's law remains constant. A Bond number ($Bo < 1$) indicates that surface tension dominates the droplet's behavior compared to gravitational forces [38]. Conversely, as the droplet's volume increases, gravitational forces become more significant, leading to an increase in the Bond number. For $Bo > 1$, inertial and gravitational forces dominate, often resulting in rupture or instability [38].

The Bond number is defined as:

$$Bo = \frac{\rho g L^2}{\gamma} \tag{2.56}$$

where L represents the characteristic length of the fluid, typically the droplet's diameter.

In phenomena such as splashes and sloshes, microdroplets often form due to shear stresses during fluid collisions. The fluid dynamics of these microdroplets are significantly influenced by surface tension effects, which are frequently overlooked in SPH simulations [90]. This study employs Laplace's law and the Bond number to analyze the fluid system's behavior under varying volumes, highlighting the critical role of surface tension in microscale dynamics.

2.11 Navier-Stokes equation on SPH formalism

The continuity and Navier-Stokes equations are traditionally used to describe the motion of fluids. These equations are derived from the principles of mass conservation (Eq. 2.57) and momentum conservation (Eq. 2.58) within a Lagrangian framework.

$$\frac{d\rho}{dt} = -\rho \nabla \cdot \mathbf{v} \tag{2.57}$$

$$\frac{D\mathbf{v}}{Dt} = -\frac{1}{\rho}\nabla P + \boldsymbol{g} + \Gamma + \boldsymbol{F}_{ipf} \tag{2.58}$$

where ρ is the density, ∇ is the gradient operator, $\mathbf{v}$ is the fluid velocity, P is the pressure, $\mathbf{g}$ is the gravity, Γ is the viscous dissipative term, and $\mathbf{F}_{ipf}$ is in this particular case the internal particle force.

SPH is a meshless method that has been employed to simulate a wide range of applications for solving hydrodynamic problems. SPH employs integral equations based on an interpolation function to convert partial differential equations into particle-based simulations. The book of Liu or Violeau can be consulted for a full explanation of the details of the SPH method [4, 91]. The integral interpolation approximation used in the SPH method is provided in Equation 2.59.

$$F(\mathbf{x}) = \int_{\Omega} F(\mathbf{x}')W(\mathbf{x} - \mathbf{x}', h)d\mathbf{x}', \tag{2.59}$$

where $F(\mathbf{x})$ is a continuous function, $\mathbf{x}$ is a position variable, W is the smoothing kernel, and h is the smoothing length that defines the influence of the kernel in a domain Ω.

The continuous SPH integral interpolation representation is discretized by the summation over all particles within h. The particle approximation for a function at particle a is written in Eq. 2.60.

$$F(\mathbf{x}_a) = \sum_{b=1}^{N} \frac{m_b}{\rho_b} f(\mathbf{x}_b) \cdot W(|\ \mathbf{x}_a - \mathbf{x}_b|, h) \tag{2.60}$$

Where $\mathbf{x}_a$ is the position of particle a. The subscripts b denote the neighbour-interacting particles, m_b, ρ_b, $\mathbf{x}_b$ are mass, density, and position of particles b, respectively.

The smoothing kernels are usually designed to possess the following properties and requirements: compact support, normalization, positivity within an interaction zone, and it should exhibit decreasing values as the distance between particles increases. In this study, the fifth-order Wendland function is employed, which is known for its reduced pairing instability[92] represented by Equation 2.61.

$$W(r, h) = \alpha_D \left(1 - \frac{q}{2}\right)^4 (2q + 1) \quad for \quad 0 \leq q \leq 2 \tag{2.61}$$

where α_D is $21/16\pi h^3$ in 3-dimensions, q is r/h, and r is the distance between neighboring particles ($r = |\mathbf{x}_a - \mathbf{x}_b|$).

The Eq.2.57 and 2.58 are discretized using the integral interpolation approximation from Eq. 2.60, resulting in the equations Eq. 2.62 and Eq. 2.63, respectively.

$$\frac{d\rho_a}{dt} = -\rho_a \sum_b \frac{m_b}{\rho_b} (\mathbf{v}_a - \mathbf{v}_b) \cdot \nabla_a W_{ab} \tag{2.62}$$

$$\frac{d\mathbf{v}_a}{dt} = -\sum_b \left(\frac{p_a + p_b}{\rho_a \rho_b}\right) \nabla_a W_{ab} + \mathbf{g} + \Gamma_{ab} + \mathbf{F}_{int} \tag{2.63}$$

The viscous dissipative term Γ_{ab} is the stress tensor and is described in Eq. 2.64 using the laminar viscosity model, proposed by Lo et al [93].

$$\Gamma_{ab} = \sum_b m_b \left(\frac{4\nu r_{ab} \cdot \nabla_a W_{ab}}{(\rho_a + \rho_b)(r_{ab}^2 + \eta^2)}\right) (\mathbf{v}_a - \mathbf{v}_b) \tag{2.64}$$

where ν is the kinematic viscosity and $\eta = 0.01h^2$. This term helps avoid division by zero when $a = b$.

A constitutive equation of state (EOS) is commonly employed for each phase to close the system of Eq. 2.57 and 2.58. In this work, pressure is determined by density through the Tait equation, [68], expressed in Eq. 2.65.

$$p = \frac{c^2 \rho_0}{7} \left[\left(\frac{\rho}{\rho_0}\right)^7 - 1\right] \tag{2.65}$$

where p is the fluid pressure, ρ_0 is a reference density and c is the speed of sound inside the reference fluid. According to the Courant-Friedrichs-Lewy (CFL) condition,

the use of the physical speed of sound in water will require a prohibitively small-time step in order to obtain a solution of the equation of Navier-Stokes in SPH form. Therefore, it is necessary to use a quasi-incompressible EOS for fluids in SPH, where an artificial speed of sound is much lower than the real one. On the other hand, an inappropriately low speed of sound might make the liquid more compressible than it should be. As a result, the chosen speed of sound must be large enough to ensure that the behavior of the corresponding quasi-incompressible fluid is sufficiently close to the real one and yet reasonably small to allow the use of practically large time steps in the calculation.

The SPH equations were integrated using the "Verlet velocity algorithm" [94] as seen in Eq.2.66, Eq.2.67, and Eq.2.68. In this case, the time step was set variable to encompass the CFL condition, using the next relations [95].

$$\mathbf{x}_i(t+\Delta t) = \mathbf{x}_i(t) + \Delta t \mathbf{v}_i(t) + \frac{\Delta t^2}{2m_i}\mathbf{f}_i(t) \tag{2.66}$$

$$\mathbf{v}_i(t+\Delta t) = \mathbf{v}_i(t) + \frac{\Delta t}{2m_i}\left[\mathbf{f}_i(t) + \mathbf{f}_i(t+\Delta t)\right] \tag{2.67}$$

$$\mathbf{f}_i(t+\Delta t) = \mathbf{F}_i^P(t+\Delta t) + \mathbf{F}_i^\Gamma(t+\Delta t) + \mathbf{F}_i^{int}(t+\Delta t) + \mathbf{g} \tag{2.68}$$

The variable time step is calculated applying the following constraints [6] in Eq.2.69:

$$\begin{aligned} \Delta t &\leq 0.25 \min_i \left(\frac{h}{3\left|\mathbf{v}_i\right|}\right) \\ \Delta t &\leq 0.25 \min_i \left(\sqrt{\frac{m_i h}{3\left|\mathbf{f}_i\right|}}\right) \\ \Delta t &\leq 0.25 \min_i \left(\frac{\rho_i h^2}{9\eta}\right) \end{aligned} \tag{2.69}$$

Generally, SPH uses the Navier-Stokes equation for liquid dynamics and depends on small differences in density and pressure and the characteristic viscosity of the simulated fluid. SPH works well for simulations where small-scale dynamics do not play a prominent role, encompassing scenarios ranging from centimeters to meters or even kilometers in most cases. Nonetheless, by reducing the scale, the inherent cohesive forces of fluids can lead to the insignificance of terms related to body forces (as defined by the Bond number), causing the dynamics to be governed by the surface tension. So, it is important to take into consideration the surface tension (small forces) in big volumes of liquid or the simulation becomes less reliable, like in cases of splashing, where the collision of water masses and shear forces give rise to microdroplet formation. In such instances, it becomes imperative to introduce a force term to the Navier-Stokes equation that governs the dynamics of micro-volumes.

3 SPH Simulation Code

This chapter details the code developed for implementing the Smoothed Particle Hydrodynamics (SPH) method. Here we discuss the main stages of the simulation, from the initialization and distribution of particles to the temporal integration and optimizations performed. The code is designed for efficient execution on GPU devices using the `Taichi` framework [96], enabling high-performance simulations in complex domains.

The simulation starts with a homogeneous distribution of particles, where the total number of particles is denoted as `num_particle`. A maximum number of simulation steps, `total_step`, is set, defining when the simulation should stop. In each iteration, if the current step is less than `total_step` (the total number of steps), the simulation continues. First, we identified the neighbors for each particle within the simulation. Then, in the first loop, each particle is iterated to compute its density and pressure based on its neighbors. Once the density and pressure fields are determined, a second loop is executed, where all particles are iterated again, but this time to compute the pressure gradient and internal forces acting on them. The separation into two loops is crucial because force calculations require prior knowledge of the density and pressure distribution throughout the entire domain, ensuring stability and accuracy in the simulation. Finally, with the total forces known, the acceleration of each particle is determined, allowing for the update of its velocity and position. This process is iteratively repeated until the total number of steps (`total_step`) is reached, ensuring the consistent evolution of the simulation using the SPH method (See Fig. 3.1). The code has been designed with modularity and efficiency in mind, ensuring that each component can be independently tested, optimized, and reused. The implementation employs the `Taichi` framework [96] for high-performance GPU-accelerated computations, enabling the simulation of complex scenarios with a large number of particles in a computationally efficient manner. This chapter elaborates on how these concepts are translated into functional code.

In the following sections, we provide a detailed explanation of the various components of the code and describe how each part is implemented. The explanation includes the fundamental building blocks of the Smoothed Particle Hydrodynamics (SPH) simulation, from initialization to temporal integration and optimization techniques. Each section focuses on a specific aspect of the simulation to provide a clear understanding of the methodology and its implementation.

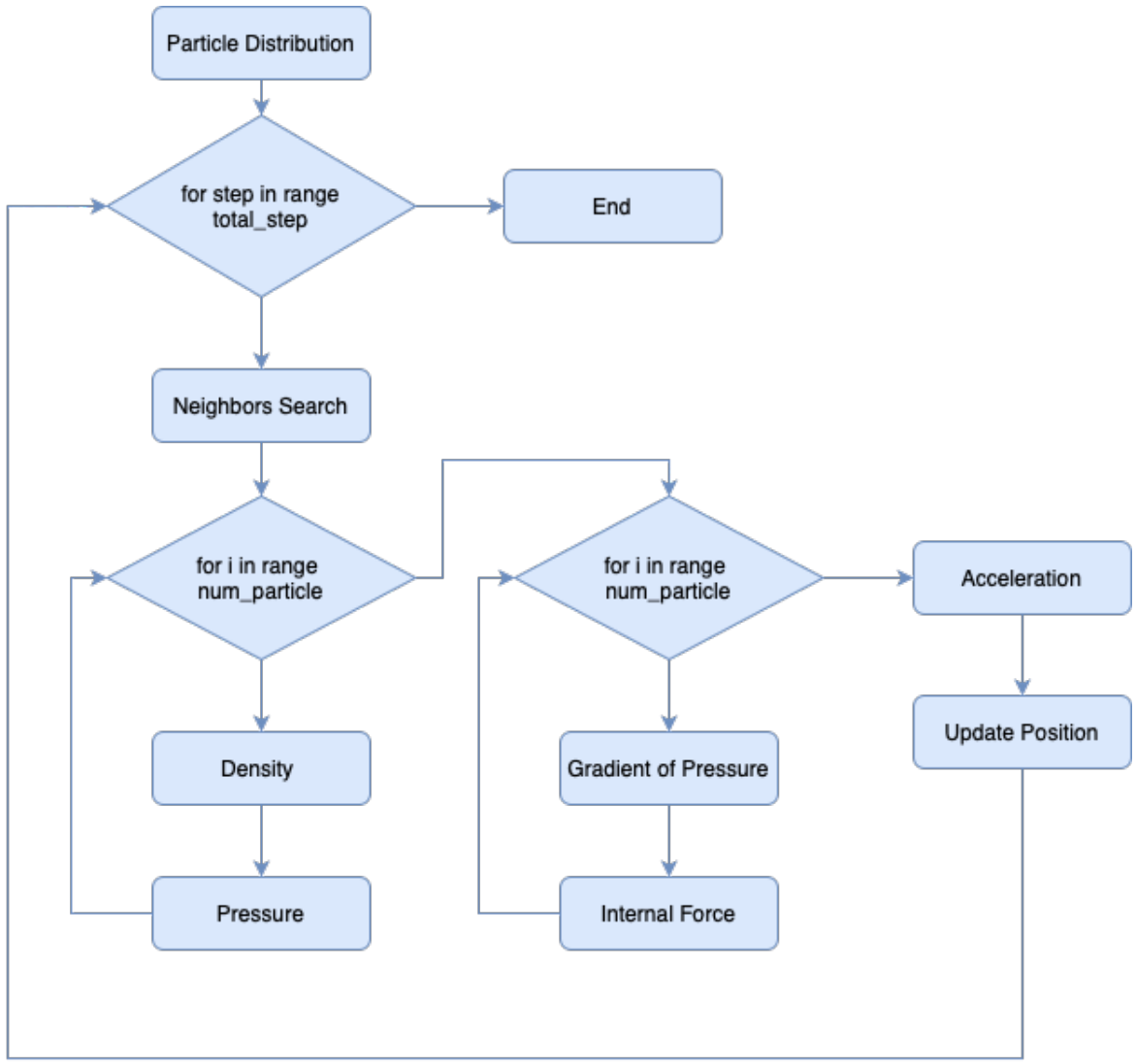

Figure 3.1: The flowchart of the developed code starts with a distribution of particles with predefined positions. The simulation enters a time-stepping loop. At each time step, the neighbors of each particle are calculated. There are two sub-loops: the first computes the density and pressure fields for all fluid particles. Once these fields are obtained, the second sub-loop calculates the pressure gradient (based on the density and pressure fields) and the forces acting on the particles. Using this information, the acceleration, velocity, and new position of each particle are updated. These updated positions are then used for the next iteration of the loop, and the process continues until all time steps are completed.

3.1 Particle Distribution

The first step in any SPH simulation is to establish the initial distribution of particles. This stage defines the system's initial state, including the position and physical properties of each particle (density, mass, velocity, etc.). In our case, particles are distributed based on data loaded from `CSV` files; these files are obtained from a script in which the fluid particles and the solid particles (flat, micro-channels) are generated depending on the simulation application, which will be loaded to the main code where the simulation is performed. The initial particle spacing, ds, ensures a uniform density distribution within the domain and is defined as:

$$ds = \frac{L}{N_p^{1/3}} \tag{3.1}$$

where L is the characteristic length of the domain (for example, the edge length of a cube), and N_p is the total number of particles. Therefore, if a cubic domain of edge length L is to be simulated using N_p particles, this expression allows the computation of the appropriate particle spacing to achieve a uniform distribution. This approach enables the modeling of complex geometries, such as microfluidic channels, ensuring an accurate representation of the physical problem. Below is the pseudocode for initializing the particle distribution:

Algorithm 1 Initial Particle Distribution

```
Load data from CSV file
Normalize initial positions to the physical domain
Compute ds = L / N_p^(1/3)
for each particle i do
    Assign initial position x_i
    Initialize velocity v_i = 0
    Assign physical properties (mass, density)
end for
```

3.2 Neighbors Search

Neighbor searching is a critical step in the Smoothed Particle Hydrodynamics (SPH) method because it determines which particles interact within a support radius ($h_0 = 1.8\,ds$). This radius corresponds to the maximum distance at which neighboring particles have influence on the particle of interest. Since SPH relies on localized interactions, identifying neighbors efficiently is essential to ensure the computational feasibility of simulations involving large numbers of particles.

In SPH simulations, the less efficient neighbor search involves calculating the distance between every pair of particles, resulting in a computational complexity of $O(N^2)$,

where N is the total number of particles. This becomes prohibitive as N increases. Consequently, optimizing this step can significantly reduce the simulation runtime and enable the study of larger and more complex systems.

Initially, the simulation utilized Python's KDTree library for neighbor searching. While KDTree is an effective tool for spatial queries, its implementation on a single CPU core proved insufficient for simulations with a high particle count, requiring approximately 120 seconds per simulation step with $125K$ particles of fluid .

To address this limitation, the implementation transitioned to MATLAB [97], leveraging its built-in parallel computing capabilities. By utilizing multiple CPU cores, the runtime per step was reduced to 4.32 seconds, representing a substantial improvement. However, further optimization was necessary for real-time or large-scale simulations.

Finally, the neighbor search algorithm was implemented using the Taichi library [96] in Python, a high-performance framework designed for GPU parallelization. By taking advantage of the massively parallel architecture of GPUs, the runtime per simulation step was reduced to just 0.06 seconds, enabling efficient execution of computationally demanding SPH simulations.

The current implementation combines the Taichi library [96] with a spatial hashing technique [98]. The simulation domain is divided into uniform cells of size `cell_size`, which are defined as $h_1 = 2.5ds$, with particles assigned to these cells. For each particle, neighbors are identified by inspecting adjacent cells. This approach balances computational efficiency and simplicity while benefiting from GPU acceleration.

Algorithm 2 Neighbor Search with Spatial Hashing

```
Divide the domain into cells of size cell_size
for each particle i do
    Compute i's cell based on its position
    Add i to the corresponding cell
end for
for each particle i do
    Initialize neighbor list
    for each adjacent cell do
        for each particle j in the cell do
            if r_ij < h_1 then
                Add j to i's neighbor list
            end if
        end for
    end for
end for
```

The Fig.3.2 illustrates the performance improvements achieved through successive optimizations of the neighbor search implementation. To compare performance, we plot the execution time required to complete 1000 simulation cycles or steps was plotted.

The results show a significant reduction from 33 hours per 1000 steps to just 0.017 hours ($62s$) per 1000 steps. This optimization is crucial for long simulations, such as those involving $100k$ steps, as it considerably reduces the overall simulation time.

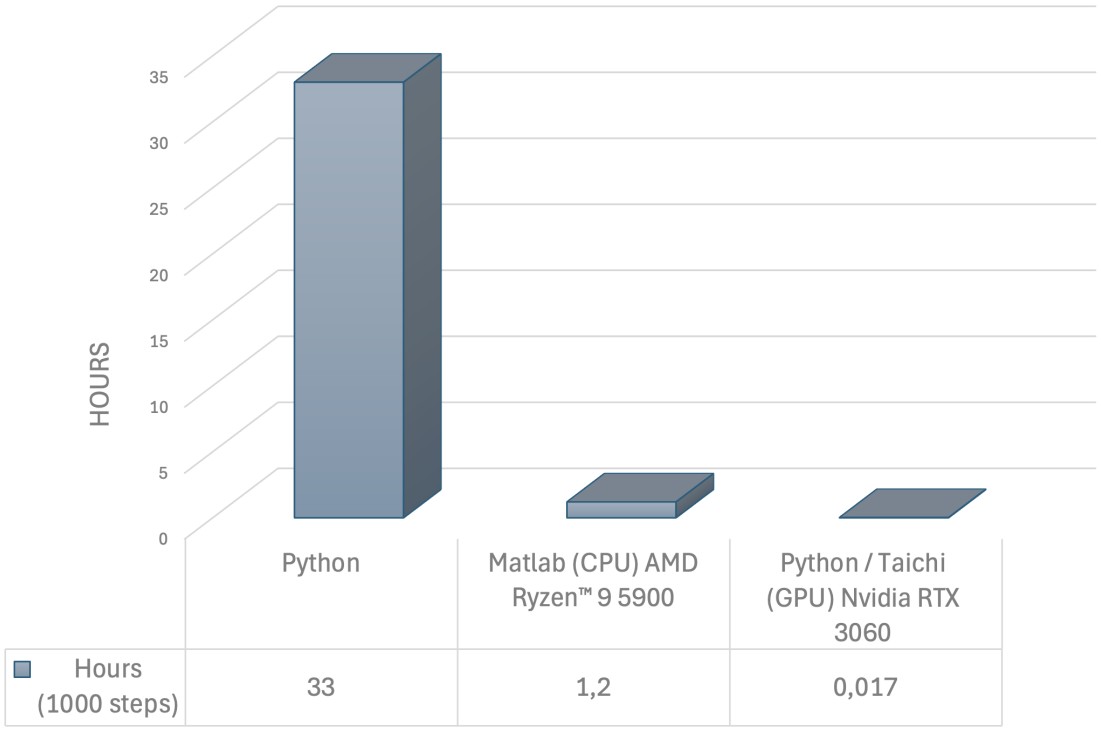

Figure 3.2: Performance comparison of neighbor search implementations using 125K particles. Python KDTree (single-core) requires 33 hours per 1000 step, MATLAB (multi-core CPU) reduces this to 1.2 hours per 1000 steps, and Taichi (multi-core GPU) achieves 0.017 hours ($62\,s$) per 1000 step.

3.3 Density Calculation

Each particle represents a discretized volume of fluid and is assigned an initial mass, which is determined based on the total fluid volume to be simulated and its density. This mass is used to compute the density ρ_i of each particle using the kernel function $W(r, h_0)$, which evaluates the influence of neighboring particles j within a support radius h_0. The equation used is:

$$\rho_i = \sum_j m_j W(r_{ij}, h_0) \tag{3.2}$$

where the subscript i refers to the particle under study, while the subscript j refers to its neighboring particles, $r_{ij} = \|\mathbf{x}_i - \mathbf{x}_j\|$ is the distance between particles i and j,

m_j is the mass of particle j, $W(r, h_0)$ is the Wendland kernel function, and h_0 is the smoothing length that defines the interaction radius of the kernel function [99].

Algorithm 3 Density Calculation

```
for each particle i do
    Initialize ρ_i = 0
    for each neighbor j of i do
        Compute distance r_ij
        if r_ij < h_0 then
            ρ_i += m_j W(r_ij, h_0)
        end if
    end for
end for
```

At the end of this calculation, we obtain the density field of the fluid particles. This information is essential for determining the pressure at each particle and computing its gradient, which allows for the evaluation of the internal forces within the system.

3.4 Pressure Calculation

The pressure calculation is a fundamental step in SPH because it determines the force exerted by the fluid on each particle. The pressure P_i of each particle is computed using the Tait equation of state [68], which establishes a relationship between local density and pressure:

$$P_i = B\left[\left(\frac{\rho_i}{\rho_0}\right)^{\gamma} - 1\right] \tag{3.3}$$

where B is a parameter related to the speed of sound in the fluid,ρ_0 is the reference density, and γ is a dimensionless exponent.

In the literature [5, 91, 100] , the exponent γ is typically set to 7 to ensure a quasi-incompressible behavior of the fluid. This choice is crucial because if the simulated density ρ_i deviates from the reference density ρ_0, the pressure increases significantly. As a result, the pressure becomes highly sensitive to density fluctuations, effectively preventing large compressibility effects and ensuring numerical stability in the simulation. Once the pressure is computed for all particles, a pressure field is obtained, representing the spatial distribution of pressure throughout the fluid. This field is essential for computing pressure gradients in the next step, which will be used to determine the internal forces acting on each particle, driving the motion of the fluid.

Algorithm 4 Pressure Calculation

1: **for** each particle i **do**
2: $\quad P_i = B\left[\left(\frac{\rho_i}{\rho_0}\right)^{\gamma} - 1\right]$
3: **end for**

3.5 Gradient of Pressure

The pressure gradient is computed to determine the internal forces acting on particles due to pressure differences. This force is responsible for driving fluid motion by ensuring that particles move from regions of high pressure to regions of low pressure. The equation governing this force is:

$$\mathbf{F}_i^{\text{pressure}} = -\frac{1}{\rho}\nabla P = -\sum_j m_j \left(\frac{P_i}{\rho_i^2} + \frac{P_j}{\rho_j^2}\right) \nabla W(r_{ij}, h_0) \tag{3.4}$$

here, the subscript i refers to the particle under study, while the subscript j refers to its neighboring particles. $\mathbf{F}_i^{\text{pressure}}$ it is the acceleration that the fluid experiences due to the change of pressure in space. m_j is the mass of the neighboring particle j, P_i and P_j represent the pressures of particles i and j, respectively, ρ_i and ρ_j denote the densities of particles i and j, respectively,$\nabla W(r_{ij}, h_0)$ is the gradient of the kernel function, which determines the spatial influence of neighboring particles, and h_0 is the smoothing length that defines the interaction radius of the kernel function.

The calculation of the pressure gradient determines the internal forces responsible for balancing the fluid dynamics. By computing this force, we obtain a pressure force field, which describes the net effect of pressure interactions on each particle. This force field is then used to compute the total acceleration of each particle.

Algorithm 5 Pressure Gradient

1: **for** each particle i **do**
2: $\quad$ Initialize $\mathbf{F}_i^{\text{pressure}} = \mathbf{0}$
3: $\quad$ **for** each neighbor j of i **do**
4: $\quad\quad$ Compute $\nabla W(r_{ij}, h_0)$
5: $\quad\quad$ Update $\mathbf{F}_i^{\text{pressure}}$ with j's contributions
6: $\quad$ **end for**
7: **end for**

3.6 Internal Force Calculation

The internal force acting on each particle is calculated as the derivative of a general pair potential $\Phi(r)$, which governs the interaction between particles within a specified

cutoff radius r_c. The force $\mathbf{F}_i^{\text{internal}}$ acting on particle i due to all its neighbors is given by:

$$\mathbf{F}_i^{\text{internal}} = -\sum_j \nabla\Phi(r_{ij}), \tag{3.5}$$

where $r_{ij} = \|\mathbf{x}_i - \mathbf{x}_j\|$ is the distance between particles i and j,and $\nabla\Phi(r_{ij})$ is the gradient of the pair potential. This formulation ensures that particle interactions vary continuously and smoothly with inter-particle distance, which improves numerical stability, while being spatially restricted to neighboring particles within the cutoff radius r_c, reducing computational cost and reflecting the localized nature of short-range physical forces. The algorithm for implementing this force calculation is as follows:

Algorithm 6 Internal Force Calculation

```
for each particle i do
    Initialize F_i^internal = 0
    for each neighbor j of i do
        Compute r_ij = ||x_i − x_j||
        if r_ij ≤ r_c then
            Compute ∇Φ(r_ij)
            Update F_i^internal += −∇Φ(r_ij)
        end if
    end for
end for
```

3.7 Time Integration with Verlet

The Verlet method is used to efficiently integrate the position and velocity of each particle over time [94]. This method is widely employed in molecular dynamics and particle-based simulations due to its simplicity, stability, and time-reversibility properties. The position update follows the equation:

$$\mathbf{x}_i(t + \Delta t) = \mathbf{x}_i(t) + \mathbf{v}_i(t)\Delta t + \frac{1}{2}\mathbf{a}_i(t)\Delta t^2 \tag{3.6}$$

The Verlet integration method is advantageous because it is symplectic and conserves energy better than explicit Euler methods, reducing numerical errors in long-term simulations. Additionally, it does not require storing previous velocity values, making it computationally efficient.

By applying this integration scheme, we ensure that each particle follows a smooth trajectory while maintaining numerical stability, which is essential for accurately simulating the dynamics of the fluid. The motion of the entire fluid is obtained by calculating the contribution of all physical interactions acting on each particle and integrating

them over time. Specifically, the total force on each particle is computed by summing the previously calculated interactions, including the pressure gradient and internal forces. The resulting total force $\mathbf{F}_i$ is then divided by the particle's mass to obtain the acceleration, following the expression $a_i = \mathbf{F}_i / m_i$.

This acceleration is the key link between the computed forces and the resulting particle trajectories. The particle's velocity and position are updated at each timestep. In this way, all individual interactions—pressure, viscosity, and any additional forces—are consistently combined within the integration loop to produce the global motion of the fluid.

Therefore, the simulation evolves as each particle continuously updates its position and velocity based on the cumulative effects of all forces from its neighbors. This process, when applied to every particle in the system, effectively models the complete fluid dynamics, providing a physically coherent and numerically stable representation of the fluid's behavior.

Algorithm 7 Time Integration (Verlet)

1: **for** each particle i **do**
2: Update position $\mathbf{x}_i(t + \Delta t)$
3: Update velocity $\mathbf{v}_i(t + \Delta t)$
4: **end for**

3.8 Conclusion

This chapter has presented a detailed overview of the developed Smoothed Particle Hydrodynamics (SPH) simulation code, highlighting its key computational stages and optimizations. Starting with particle initialization, we established a structured approach to define the initial state of the system, ensuring uniform distribution and accurate representation of physical properties.

A crucial aspect of the simulation was the efficient neighbor search algorithm, which transitioned from an initial CPU-based approach to a highly optimized GPU-accelerated implementation using the `Taichi` framework. This optimization significantly improved computational efficiency, reducing execution time from several hours to a few minutes, enabling the simulation of large-scale fluid systems.

Following neighbor detection, the density and pressure calculations were implemented using the Wendland kernel function and the Tait equation of state, ensuring stability and consistency in fluid behavior. The pressure gradient and internal forces were then computed, forming the basis for determining the dynamic evolution of the system. By leveraging optimized kernel functions, we ensured a physically accurate and computationally efficient representation of fluid interactions.

Finally, the time integration scheme was implemented using the Verlet method, which provides a stable and energy-conserving approach to updating particle positions and

velocities. This method enhances numerical accuracy while maintaining computational efficiency, ensuring the reliability of long-term simulations.

4 Modeling of Surface Tension

Modeling surface tension is a critical challenge in SPH , particularly when simulating free-surface flows, droplet formation, and multiphase interactions at micro and macro scales. In conventional SPH formulations, surface tension effects are not inherently represented, often requiring additional force models to capture the cohesive interactions that give rise to phenomena such as droplet stability, interface curvature, and capillarity. Accurate modeling of surface tension is essential for reproducing real-world behaviors in applications ranging from microfluidic device design to splash dynamics and multiphase flow simulations. This chapter addresses this challenge by incorporating an internal pair potential force into the SPH framework, enabling the representation of gas-liquid interactions and cohesive forces solely within the liquid phase. This approach enhances computational efficiency while maintaining physical fidelity, providing a robust tool for simulating complex interfacial phenomena without explicitly modeling the surrounding gas phase

4.1 Pair Potential force

In this thesis, a pair potential force is proposed to facilitate internal interactions among small liquid volumes. The pair potential force typically captures both repulsive and attractive forces between particles and is commonly used to describe molecular interactions. It consists of two terms: a repulsive term that prevents particles from occupying the same space, and an attractive term that accounts in the case of fluids as a cohesive force. The specific form of the pair potential force equation depends on the chosen potential function and its parameters. In the case of large potentials, some of them are not suitable for molecular interaction simulations because their range of attraction is too large, and their truncated form is too sensitive. Wang et al.'s work [23] proposes a solution for the potentials in Eq. 4.1, which is computationally efficient and commonly used in short-range interaction-based methods as SPH.

$$\Phi(r) = \begin{cases} \varepsilon\alpha \left(\left[\frac{\sigma}{r}\right]^2 - 1 \right) \left(\left[\frac{r_c}{r}\right]^2 - 1 \right)^2 & \text{for } r \leq r_c, \\ 0 & \text{for } r > r_c. \end{cases} \tag{4.1}$$

Here ε is the depth of the attractive well, and σ is the interparticle distance where the potential changes from attractive to repulsive. The cutoff radius of the potential is r_c, where the attractive part of the potential vanishes quadratically, avoiding discontinuity

in the attractive force. The coefficient α, described in Eq. 4.2, ensures that the value of $-\varepsilon$ remains constant.

$$\alpha = 2\left(\frac{r_c}{\sigma}\right)^2 \left(\frac{3}{2\left(\left(\frac{r_c}{\sigma}\right)^2 - 1\right)}\right)^3 \tag{4.2}$$

We used two interacción distances: the smoothing distance $h = 1.8\sigma$ for SPH and the cutoff radius $r_c = 2.5\sigma$ for the pair potential.

These equations contribute to the overall force calculation acting on each particle and can be used in the internal interaction of a liquid, expanding and contracting the system, as if the liquid feels the interaction of external air pressure. Therefore, it is possible to calibrate the value of the surface tension in a droplet by varying the epsilon constant in the potential, allowing the simulation of the effect of atmospheric pressure (air) on the drop using only the liquid phase. The validation of these equations through comparisons with empirical values ensures the reliability and accuracy of the simulated surface tension.

4.2 Numerical Model: Pair Potential into SPH

In the simplest (one-phase) SPH model, free surface phenomena occur as a result of small variations in pressure and density at the interface of the fluid particles. However, in these models the changes resulting in the nature of the fluid, such as free surface phenomena or droplet formation, do not account for the interaction between the two fluids (air and water for example) or provide a physical justification for it. Consequently, phenomena like the contact angle in droplets cannot be accurately represented, nor can the formation of small drops caused by splashing.

From a Lagrangian perspective, the curved surface of a droplet is a consequence of cohesive forces acting between the liquid particles and external gas particles. The internal forces within the droplet and those applied externally by the gas can reach a very delicate equilibrium, where cohesive forces play a crucial role in the formation of droplets at small scales.

One potential solution for representing these phenomena is the use of molecular dynamics methods. However, computational limitations make it impossible to accurately represent even smaller drops.

SPH has advantages for simulations of this type of problems, as it allows, from the Lagrangian perspective, to represent these cohesive forces, including phenomena that operate at small (micro) and large (macro) scales.

To accurately simulate the effects of surface tension in SPH, we propose using a pair potential suggested by Wang et al. [23]. This method involves adding an extra force to the N-S equation, acting between particles, to simulate the cohesive effects of internal phenomena. However, the magnitude of this force needs to be calibrated. In this

work, we employ the values of surface tension and the Y-L equation for this purpose. These forces can also be tested in different scale scenarios for validation, along with the droplet spherization test.

4.2.1 Pair-potential force formulation

The Wang [23] pair potential has been previously employed in simulating cohesive interactions between fluid particles and has shown promising results.

To determine the value of ε in the pair potential, we numerically evaluate it through a comprehensive analysis that allows the calibration of the force corresponding to cohesive interaction in a droplet. For this, we assume that regardless of the number of particles, i.e., the discretization scale, as observed in figure 4.1, the force term associated with the simulation volume must remain constant. In other words, the force term per unit mass of the particles in a given volume should be invariant to the discretization scale and the physics of the system. In this case, the system's physics, represented by the droplet spherization phenomenon, should remain invariant amidst these changes, thereby conserving the droplet volume in all instances.

To test this assumption, numerical experiments were designed for different discretization scales (8K, 27K, 64K, and 125K particles). A value of epsilon was determined for each scale, describing plausible physical behavior, using droplet spherization as a benchmark, as mentioned earlier. Fig. 4.2 graphically illustrates these results for various values of sigma, which determines the number of particles in the simulation. The analysis of the graph enables the deduction of Eq. 4.4 from the corresponding curve fitting. Subsequently, for calculating the surface tension in the simulation, the corresponding viscosity and density values were adjusted for each fluid. The Law of Laplace Eq. 2.55 was modified into Eq. 4.3, assuming that the pressure difference in the droplet is equal to the sum of internal forces between the particles, divided by the droplet's surface area. This allows substituting pressure in terms of the magnitude of interparticle forces and calculating the corresponding surface tension.

$$\gamma = \frac{\sum_{b=1}^{N} F_{ab}}{8\pi R} \tag{4.3}$$

This ensures that the pair potential not only simulates the internal pressure but also accurately represents the pressure difference between the liquid and the surrounding gas, making it possible to use this cohesive force at different length scales. This approach improves the reliability of the numerical method and the computational efficiency by the use of only the liquid phase.

$$\varepsilon = Constant \cdot \sigma^4 \tag{4.4}$$

The previous Eq. 4.4 was determined for a fixed volume, in this case 2 μL; However, when the volume increased, because the magnitudes of the forces associated with the

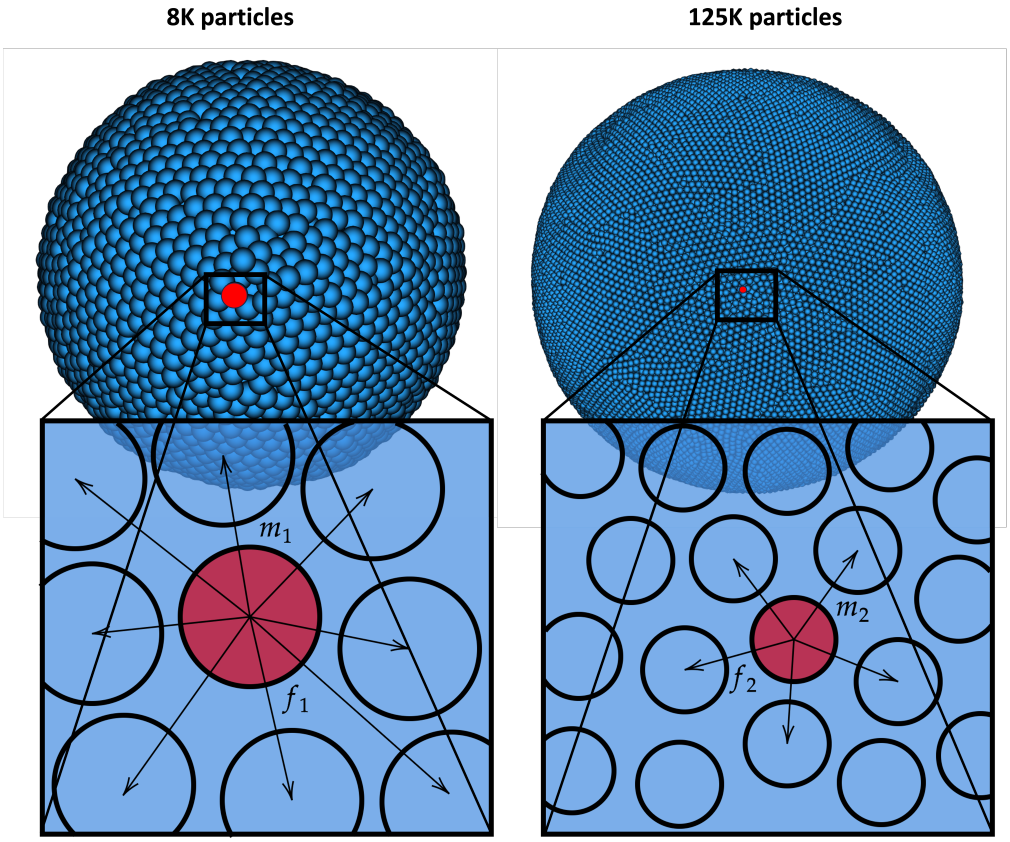

Figure 4.1: The figure shows how the magnitude of the interparticle force changes as the discretization is changed, but since the same physical system is being simulated, the net force must be the same, therefore, $c_1(f_1/m_1) = c_2(f_2/m_2)$, where c_i is a constant

mass changed (due to changing the discretization scale), it became necessary to introduce a term that allows scaling of the equation. The same process was used to find ε for larger volumes, with the same variation in the number of particles, and it was observed that the new relationship between ε and σ is Eq. 4.5,

$$\varepsilon = \frac{(Constant) \cdot \sigma^4}{L} \tag{4.5}$$

The dimensional analysis allows to establish ε's dependence on the simulation's physical parameters, obtaining the expression in Eq.4.6.

$$\varepsilon = \frac{S_f \cdot \mathrm{P}_{atm} \cdot \mathrm{V}}{\mathrm{L} \cdot np} \tag{4.6}$$

where S_f is a length factor, in meters. In our case, 1.5668×10^{-9}, P_{atm} is the atmospheric

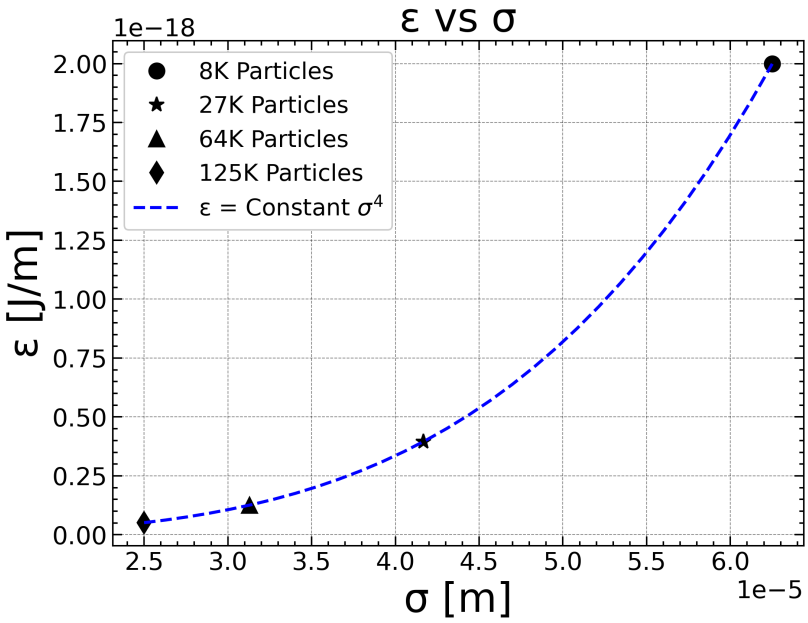

Figure 4.2: Relation between ϵ and σ at different number of particles

pressure, V the volume, and np the number of particles.

4.3 Validation and Discussion

The proposed simulation method for free surface has been validated through various three-dimensional tests. The SPH particles are initially arranged on a cube lattice with a spacing defined by $\sigma = L/n_x$, where n_x is the number of particles along L. Every simulation started from this initial configuration and was allowed to evolve over time until a stable state was achieved. Subsequently, gravity was either applied or not, depending on the specific scenario under consideration.

4.3.1 Formation of droplet: gas-liquid interaction

Therefore, in this work, we will take the evolution of particles from a cubic to a spherical shape in the absence of gravity as a validation test. This spherization process (in a Lagrangian point of view) is a consequence of the cohesive forces acting in the system and also replicate the behavior of the liquid by minimizing surface energy. So, during the process, the kinetic energy of the particles will be monitored, which, in order to be consistent with physical behavior, should tend to minimize.

Simulations were conducted with an initial volume of $2\mu L$, in the absence of gravitational forces, with particles initially arranged in a cubic configuration and subjected to the potential given by Eq. 4.1. In order to simulate different fluids, the initial reference

values for viscosity and density were changed. Subsequently, the values of the surface tension were obtained using the Y-L equation, Eq. 4.3

The Fig. 4.3 shows the evolution of 4.3a) water, 4.3b) ethanol, and 4.3c) ethylene glycol at different time steps of the simulation under the potential Eq. 4.1. From the figure, the scale of particle velocities represented in the color palette can be observed. Red indicates the maximum velocity of the system, which in our case is 0.694 m/s, and blue indicates the minimum of $\sim$ 0 m/s. During the spherization process, particles begin to move, as can be seen in the variation of velocity in figures 4.3 a), b), c) during time step 100. Subsequently, they tend towards a velocity close to zero in the later time steps, aiming to minimize energy and achieve a spherical shape. Additionally, no residual oscillating fluctuations around the equilibrium point are observed. Instead, the system tends towards velocities close to zero by time step 2500 in all cases, demonstrating consistency in the utilized potential function.

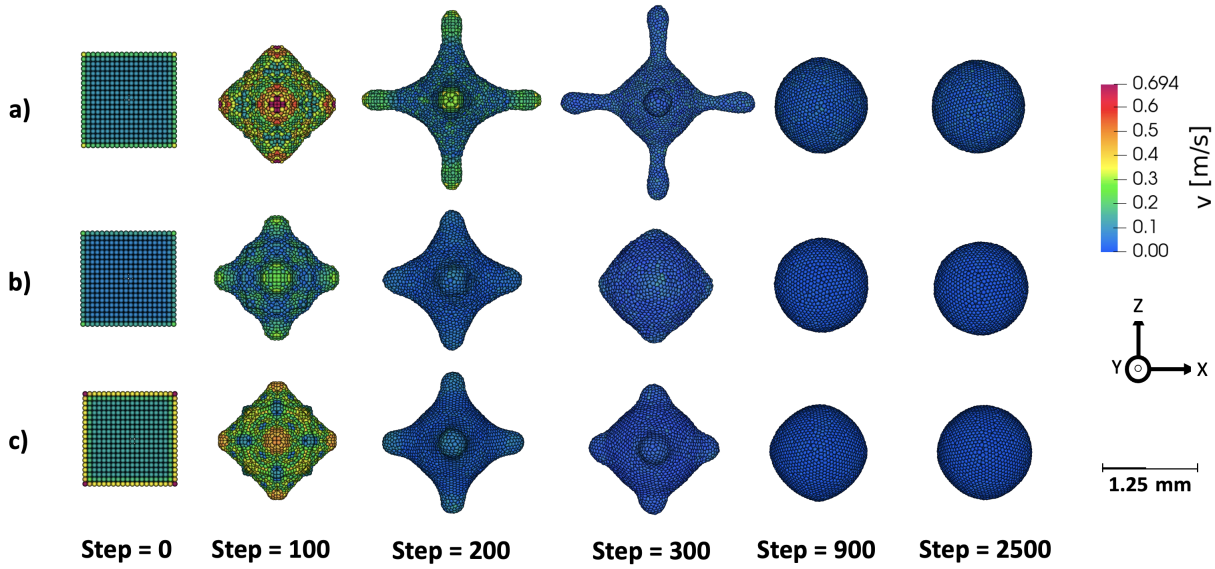

Figure 4.3: Relaxation process, from of an initially cubic shape to a droplet. The figures show snapshots of the droplet at increasing time steps, colored by velocity a) water, b) ethanol, c) ethylene glycol.

For the cases of water, ethanol and ethylene glycol, the results of evolution of density during the spherization process are presented in Fig 4.4. It can be observed in the graph for all cases, small fluctuations in density for the initial time steps, due to the movement of particles corresponding to the system's tendency to minimize energy. Subsequently, the density exhibit physically consistent behavior, with an average density of $987.2 \pm 0.51\,\mathrm{kg/m^3}$ for water, $771.3 \pm 0.25\,\mathrm{kg/m^3}$ for ethanol, and $1102.7 \pm 0.26\,\mathrm{kg/m^3}$ for ethylene glycol matching the theoretical values.

To determine the droplet's surface tension, the Eq. 4.3 was employed for each time step. The results for the analysis of the evolution of surface tension for the three fluids

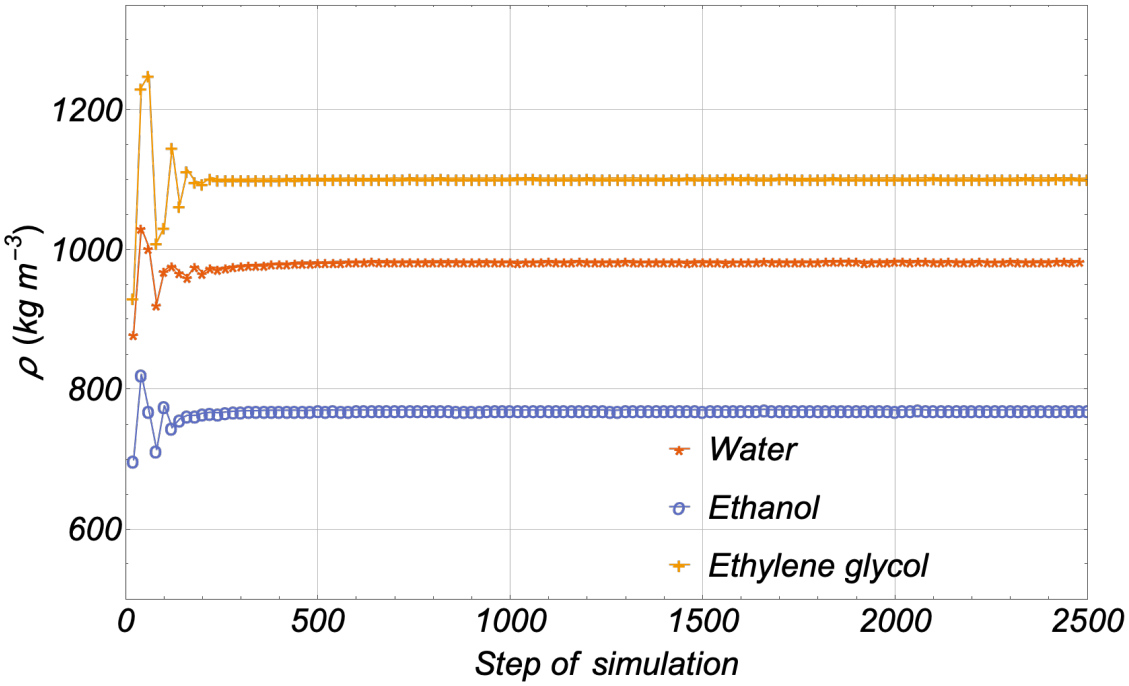

Figure 4.4: Density evolution of simulations of 2μL droplets for water, ethanol, and ethylene glycol with 8k particles

are shown in Fig 4.5. During the initial time steps in the spherization process, a decrease in the surface tension value is observed in all three cases, followed by stabilization at the corresponding value. This decrease is associated with the rearrangement of particles. They begin the simulation in a cubic arrangement, and during the spherization process, the system tends to minimize energy, causing particles to move and alter the value of internal inter-particle forces. This, in turn, affects the sum of forces between all particles and, therefore, the average pressure on the system Eq. 4.3. This effect creates small fluctuations observed in the graph, which then stabilize in the corresponding values after 1000 time steps.

In Table 4.1, a comparison between simulated and empiric surface tension values for three different fluids is presented. For water, the simulated value of $73.6 \pm 2.9\,\mathrm{mN/m}$ closely aligns with the empiric measurement of $72.8\,\mathrm{mN/m}$, leading to a relative error of only 1.19%. Similarly, the simulated surface tension of ethanol, $21.8 \pm 3.5\,\mathrm{mN/m}$, and that of ethylene glycol, $47.3 \pm 10\,\mathrm{mN/m}$, also show a close correspondence with their respective empiric values, resulting in relative errors of 1.47% and 1.30% respectively. Such minimal discrepancies in relative errors underscore the reliability and accuracy of the simulation. Furthermore, the provided standard deviations indicate the variability in simulations, with ethylene glycol showing the highest deviation, potentially caused

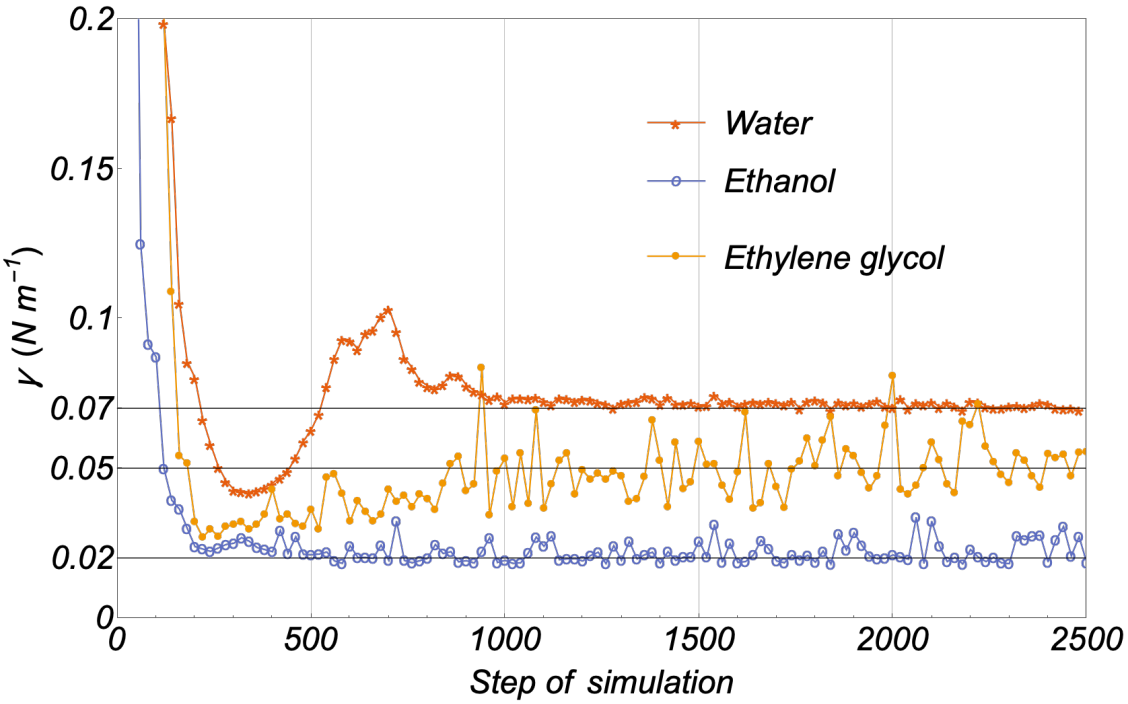

Figure 4.5: Graphic of surface tension values for water, ethanol, and ethylene glycol

by differences in viscosity, which in this case is an order of magnitude higher than that of water, but it still managed to spherize. Nevertheless, the observed spherization also attests to the adaptability and robustness of the employed potential. The referenced, [101], serve as trusted benchmarks to validate the outcomes of the simulation.

4.3.2 Droplet free-falling at different volumes and number of particles

To validate the utility of the potential, another test called the droplet fall test was employed. In these simulations, the process began with a cubic arrangement, allowing the droplet to stabilize until its spherization, followed by the application of gravity on the droplet. The surface used in all cases for the collision did not interact with the droplet, simulating a hydrophobic behavior. In Fig. 4.6, the case of two different volumes ($2\mu L$ and $2mL$) using 8K particles and water as the fluid is depicted. Fig 4.7 shows the same experiment but with 125K particles.

The behavior of free-falling droplets and their interaction with surfaces can be significantly influenced by the balance between internal and gravitational forces. This equilibrium is described by the dimensionless Bond number as previously was described. For the case with a volume of $2\mu L$, the calculated Bond number was 0.21. This suggests

Table 4.1: Surface tension values in mN/m: simulated and empirical values. The referenced values were acquired from [101].

Fluid	**Simulated Surface Tension (mN/m)**	**Empirical Surface Tension (mN/m)**	**Relative Error (%)**
Water	73.6 ± 2.9	72.8	1.19
Ethanol	21.8 ± 3.5	22.1	1.47
Ethylene Glycol	47.3 ± 10	47.9	1.30

that internal forces, primarily associated with surface tension, outweigh gravitational forces. As a result, the fluid must remain its spherical shape, forming a droplet on the surface without extensive spreading, as illustrated in Fig. 4.6.b) and 4.6.c). Conversely, with a larger volume of $2mL$, the Bond number rises to 21. This magnitude indicates that gravitational forces now surpass internal forces. As depicted in Fig. 4.6.e) and Fig. 4.6.f), the fluid tends to spread across the surface.

In Fig.4.7, simulations for free-falling of the droplets were revisited with a more refined discretization by increasing the number of particles to 125K, which essentially offers a higher resolution in capturing the fluid dynamics. This refined discretization resulted in more accurate representations of the physical properties of the fluid. In this case, as in the previous one, the behavior of spherization and spreading remained consistently in line with the Bond numbers associated with the volumes. The fluid must remain in its spherical shape, forming a droplet on the surface without extensive spreading, as is seen in Fig. 4.7.b) and 4.7.c). Conversely, with a larger volume of $2mL$, the Bond number increases to 21. For this case also the gravitational forces overcome the internals. As shown in Fig. 4.7.e) and Figure 4.7.f), the fluid tends to spread across the surface.

Analyzing the figures in Fig. 4.6.c) and Fig. 4.7.c), differences in contact angles are observed. Even though they involve the same liquid (water), these differences are associated with the fact that pairwise interactions between the solid and the fluid are not taken into account in simulations. This absence leads to variations in wetting shape and contact angle. The interactions between these two phases were modeled using the gosh particles approach, which produces a repulsive force between the particles near the boundary, preventing them from nonphysically penetrating through it [91, 102]. However, this approach does not consider the forces between the fluid and surface, which generate the formation of the contact angle.

Notably, despite the variations in the number of particles associated with changes in the discretization magnitude, from 8K particles Fig. 4.6 to 125K particles Fig. 4.7, physical properties such as density and surface tension remained consistent. These properties are graphically represented in Fig. 4.8 and 4.9.

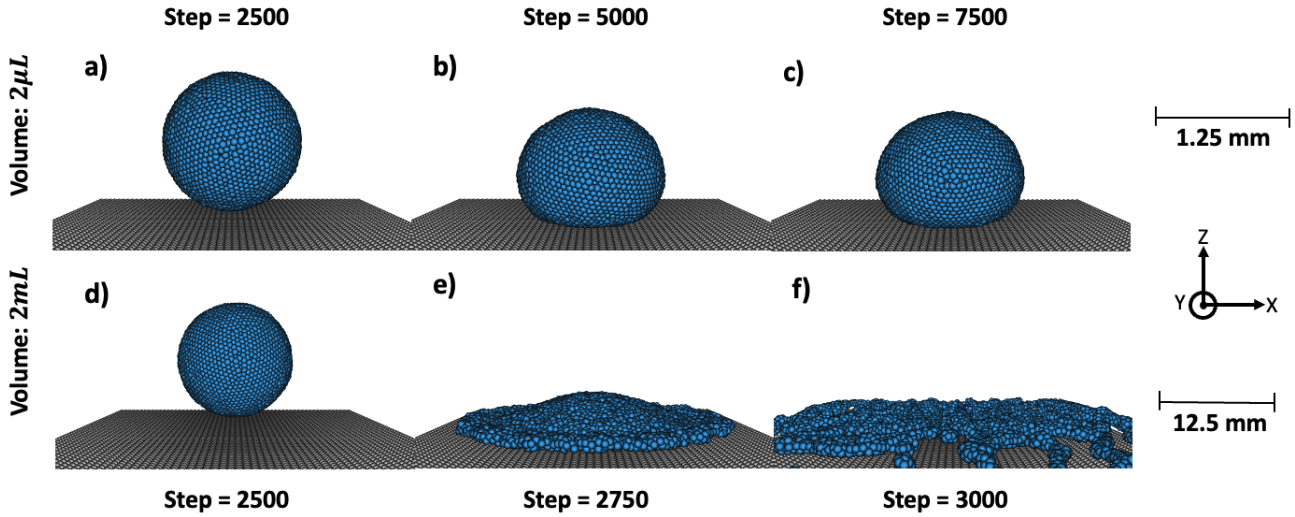

Figure 4.6: Graph screenshots of free-falling water volumes simulated with 8k particles. a) 2μL of water after relaxation, b) small volume touching the surface, $\gamma > g$, c) small volume forming a droplet. d) $2mL$ of water after relaxation, e) big volume touching the surface, $\gamma < g$, f) big volume splashing the surface.

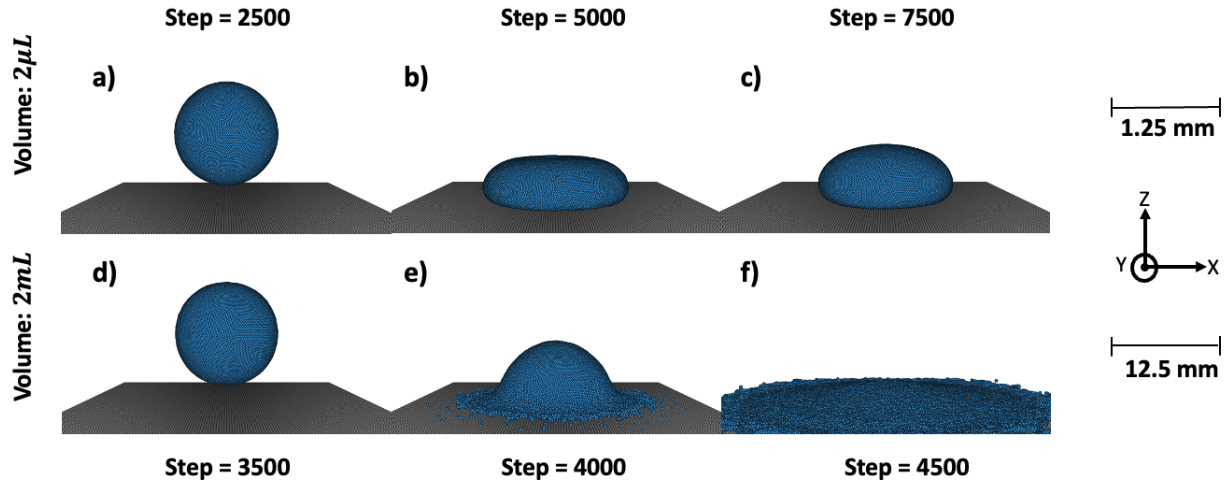

Figure 4.7: Graph screenshots of free-falling water volumes simulated with 125k particles. a) 2μL of water after relaxation, b) small volume touching the surface, $\gamma > g$, c) small volume forming a droplet. d) $2mL$ of water after relaxation, e) big volume touching the surface, $\gamma < g, f$) big volume splashing the surface.

Fig. 4.8 demonstrates noticeable precision in the average density measurements. For the $2\mu L$ volume before the collision, the density is determined to be $987.2 \pm 0.5\,\mathrm{kg/m^3}$ for the case of 8K particles and $991.8 \pm 0.3\,\mathrm{kg/m^3}$ for the case of 125K particles, with a relative error of 1.29% and 0.9%, respectively, over the entire simulation.

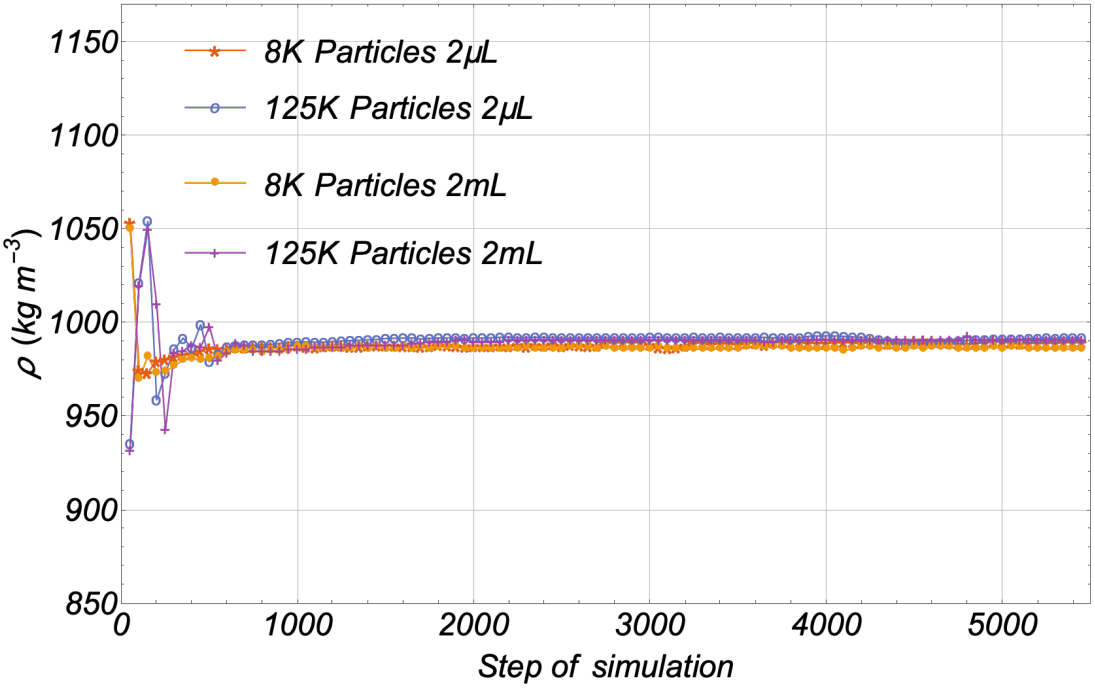

Figure 4.8: Density of 2μL and 2mL of water with 8K particles and 125K particles for each volume.

For the $2mL$ volume before the collision, the density is determined to be $986.3 \pm 0.5\,\mathrm{kg/m^3}$ for 8K particles and $990.8 \pm 0.4\,\mathrm{kg/m^3}$ for 125K particles, with a relative error of 1.38% and 0.92%, respectively. These results are summarized in Table 4.2. In this last case, fluctuations in density occur, after the collision as can be seen in the graphs after 2500 time steps for 8K particles and after 3500 steps for 125K particles.

These fluctuations occur because the density is calculated on average for the entire set of particles for each time step, and in the case when the Bond number is > 1, due to spreading, volumes with a low number of particles or small droplets affect the measurement of density.

The consistency in the physical properties, evidenced in the aforementioned figures, underscores the robustness of the developed method. It's clear that this approach is both versatile and precise enough to adapt to varying simulation conditions, affirming its applicability and reliability across a range of scenarios.

In Fig. 4.9, shows the results for the surface tension calculation. The values for the $2mL$ case were $73.1 \pm 0.46\,\mathrm{mN/m}$ for 8K particles and $74.8 \pm 2.1\,\mathrm{mN/m}$ for 125K

particles, with relative errors of 0.46% and 2.68%, respectively. For the $2\mu L$ case, the surface tension values were $73.6 \pm 2.9\,\mathrm{mN/m}$ for 8K particles and $73.2 \pm 2.1\,\mathrm{mN/m}$ for 125K particles, with relative errors of 1.18% and 0.54%, respectively. These results can also be found in Table 4.2.

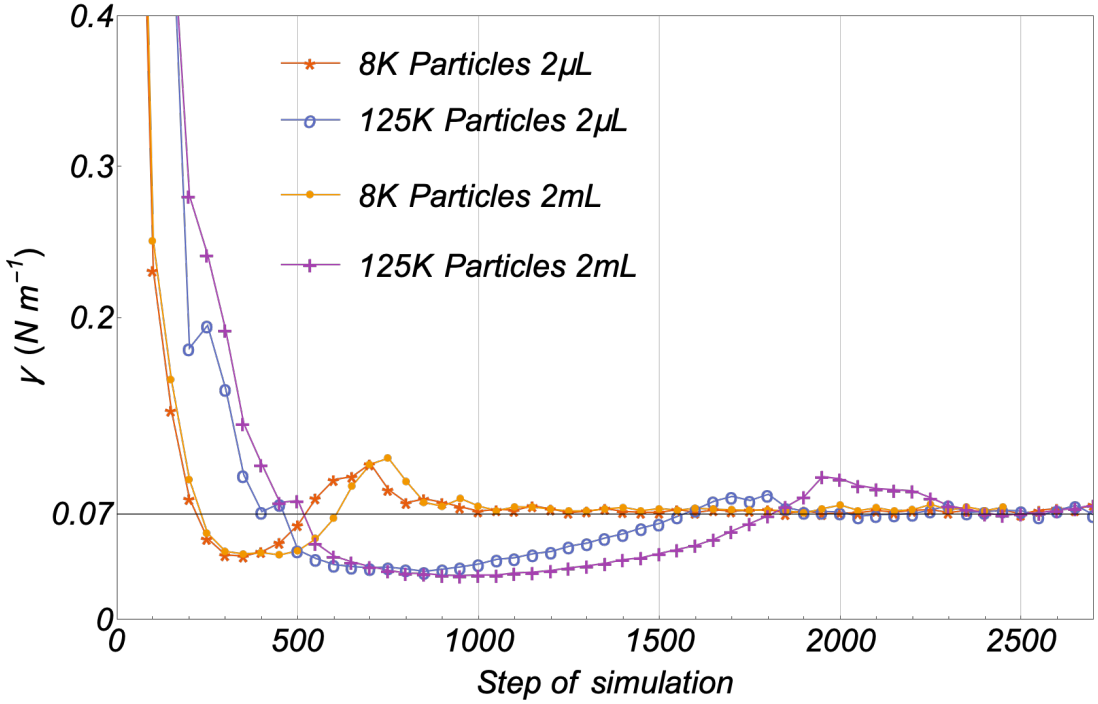

Figure 4.9: Graphic of surface tension values changing the number of particles for a droplet of water at 2μL and $2mL$

Similar to the density case, the graph exhibits fluctuations after 2500 time steps for the 8k particles case and 3500 time steps for the 125k particles case. These fluctuations are caused because the measurement of surface tension takes into account the radius of curvature and the average force summation of the entire particle set. In these experiments, after the droplet spreading, the measurement of the radius is altered, providing incorrect surface tension values.

4.3.3 Oscilation of droplet: gas-liquid interaction

Typically, the validation of droplet formation is carried out using classical literature, with Miller's two-dimensional droplet oscillation model [103] being one of the most commonly used. However, this model provides equations only for the two-dimensional case. Recently, Aalilija's [104] work also proposes a three-dimensional model for the droplet oscillation. The model solves the Navier-Stokes equation through an energy

Table 4.2: Surface tension and density values for different volumes and discretizations. Simulated and empirical values are compared. Reference values from [101] at room temperature.

Case	**Density** (kg/m^3)	**Density Error (%)**	**Surface Tension** (mN/m)	**Surface Tension Error (%)**
$2\,\mu L$, 8k particles	987.2 ± 0.5	1.29	73.6 ± 2.9	1.18
$2\,\mu L$, 125k particles	991.8 ± 0.3	0.90	73.2 ± 2.1	0.54
$2\,mL$, 8k particles	986.3 ± 0.5	1.38	73.1 ± 1.1	0.46
$2\,mL$, 125k particles	990.8 ± 0.4	0.92	74.8 ± 2.1	2.68

balance scheme, obtaining the solution for the radius of the free surface for an incompressible Newtonian liquid when a oscillation is induced. In Aalilija's work, the solution of the theoretical model is compared with a numerical Eulerian finite element model that solves the two fluid phases using a Variational MultiScale (VMS) stabilized finite element method proposed to solve the Navier-Stokes equations, including both mass conservation and momentum balance equations.

In this thesis, we use the theoretical model solution obtained in Aalilija's study as an additional way to validate our numerical results for a droplet oscillating from a defined condition to equilibrium in a damped model.

To achieve this, the equations of a Newtonian liquid can be considered through the Navier-Stokes equations, with density ρ and viscosity μ. In the model, the oscillations are measured over time by spatial evaluation of the surface at the liquid-gas interface Γ. The droplet is initially released in the first two modes (n=2) of the equation.

$$R(\theta, t = 0) = R_0(1 + \epsilon P_2 cos(\theta) + 0.2\epsilon^2) \tag{4.7}$$

Where P_2 is the second-order Legendre polynomial and in our case, $\epsilon = 0.01$, the droplet in the numerical SPH model was defined with a total of $125K$ particles and a diameter of 1.37 cm.

Fig. 4.10 presents a comparison between the numerical and theoretical results. In both cases, the droplet's equilibrium radius was 0.685 cm. The simulation was initialized with a small perturbation of 0.006 cm from the equilibrium radius, inducing oscillations that were compared to the theoretical model.

The results in Fig. 4.10 show that the average period of oscillation in the simulation was 0.18 s, compared to the theoretical period of 0.15 s. While the values are close to the theoretical predictions, with similar amplitude and frequency, an exact match between the numerical and theoretical solutions was not achieved. This discrepancy can be attributed to the fact that the theoretical model assumes an incompressible system, whereas the SPH simulations represent a quasi-incompressible system. These small differences in the period cause a slight phase shift between the two datasets.

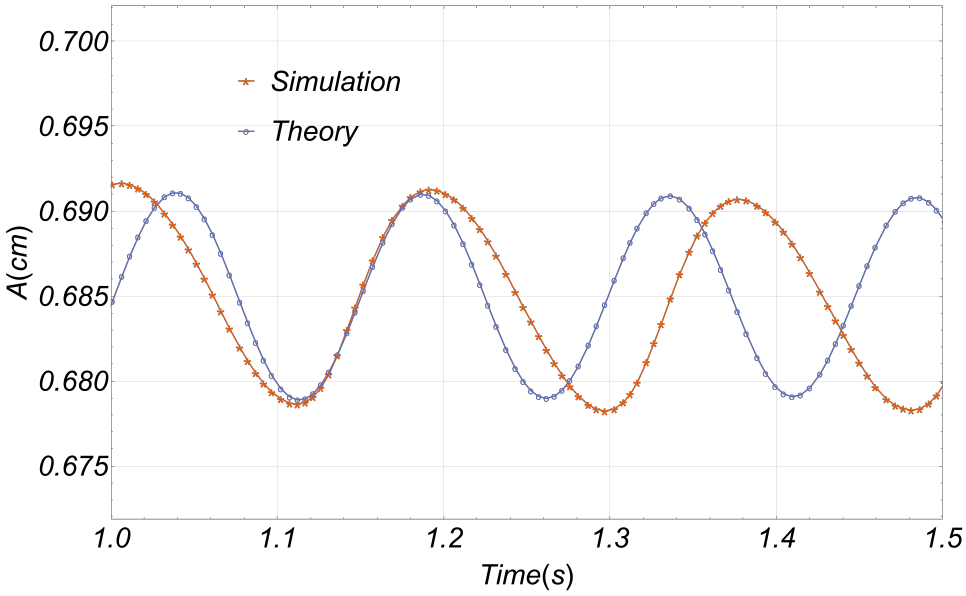

Figure 4.10: Graph of the theoretical and numerical droplet oscillations. The numerical conditions involved the use of $125K$ particles, with an average oscillation period of 0.18 s. The theoretical results are obtained from the plotting of equation (4.7).

4.3.4 Experimental Method

To validate the internal force approach proposed using SPH, we performed experiments to measure the surface tension of a fluid based on the stalagmometric method [105]. The stalagmometric method is a simple and accurate method to determine the surface tension of fluids that consists of measuring the weight of a pendant drop falling from a capillary tube. First, we determined experimentally the surface tension of three different fluids: distilled water, ethylene glycol and ethanol. Then we defined a method to compare the experimental results with the simulated results for a pendant drop.

Tate's Law establishes that the weight of a pendant drop is in an equilibrium state with the surface tension [105, 106]. This equilibrium state is described through the following equation

$$mg = 2\pi r\gamma, \tag{4.8}$$

where m is the mass of the drop, g is the acceleration of gravity, r is radius of the tube

and γ is the surface tension at the fluid-air interface. Therefore, the surface tension of the drop can be obtained as a function of the mass of the drop and the radius of the tube

$$\gamma = \frac{mg}{2\pi r}. \tag{4.9}$$

4.3.4.1 Experimental determination of the Surface Tension

To perform the measurements, we prepared an experimental setup that consisted of a vertical syringe of $1\,ml$ connected to a stainless steel tip of 16G, $1.6\,mm$ of external radius, and $1.25\,mm$ of internal diameter. The fluid moves along the syringe pushed by a vertical custom-made injection pump [107], whose injection flow rate was set at $Q = 85.1\,\mu l/min$ and controls the dripping frequency, $f = 0.053$ drops per second for distilled water, $f = 0.11$ drops per second for ethylene glycol and $f = 0.14$ drops per second for ethanol, these values ensure the formation of the drops avoiding leakage through the tip of the capillary. To collect the drops, we set a petri dish at a distance $d = 5\,cm$ from the tip of the tube. The images of the drops were obtained using a Panasonic Lumix DMC-FZ45 camera with a macros zoom, which records videos at 50 frames per second, and were analyzed using Image J (Fiji version 2.14.0/1.54f) [108]. The experimental setup is shown in figure. 4.11. Using Tate's Law, we measured

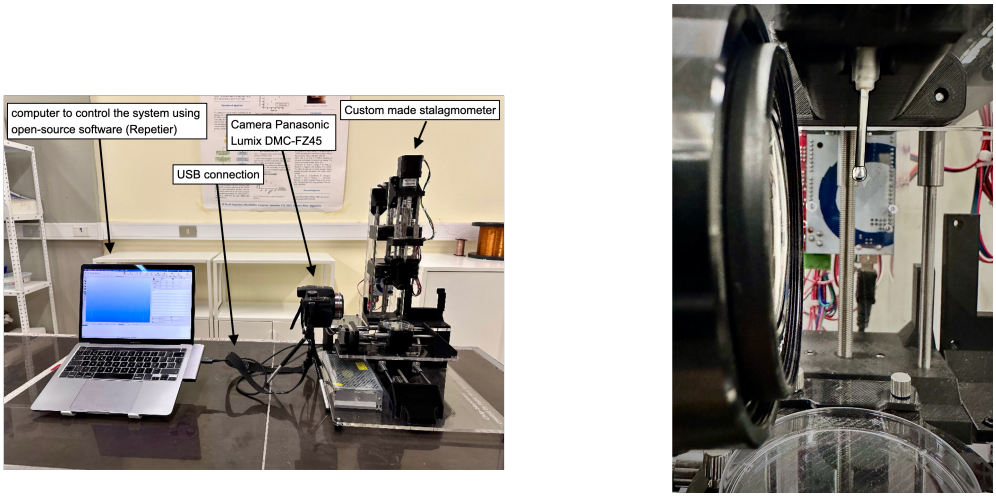

(a) (b)

Figure 4.11: (a) Photograph of the experimental setup. (b) Close-up of the drop at the moment of detachment.

experimentally the surface tension for three fluids with different densities: distilled water, $\rho_w = 998\,kg/m^3$; ethylene glycol, $\rho_{eg} = 1115\,kg/m^3$; and ethanol at 96%, $\rho_{et} = 807\,kg/m^3$. The experiments were performed at $18.4°C$. We performed ten repetitions of each experiment. We collected between eight and twelve drops for each experiment;

these were weighted with a precision scale (Kern ADJ 200-4) and divided by the number of drops to obtain the mass m of a single drop. Then, using eq. (4.9), we calculated the surface tension for each experiment and averaged it over the ten repetitions to obtain its value for each fluid. Table 4.3 shows the results obtained using Tate's Law. These

Table 4.3: The table shows the experimental results for the mean surface tension of the drops for the three different fluids obtained using Tate's Law, eq. (4.9).

Fluid	**Tate Law** $\gamma\,[mN/m]$ [105]	**Bibliographical** $\gamma\,[mN/m]$
Distilled water	70.9 ± 4.9	72.8 (20°C) [109]
Ethylene glycol	44.4 ± 0.5	47.7 (25°C) [109]
Ethanol	25.5 ± 2.6	22.4 (20°C) [110]

results show that the values are close to those expected [109, 110]. For distilled water, the accuracy is 2.6 %; however, the error increases to 6.7% for ethylene glycol and 14% for ethanol. The high error in ethanol measurements is likely due to evaporation between the drop deposition and weighting; ethanol's high volatility causes mass loss during this interval, leading to inaccuracies. In the case of ethylene glycol, the error is due to the high viscosity of the fluid, which may affect the detachment of the drop at the tip. Even though Tate's Law is a simple and accurate method, some corrections are recommended to obtain more accurate results. [1, 111–114].

4.3.5 Comparison between the experiment and the simulation

To validate the behavior of the internal force, we developed a method to compare the images of the drops recorded from the experiments with those obtained by the simulations. The method involves measuring the ratio, R, between the maximum diameter reached by the drop before detaching from the tip, D, and the inner diameter of the tube, d.

$$R = \frac{D}{d}. \tag{4.10}$$

According to the literature, to obtain accurate results, the ratio between the diameter of the tube and the ideal diameter of the drop must be within $0.6 - 0.9$ [1]. Therefore, for the experiments, we selected a tube with an inner diameter of 1.25 mm in order to observe only the interaction of internal forces (associated with surface tension) and gravitational force, as shown in Fig. 4.12. With smaller tube diameters, capillary effects appear, which are not included in the proposed approximation (solid-fluid interaction), and corrections are required to obtain accurate surface tension values.

The simulations were conducted with $170K$ fluid particles and $42K$ solid particles (which build the reservoir and the tip where the fluid comes out) with an inter-particles distance (σ) of 30×10^{-6} m. The inner diameter of the simulated tube was set at 240 μm,

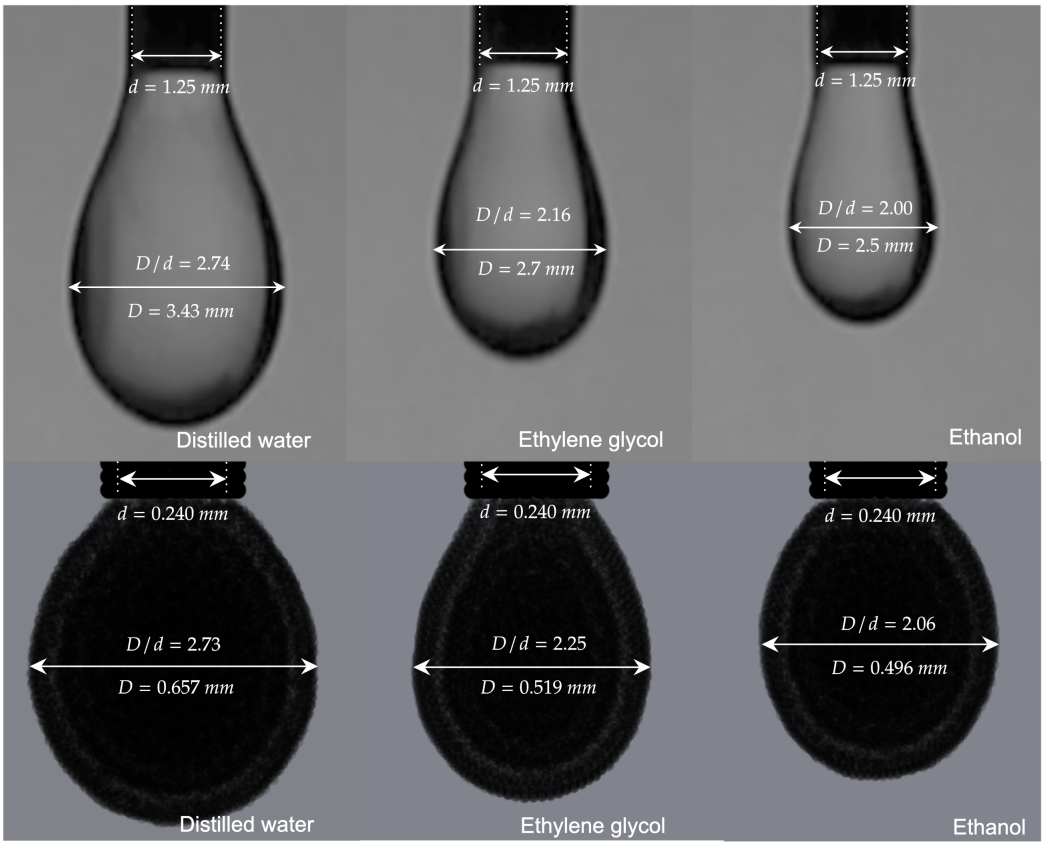

Figure 4.12: Comparison of the parameter $R = D/d$ between the experiments (top) and the simulations (bottom) for distilled water, ethylene glycol, and ethanol

and the wall thickness ratio (outer diameter/inner diameter) was replicated from the experiment and set at 1.3. A constant acceleration in the z direction of $79\,\mathrm{m/s^2}$ was applied to each particle to ensure that the fluids form drops instead of being ejected as a jet, which occurs when attempting to simulate a diameter greater than 1 mm, due to gravitational forces surpassing internal forces and causing the fluid to fall, it is the same phenomenon observed in experiments when dripping is not controlled. For each fluid, we measured the maximum diameter of each drop just before detachment from the tip, both for the experiments and the simulations. Then, we compared the ratios $R = D/d$ for the three fluids. The results presented in Table 4.4 show that the ratios for the experiments and the simulations are very similar, with an error of 0.36% for distilled water, 4% for ethylene glycol and 2.9% for ethanol. Figure 4.12 compares the experiments and the simulations of the maximum diameters reached by the different fluid drops before falling

It can be observed that as the surface tension of the fluids decreases, the maximum diameters reached (in both the experiments and the simulation) also decrease. This

Table 4.4: The table compares the maximum ratios reached by the fluid droplets in the experiments and the simulation.

Fluid	**Experiment** D/d	**Simulation** D/d	**Error** [%]
Distilled water	2.74 ± 0.02	2.73	0.36
Ethylene glycol	2.16 ± 0.08	2.25	4.00
Ethanol	2.00 ± 0.04	2.06	2.90

behavior occurs because, in fluids with higher surface tension, the cohesive forces are stronger, leading to a larger diameter before drop detachment compared to fluids with lower surface tension. The results in Table 4.4 confirm this trend, demonstrating that the internal forces associated with surface tension behave as expected.

4.4 Conclusion

An internal force has been introduced in the SPH model to replicate the cohesive interactions among fluid particles in a single-particle system, representing a multiphase (gas-liquid) phenomenon and resulting in surface tension effects. The Lagrangian approach focuses exclusively on the internal interactions within the liquid phase, enhancing computational efficiency by circumventing the need to simulate the gaseous phase. This approach involved determining a constant value of ε within the Wang potential, which allowed for the replication of droplet spherization as a validation method, as well as energy minimization and the evolution of surface tension over time. Additionally, it enabled simulations for Bond numbers both less than and greater than 1. This included reproducing drop formation on hydrophobic surfaces for a Bond number of 0.21, and the dispersion of fluid for a Bond number of 21, demonstrating the validity of cohesive internal forces that can be scaled for smaller or larger volumes.

To validate the model, the evolution of density and surface tension at various discretization scales was evaluated. In all cases, the values closely matched those reported experimentally.

Additionally, a comparison with the theoretical droplet oscillation model was carried out, revealing close agreement between the numerical and theoretical solutions. The pendant drop experiments also produced results consistent with the numerical simulations for the three fluids studied.

However, the proposed model does not account for the interaction of fluid flow with hydrophobic surfaces, leading to inconsistencies in the shape of the drop for different volumes. Therefore, further investigation of this interaction is necessary to improve the precision of the method. The proposed approach shows promise for various practical applications, including microfluidic simulation, droplet manipulation, splash simula-

tion, and the optimization of multiphase systems. Accurate surface tension modeling is crucial for understanding and optimizing these processes. The research highlights the practical implications of the developed approach. A similar study is needed to investigate the interaction between solid and fluid phases, which would enable a comparison of the computational model with experimental setups. The use of SPH in this model facilitates the physical representation of the liquid without the need for molecular-level discretization.

5 Microfluidic simulations

The increasing importance of microfluidic systems in areas such as biomedicine, material engineering, and chemical processing [46, 115] has driven the demand for precise simulation tools to support the research and development of advanced microfluidic technologies. In this context, the SPH method has established itself as a fundamental approach due to its ability to accurately capture complex phenomena at microscopic scales [5, 6, 25]. This is particularly evident in the simulation of fluid-fluid interactions mediated by interparticle potentials, such as the Wang potential [23].

In this chapter we focus on validating SPH simulations through comparisons with experiments. Such comparisons provide essential qualitative insights for assessing the accuracy and robustness of SPH models in reproducing microfluidic phenomena under various scenarios. By demonstrating the efficacy of SPH in simulating flows within microfluidic systems, our study reinforces the reliability of numerical simulations that incorporate particle interactions mimicking surface tension effects. This dual approach of simulation and experimentation not only fosters confidence in SPH models but also paves the way for further advancements in microfluidic research and the development of next-generation devices.

Furthermore, the integration of SPH-based simulations with experimental validation highlights the potential of combining computational and empirical methodologies to address challenges in microfluidic systems. This synergy supports the design and optimization of microfluidic devices for applications ranging from single-cell analysis to drug delivery, contributing significantly to the advancement of science and engineering in this domain.

5.1 Simulated Set up

For the simulations, we use the force interaction (Eq. 4.6) described in the chapter 4, which accurately models the surface tension of water. This variable is especially relevant in the simulation of fluids at small scales, where surface forces can even outweigh gravity (with a Bond number less than 1). Therefore, it is crucial to include this term in the momentum conservation equation to accurately simulate the dynamics of microchannels.

We simulated two microchannels with a width of $w = 1\,mm$ and two different heights, $h = 150\,\mu m$ and $h = 300\,\mu m$. The simulations were conducted with a particle spacing of $ds = 30 \times 10^{-6}\,\mathrm{m}$, using 170×10^3 fluid particles, 105×10^3 solid particles for the

microchannel of $150\,\mu m$ (Fig. 5.2a) and 111×10^3 solid particles for the microchannel of $300\,\mu m$ (Fig. 5.2b). These particles were placed in a reservoir to which a constant force was applied along the z-axis. This reservoir is connected via a "tube" with a radius of $4\,\sigma$ to a channel with a height of $5\,\sigma$ ($150\,\mu$m) and a width of $34\,\sigma$ (1mm), see Fig. 5.1.

To replicate experimental configurations that use hydrostatic pressures as the driving force for the fluid displacement [46, 81, 116] a fluid reservoir was positioned at a fixed elevation above the microchannel to generate the hydrostatic pressure driving the flow. The direct simulation of a full fluid column of comparable dimensions is computationally prohibitive due to the large number of particles required to maintain an adequate interparticle distance for the microchannels.

Therefore, to simulate the effect of hydrostatic pressure as the driving force of the fluid, we introduce a modified hydrostatic acceleration a_{ph_a} for each particle. This acceleration is computed at each time step using a normalized height ratio defined as

$$\frac{R_z - r_z}{R_z}, \tag{5.1}$$

where R_z is the height of the reservoir and r_z is the coordinate on the z-axis of the particle. This ratio is multiplied by a constant f_h to control the intensity of the acceleration. The resulting product is then multiplied by the local density ρ_a of each particle and the gravitational acceleration g. The final expression gives the hydrostatic acceleration (Eq.5.2).

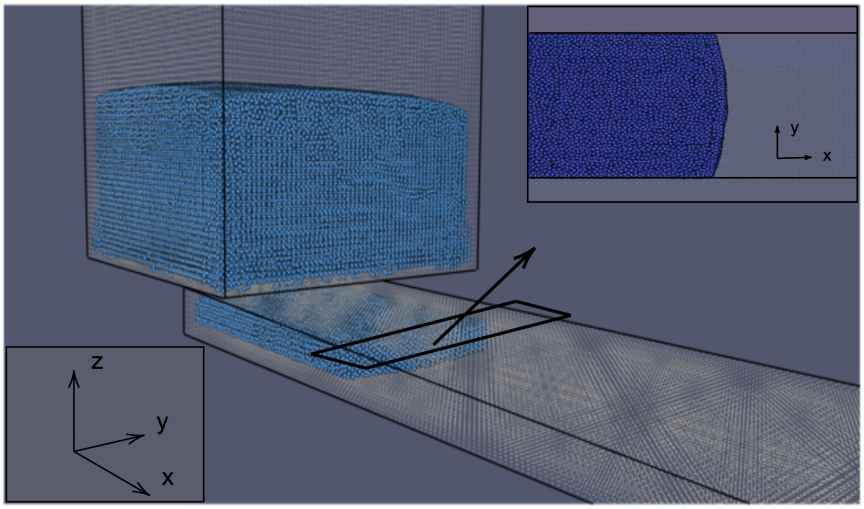

Figure 5.1: Simulation Set up

$$\mathbf{a}_{p_a} = \frac{\sigma^2\,\rho_a\,g}{m_a}\frac{(R_z - r_z)}{R_z} f_h \hat{\mathbf{z}} \tag{5.2}$$

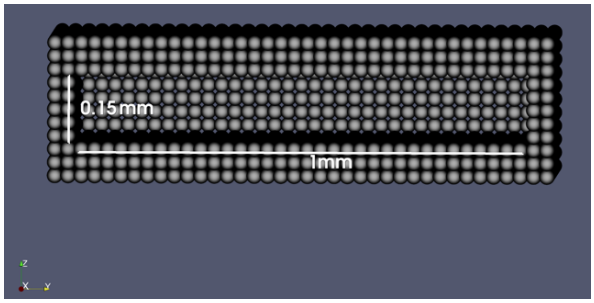

(a) $150\mu m$ of height and $1mm$ of wide simulted microchannel

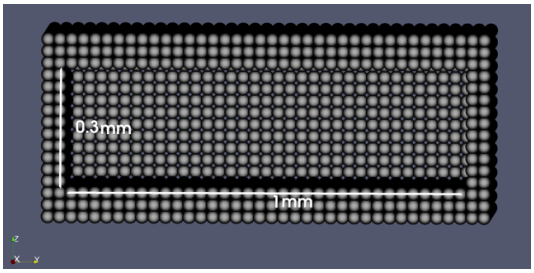

(b) $300\mu m$ of height and $1mm$ of wide simulted microchannel

Figure 5.2: Geometries of the simulated microchannels: (a) consists of 105×10^3 particles; (b) consists of 111×10^3 particles.

where a_{p_a} represents the acceleration associated with the hydrostatic pressure, f_h is a height factor with units in meters, R_z is the maximum height of the reservoir, and r_z is the height of particle "a" . Therefore, if particle "a" is at the maximum height of the reservoir ($r_z = R_z$), it will experience no pressure, while if it is at the lowest position ($r_z = 0$), it will feel the full pressure associated with the height f_h. Including the acceleration (Eq.5.2) in the Eq. 2.63, we have:

$$\frac{d\mathbf{v}_a}{dt} = -\sum_b \left(\frac{p_a + p_b}{\rho_a \rho_b}\right) \nabla_a W_{ab} + \Gamma_{ab} + \mathbf{F}_{int} + \mathbf{a}_{p_a} \tag{5.3}$$

$$\Gamma_{ab} = \sum_b m_b \left(\frac{4\nu r_{ab} \cdot \nabla_a W_{ab}}{(\rho_a + \rho_b)(r_{ab}^2 + \eta^2)}\right) (\mathbf{v}_a - \mathbf{v}_b) \tag{5.4}$$

$$\mathbf{F}_{int} = \frac{\partial}{\partial r}\left(\varepsilon\alpha \left(\left[\frac{\sigma}{r}\right]^2 - 1\right)\left(\left[\frac{r_c}{r}\right]^2 - 1\right)^2\right)\hat{r} \tag{5.5}$$

Where F_{int} is the internal force calibrated in chapter 4 and Γ_{ab} are the viscous forces associated with changes in relative velocities of the particle of interest ($mathpzca$) and neighboring particles (b).

5.2 Simulation Results

The primary objective of the simulations was to validate the capability of a SPH framework to model microfluidic flow in channels of different heights under varying pressure gradients. The simulations focused on understanding how a modified hydrostatic pressure, emulated through a height factor f_h, influences the fluid front propagation and internal flow dynamics.

From a theoretical perspective, microfluidic systems are highly sensitive to surface forces due to their small dimensions, making it essential to include surface tension

modeling. Since the filling process involves a transient front and a partially filled microchannel, the flow behavior aligns more closely with Darcy-type or Washburn models, rather than fully developed Poiseuille flow, which assumes a completely filled and steady-state regime.

Validation was carried out by comparing the simulated fluid front positions with theoretical predictions obtained from Eq. 2.37, which relates the advancement of the fluid front to the pressure drop and channel geometry.

The simulations were performed using a custom-built code in Python, accelerated via the Taichi library. The Weakly Compressible SPH (WCSPH) method was employed, incorporating surface tension effects via an interaction potential model. Water at 20°C was used as the working fluid, with standard density ($1000\,kg/m^3$) and viscosity values ($1 \times 10^{-6} mm^2/s$).

To simulate different driving forces, the height factor f_h was varied across three values: $1 \times 10^{-5}\,m$, $4 \times 10^{-5}\,m$, and $8 \times 10^{-5}\,m$. This variation resulted in different effective pressure gradients along the channel.

The inclusion of surface tension forces and a hydrostatic-like driving pressure enabled a realistic reproduction of microfluidic phenomena. The systematic variation of f_h allowed the exploration of a wide range of pressure-driven flow conditions, facilitating the evaluation of the SPH model's accuracy.

By ensuring a consistent comparison with the theoretical model, the simulations could be quantitatively validated. This validation is critical for confirming the model's predictive capabilities before extending its application to more complex fluid behaviors or non-Newtonian fluids.

5.2.1 Position vs Time

The evolution of the fluid front position over time is a critical indicator of flow dynamics within microchannels [81, 117, 118]. In these simulations, the focus was on analyzing how the fluid advances under different applied pressure gradients, modulated through the height factor f_h.

Fig. 5.3 presents a representative snapshot of the fluid front propagation obtained from the SPH simulations. The blue arrow indicates the direction of the advancing front, highlighting the dynamic nature of the filling process. This graphical representation is useful for illustrating how the SPH method captures the fluid interface evolution throughout the simulation domain.

The relationship between position and time in laminar, pressure-driven flow inside microchannels can be predicted using Eq. 2.37. This model accounts for the increasing hydraulic resistance as the fluid progresses along the channel, predicting a non-linear trend in the advancement rate due to viscous dissipation.

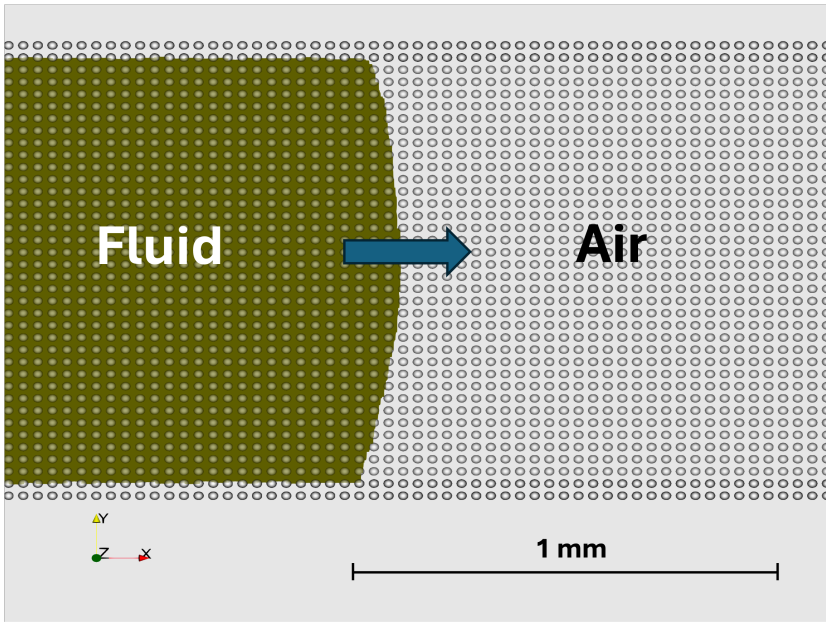

Figure 5.3: Snapshot of the fluid front propagation obtained from the SPH simulations. The filled particles represent the fluid phase, while the hollow indicate the air phase. The interface between the two phases is clearly visible, and the direction of fluid movement is indicated by the blue arrow.

$$x(t) = \frac{b^3 w\left(1 - 0.63\,\frac{b}{w}\right)}{12}\left\{\left[\left(\frac{8}{\pi}\frac{L}{r^4} + \frac{12}{b^3 w\left(1 - 0.63\,\frac{b}{w}\right)}x_0\right)^2 + \frac{24}{b^3 w^2\left(1 - 0.63\,\frac{b}{w}\right)}\frac{\Delta P}{\eta}(t - t_0)\right]^{1/2} - \frac{8}{\pi}\frac{L}{r^4}\right\}.$$

To enable comparison with the theoretical curve presented in Eq. 2.37, the pressure difference was obtained from the SPH equations, incorporating the modified hydrostatic pressure term used in the simulation. This pressure gradient, together with the same geometrical parameters used in both the simulation and the theoretical model, allowed ΔP to be calculated as a function of f_h.

At each time step, the position of the furthest fluid particle along the x-axis, representing the fluid front, was recorded. This provides a direct measurement of the penetration depth of the fluid into the microchannel as a function of time. For each simulated case, the effective pressure drop was calculated based on the imposed hydrostatic-like force derived from the height factor f_h. Fig.5.4 and 5.5 display the comparison between simulated and theoretical position-time curves (Eq. 2.37) for microchannels with heights of 150 μm and 300 μm, respectively.

Each figure includes the theoretical predictions based on Eq. 2.37 (Solid lines) for

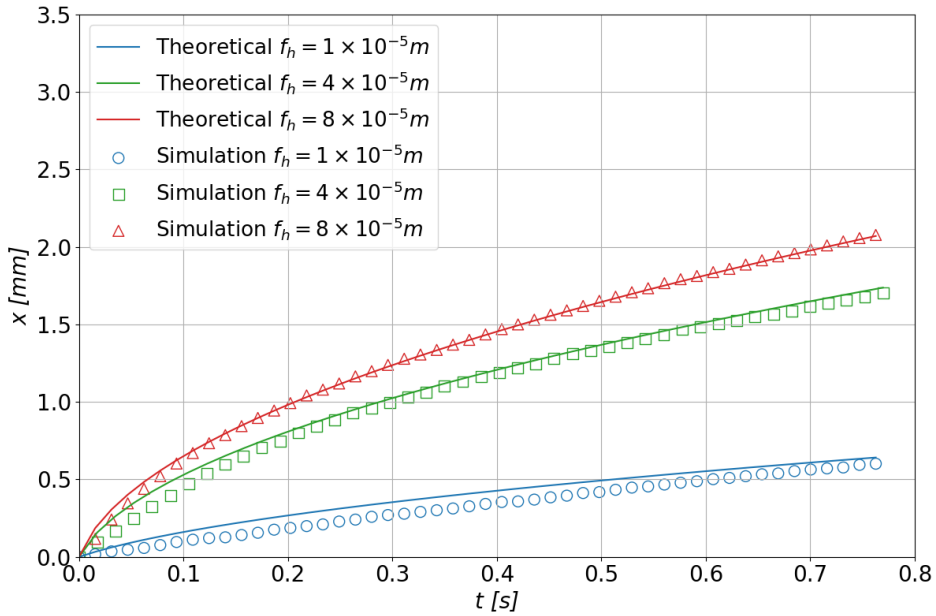

Figure 5.4: Comparison of simulation results and theoretical prediction (Eq.2.37) of fluid front position over time for a 150 μm high microchannel.

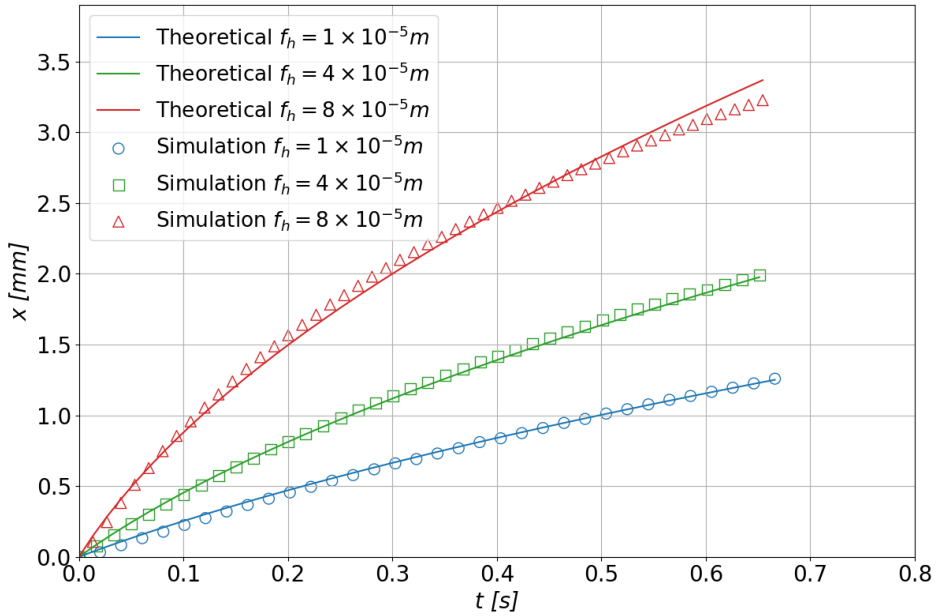

Figure 5.5: Comparison of simulation results and theoretical prediction (Eq.2.37) of fluid front position over time for a 300 μm high microchannel.

different f_h values and simulation results show the maximum x-position of the fluid front at discrete time intervals (Markers). Circles for $f_h = 1 \times 10^{-5}$, squares for $f_h = 4 \times 10^{-5}$ and triangles for $f_h = 8 \times 10^{-5}$,the x-axis represents time in seconds, while the y-axis shows the fluid front position in millimeters.

The results demonstrate a non-linear relationship between position and time, consistent with the theoretical model. For all cases, as time progresses, the fluid front advances at a decreasing rate, attributed to the increase in hydraulic resistance encountered by the fluid.

A strong agreement between simulations and theoretical predictions is observed, for $f_h = 1 \times 10^{-5}$, the advancement is slow, and both theoretical and simulation data exhibit a gradual increase in position over time. As f_h increases to 4×10^{-5} and 8×10^{-5}, the initial fluid velocities are higher, and the fluid front propagates more rapidly. Discrepancies between simulations and theoretical curves can be attributed to numerical resolution and small-scale fluctuations inherent in particle-based methods.

To evaluate the consistency between the theoretical model and simulation data, the Mean Squared Error (MSE) and coefficient of determination (R^2) were computed for each value of the height factor f_h, across two microchannel configurations. The results for the $150, \mu m$ microchannel are presented in Table 5.1, and those for the $300, \mu m$ microchannel are shown in Table 5.2. These metrics quantify the predictive accuracy and robustness of the model for capturing the fluid front dynamics under varying applied force conditions.

Table 5.1: Model validation for the $150\,\mu m$ microchannel

f_h	**MSE ($\mathbf{mm^2}$)**	R^2
1×10^{-5}	0.0046	0.8534
4×10^{-5}	0.0018	0.9917
8×10^{-5}	0.0004	0.9987

In the $150\,\mu m$ microchannel, increasing the value of f_h significantly improves the agreement between the theoretical prediction and the simulation. At the lowest value, the model underestimates the effect of the applied force, resulting in a larger discrepancy. As f_h increases, the model better accounts for the pressure-driven acceleration of the fluid, particularly in narrow channels where viscous and surface forces are more dominant. The best agreement is found at $f_h = 8 \times 10^{-5}\,m$, with an exceptionally low MSE ($0.0004\,mm^2$) and a high R^2 of 0.9987, indicating nearly perfect correlation.

In contrast, for the $300\,\mu m$ microchannel, the best performance is observed at $f_h = 1 \times 10^{-5}\,m$, with a minimal error and excellent correlation. This suggests that a lower applied force is sufficient to describe the filling dynamics in wider channels, where inertial and entrance effects are less restricted. Interestingly, increasing f_h beyond this value leads to a slight mismatch, as the model begins to overestimate fluid acceleration, especially at $f_h = 8 \times 10^{-5}\,m$, which shows the highest MSE ($0.0037\,mm^2$).

Table 5.2: Model validation for the $300\,\mu m$ microchannel

f_h	**MSE ($\mathbf{mm^2}$)**	R^2
1×10^{-5}	0.0002	0.9983
4×10^{-5}	0.0004	0.9988
8×10^{-5}	0.0037	0.9956

The simulations capture the expected trend; in the $150\,\mu$m microchannel, the fluid front reaches approximately $2.0mm$ at $0.75s$ for the highest f_h. In the $300\,\mu$m microchannel, the fluid front advances further, reaching nearly $3.0mm$ in around $0.65s$, reflecting the lower hydraulic resistance due to the larger channel height.

These results demonstrate that f_h, as a height factor, plays a critical role in tuning the model for accurate prediction of fluid propagation. In narrower geometries, a higher force factor is needed to overcome dominant resistance, whereas in larger channels, even moderate forces suffice to sustain the flow.

The position-time analysis confirms that the SPH simulations accurately reproduce the theoretical behavior of pressure-driven flow in microchannels. The methodology reliably captures the non-linear advancement dynamics and highlights the impact of varying f_h values on flow behavior. These results validate the SPH framework as a robust tool for simulating microfluidic phenomena under different pressure conditions.

The consistently high R^2 values—particularly above 0.99 in most cases—confirm that the theoretical framework captures the core physics of the system. The mean squared error remains below $0.005\,mm^2$ across all conditions, indicating excellent numerical fidelity. These findings support the validity of the model and demonstrate its suitability for simulating pressure-driven flow in microfluidic environments.

5.2.2 ΔP vs Velocity

A key feature of laminar flow in microchannels is the linear relationship between pressure drop (ΔP) and average fluid velocity ($\bar{v}$), as predicted by the Hagen–Poiseuille law for Newtonian fluids under fully developed conditions.

However, in the context of channel-filling processes, the flow is not yet fully developed, and the fluid front is still advancing. Despite this, if the flow remains laminar and the Reynolds number low, a quasi-steady approximation is valid, allowing the use of pressure–velocity proportionality to characterize the system dynamics [119].

Fig. 5.6 and 5.7 show the relationship between the effective pressure and the average fluid velocity for the $150\,\mu$m and $300\,\mu$m microchannels, respectively. Each point in the plots represents a different simulation with a distinct f_h value, translating into a different pressure gradient. The x-axis corresponds to the average velocity in millimeters per second , while the y-axis indicates the effective pressure in Pascals; the average velocity was computed by tracking the mean x-component of the velocity of

fluid particles along the channel.

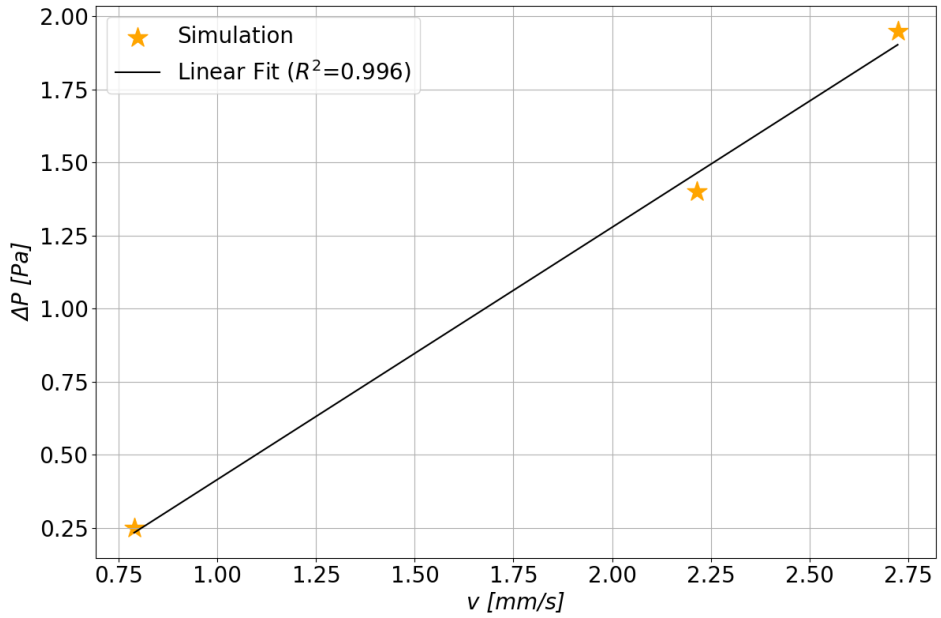

Figure 5.6: Simulated relationship between effective pressure and average velocity for the 150 μm high microchannel.

Both figures exhibit a clear linear trend between the effective pressure and the average velocity, confirming the laminar Newtonian nature of the flow. The linearity also indicates that viscous forces dominate the flow regime, with negligible inertial effects, as expected at microscale dimensions.

In the 300 μm microchannel, for a given pressure, the average velocity is higher compared to the 150 μm microchannel. This behavior is consistent with the theoretical prediction since hydraulic resistance is inversely proportional to the third power of the channel height; also, the slope of the pressure-velocity relationship is steeper for the 150 μm channel, reflecting higher resistance to flow. The excellent linear correlation between pressure and velocity in both cases with $R^2 = 0.996$ for 150 μm microchannel and $R^2 = 0.995$ for 300 μm microchannel, validates the hypothesis of Newtonian fluid behavior and laminar flow.

The delta pressure versus velocity analysis corroborates the theoretical expectation of linearity for Newtonian laminar flow in microchannels. The SPH model reliably reproduces the expected fluid dynamics for varying pressure gradients and channel heights, reinforcing its applicability for microfluidic simulations under different operational conditions. The minor deviations from perfect linearity may be attributed to local variations in flow velocities due to entrance effects and finite-size domain considerations.

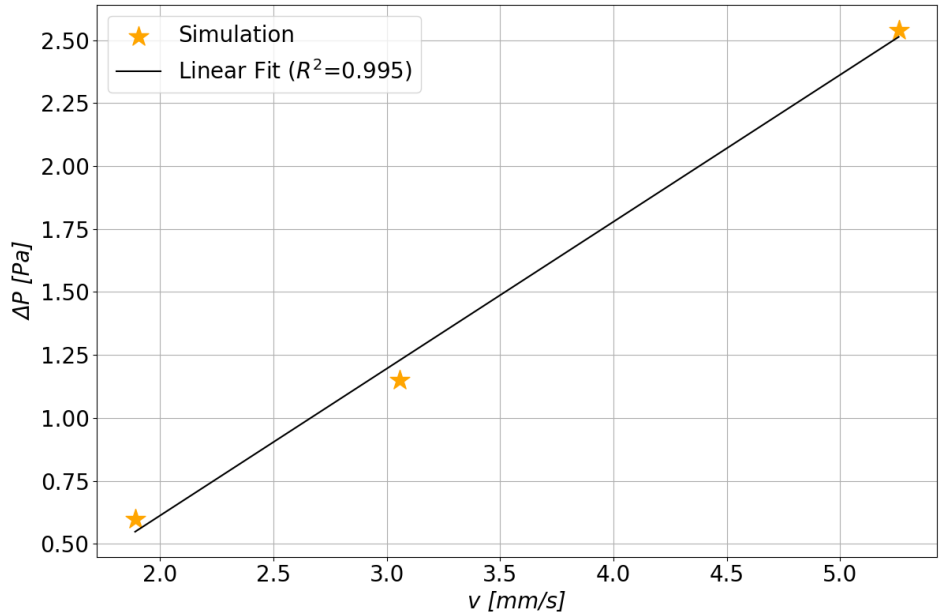

Figure 5.7: Simulated relationship between effective pressure and average velocity for the 300 μm high microchannel.

5.2.3 Reynlods vs Time

Another key aspect analyzed in the filling simulations was the estimation of the Reynolds number associated with the flow. In the context of channel-filling processes, the flow is not yet fully developed, and the fluid front is still advancing. Despite this, if the flow remains laminar and the Reynolds number low, a quasi-steady approximation is valid. As a result, the convective terms in the Navier–Stokes equation can be neglected, which simplifies both the analysis and the description of the system, allowing it to be treated under a regime dominated by viscous forces. [119, 120]. For very small organism, e.g., bacteria, the Reynolds number is very small, typically in the range of 10^{-6} and 10^{6} for a human [121]. Typical Reynolds number in microfluidics are lower than $Re < 10$ which ensures that the fluid remains in a laminar regime.[122]

These values were calculated using the velocities obtained and plotted as a function of normalized time, defined as $t/t_{\max}$, to enable comparison on a common scale. As observed in the Fig. 5.8, the Reynolds numbers obtained for the microchannel with a height of $h = 150\,\mu m$ exceeded 1 only in the interval $t/t_{max} < 0.2$ and exclusively for the simulated pressures of $f_h = 4 \times 10^{-5}\,m$ and $f_h = 8 \times 10^{-5}\,m$. However, after $t/t_{max} = 0.2$, the Reynolds number drops below 1, indicating that viscous forces become more significant than inertial forces in this regime. For the simulated pressure associated with $f_h = 1 \times 10^{-5}\,m$, the Reynolds number remained below 1 throughout the entire filling process, indicating that the flow was dominated by viscous forces. Overall, the highest Reynolds numbers were obtained for the filling associated with

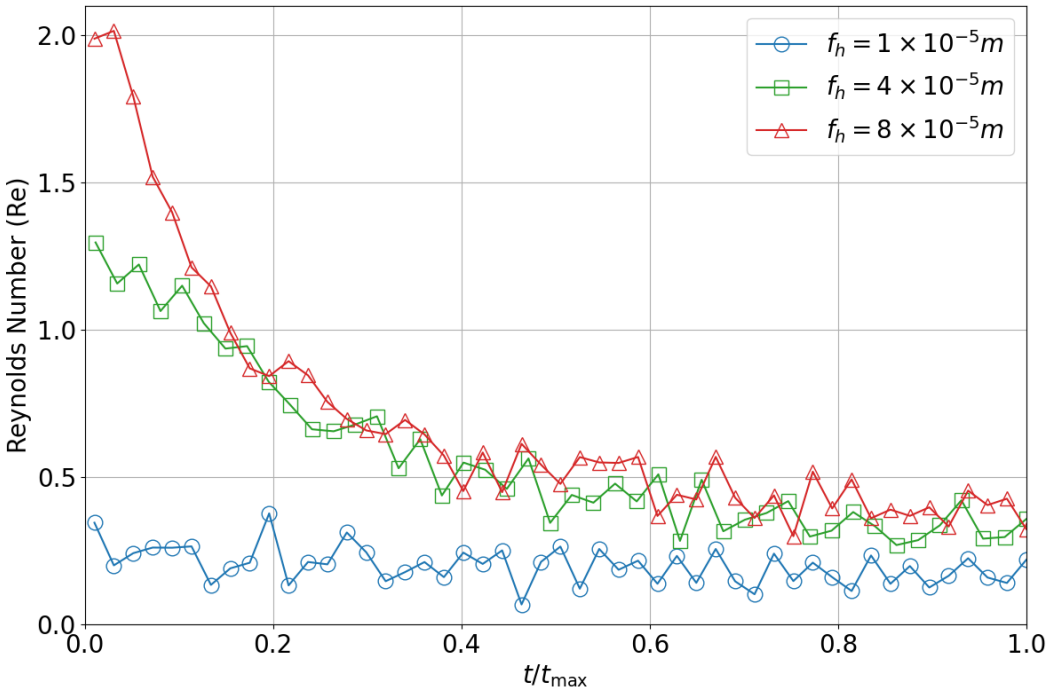

Figure 5.8: Estimated Reynolds number as a function of normalized time ($t/t_{\max}$) during the microchannel filling simulations for the 150 μm high microchannel.

the highest applied pressure ($f_h = 8 \times 10^{-5}\, m$), followed by those corresponding to the intermediate pressure ($f_h = 4 \times 10^{-5}\, m$). The lowest Reynolds numbers were recorded for the filling related to the lowest pressure ($f_h = 1 \times 10^{-5}\, m$).

In the case of the filling simulation for the 300 μm microchannel (see Fig. 5.9) , the highest Reynolds number corresponded to the filling with the highest simulated pressure, followed by the intermediate pressure, and finally the lowest pressure ($f_h = 1 \times 10^{-5}\, m$). Additionally, it was observed that the Reynolds numbers remained above 1 throughout most of the filling dynamics, with some exceptions: for the highest simulated pressure ($f_h = 8 \times 10^{-5}\, m$), the values dropped below 1 at some points towards the end of the filling; for the intermediate pressure ($f_h = 4 \times 10^{-5}\, m$), the values stayed above 1 until approximately $t/t_{max} < 0.6$; and for the lowest simulated pressure ($f_h = 1 \times 10^{-5}\, m$), the values remained close to 1, primarily for $t/t_{max} < 0.6$.

Finally, the Reynolds numbers estimated from the simulation confirmed that the filling process took place under laminar flow conditions ($Re < 2000$), as is typical in microchannel filling processes [123]. Even though the microchannels are highly sensitive to small changes, these variations do not affect the transitions of the Reynolds number, since it always remains in the laminar regime.

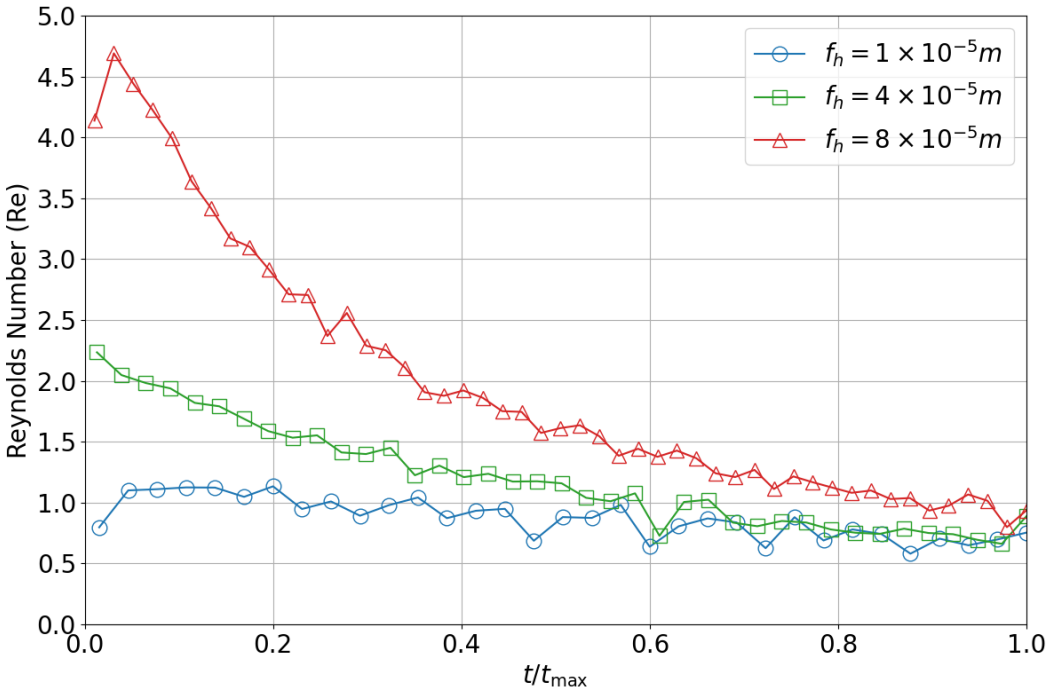

Figure 5.9: Estimated Reynolds number as a function of normalized time ($t/t_{\max}$) during the microchannel filling simulations for the 300 μm high microchannel.

5.2.4 Shear Stress vs Shear Rate

The relationship between shear stress and shear rate is fundamental for characterizing the rheological behavior of fluids [70]. For Newtonian fluids, this relationship is expected to be linear, with the slope corresponding to the dynamic viscosity. Investigating this relationship in microchannels allows for the validation of the fluid's Newtonian nature and the SPH model's ability to capture localized shear dynamics under pressure-driven flow.

For each simulation, the local shear rate was estimated using the expression $\dot{\gamma} = 6||\vec{v}|| \,/\, b$, where $||\vec{v}||$ represents the magnitude of the fluid front velocity at each time step, and b is the height of the microchannel. The corresponding shear stress τ was calculated based on the geometric characteristics of the system and the instantaneous fluid penetration distance x(t), according to the following expression:

$$\tau = \frac{\Delta p}{\left[\frac{4}{3\pi}\left(\frac{Lb^2 w}{r^4}\right) + \frac{2x(t)}{b\left(1-0.63\frac{b}{w}\right)}\right]}$$

where Δp is the applied pressure drop (associated with each f_h), L is the length of the connecting tube, and r is the tube radius. This formulation accounts for both the resistance of the connecting tube and the evolving hydrodynamic resistance within

the microchannel as the fluid advances. Measurements were taken at various positions along the channel to capture spatial variations in flow conditions.

Fig. 5.10 and 5.11 illustrate the computed shear stress versus shear rate for the 150 μm and 300 μm microchannels, respectively. Each plot displays data points obtained from different simulations, with circles representing the case $f_h = 1 \times 10^{-5}\, m$, squares for $f_h = 4 \times 10^{-5}\, m$, and triangles for $f_h = 8 \times 10^{-5}\, m$. A dashed line indicates the global linear fit applied to all data points, where the slope corresponds to the estimated viscosity η (which corresponds to the ratio between σ and $\dot{\gamma}$), and the coefficient of determination R^2 quantifies the goodness-of-fit of the linear model.

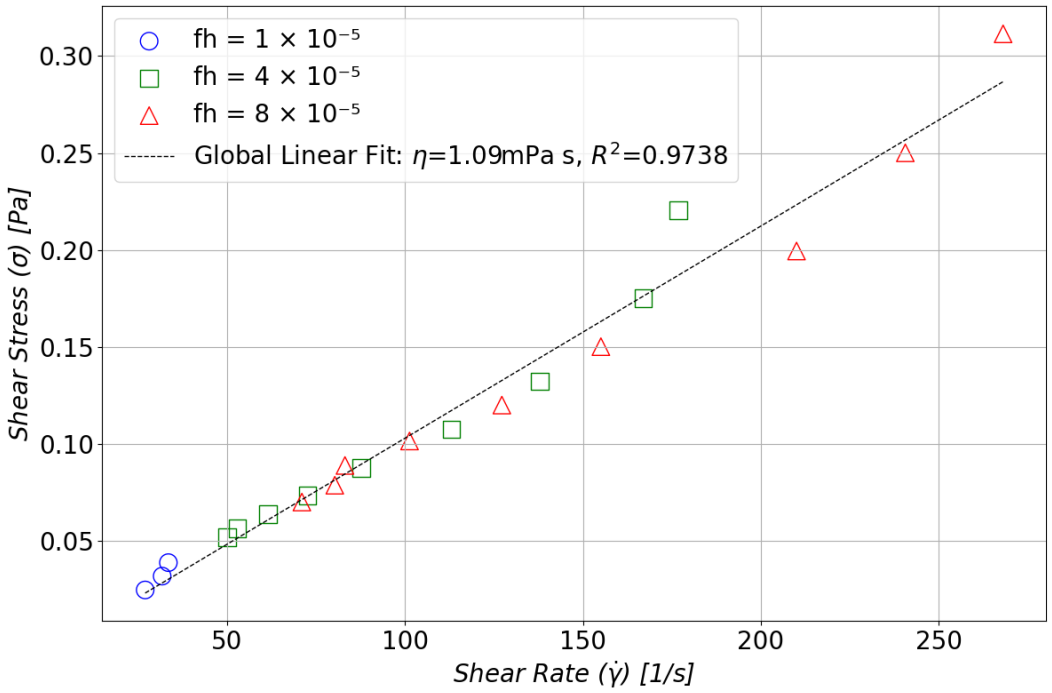

Figure 5.10: Shear stress vs. shear rate for the 150 μm high microchannel.

The plots reveal a predominantly linear relationship between shear stress and shear rate for both the 150 μm and 300 μm microchannels, confirming the Newtonian behavior of the fluid under the simulated conditions. This linearity supports the assumption of constant viscosity. The 300 μm microchannel displays a broader range of shear rates compared to the 150 μm channel, a result consistent with its lower hydraulic resistance and the higher velocities achieved in taller channels. In contrast, the 150 μm microchannel exhibits a more constrained shear rate distribution, reflecting the stronger viscous damping and more uniform flow conditions imposed by its geometry.

Quantitatively, the estimated viscosity from the global linear fit for the 150 μm microchannel is 1.09 mPa $\cdot$ s, with a coefficient of determination $R^2 = 0.9738$. For the 300 μm microchannel, the viscosity is slightly lower at 0.93 mPa $\cdot$ s, with a higher goodness-of-fit ($R^2 = 0.9968$). These values are in close agreement with the theoretical

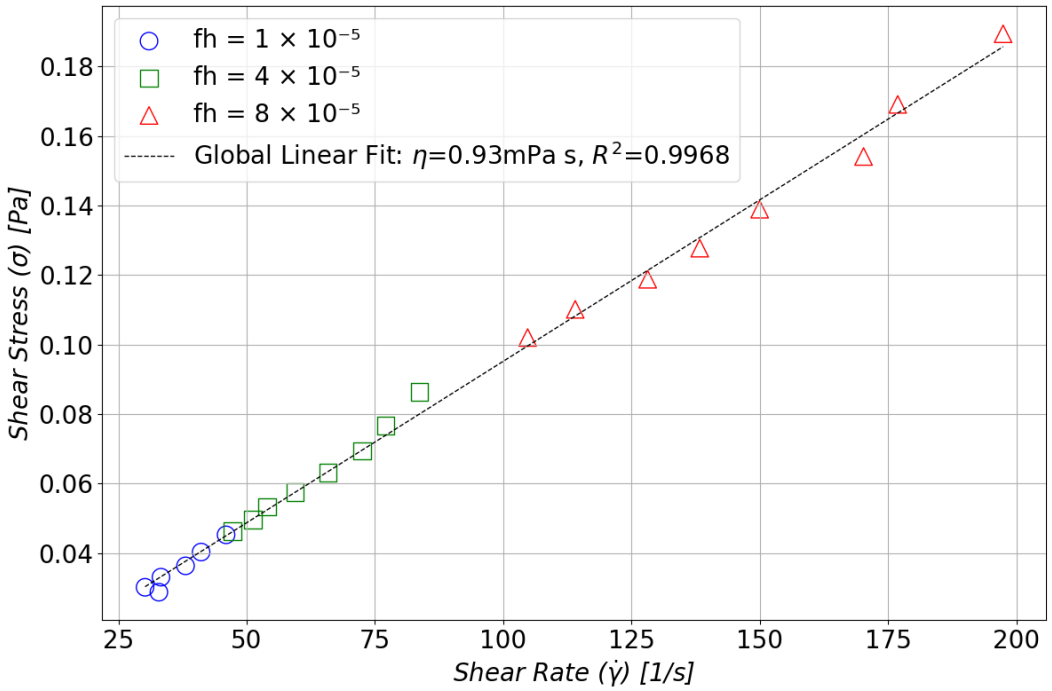

Figure 5.11: Shear stress vs. shear rate for the 300 μm high microchannel.

viscosity of water at 20°C (1.00 mPa·s) [124], confirming the accuracy of the simulation framework in reproducing expected rheological properties.

The shear stress versus shear rate analysis confirms the Newtonian behavior of the simulated fluid across both microchannel geometries. The SPH simulations accurately reproduce the expected linear relationship, demonstrating the model's ability to capture detailed rheological behavior under varying shear conditions. The estimated viscosities align closely with the theoretical value of water at 20°C, and the high coefficients of determination (R^2) reflect excellent agreement with the linear model.

Notably, the high R^2 values further reinforce the validity of the Newtonian assumption and highlight the effectiveness of the SPH method in capturing the linear viscous response of the fluid. Minor scatter observed in the data, particularly at higher shear rates or near the microchannel walls, is likely attributable to local velocity fluctuations and the discretized nature of the SPH approach, where sharp gradients are more sensitive to particle resolution.

These findings validate the robustness of the SPH framework for microscale flow simulations, showing that it can accurately resolve spatial variations in stress and shear rate without introducing numerical artifacts indicative of non-Newtonian effects. The observed consistency in viscosity across different pressures and channel geometries underscores the reliability of the method for modeling Newtonian fluid dynamics in confined microfluidic systems.

5.2.5 Viscosity

In Newtonian fluids, viscosity η remains constant regardless of the applied shear rate or local flow conditions [70]. Verifying that the viscosity remains spatially uniform along the microchannel and across different flow regimes is essential for confirming the Newtonian behavior of the fluid and the reliability of the SPH numerical method.

The viscosity was calculated at different positions along the microchannel, based on the local values of shear stress and shear rate. Multiple simulations with varying height factors f_h were conducted to evaluate the influence of different pressure gradients on the viscosity measurements.

$$\eta = \frac{\Delta P}{\left(\dot{x(t)}\right)\left[\frac{8}{\pi}\left(\frac{Lb^2w}{r^4}\right) + \frac{12x(t)}{b^2\left(1-0.63\frac{b}{w}\right)}\right]}$$

Fig. 5.12 and 5.13 show the viscosity distribution along the microchannel for heights of 150 μm and 300 μm, respectively. Each figure presents the viscosity values calculated at discrete positions along the channel for different values of f_h. Circles represent $f_h = 1 \times 10^{-5}\, m$, squares correspond to $f_h = 4 \times 10^{-5}\, m$, and triangles indicate $f_h = 8 \times 10^{-5}\, m$. A dashed line in each figure shows the average viscosity (η_{prom}) along with its associated standard deviation.

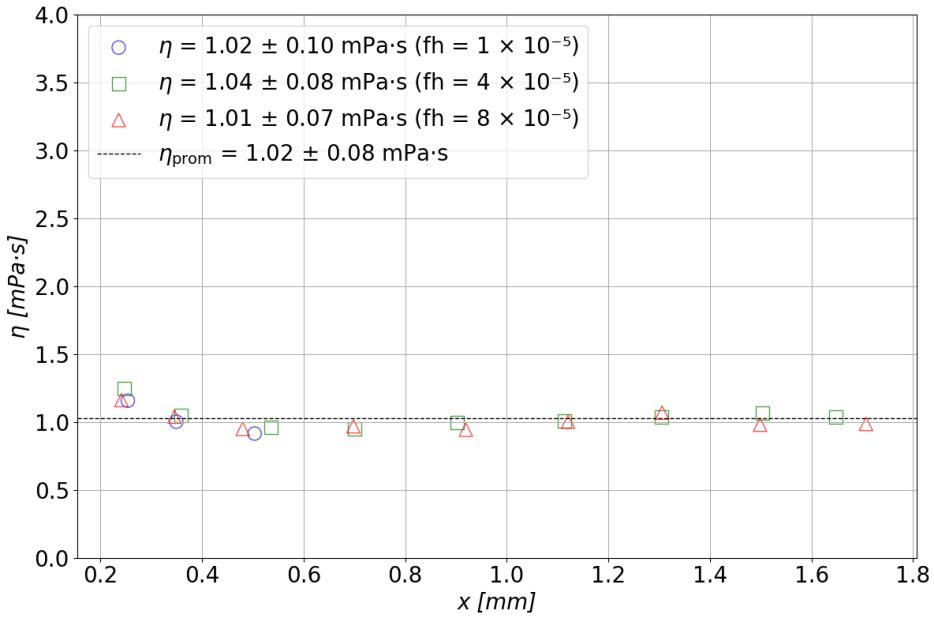

Figure 5.12: Evolution of viscosity along the 150 μm high microchannel. Average viscosity: 1.02 ± 0.08 mPa s.

The results show that the average viscosity in the 150 μm channel is 1.02 ± 0.08 mPa s, while in the 300 μm channel it is 0.96 ± 0.03 mPa s. Both values are in excellent agree-

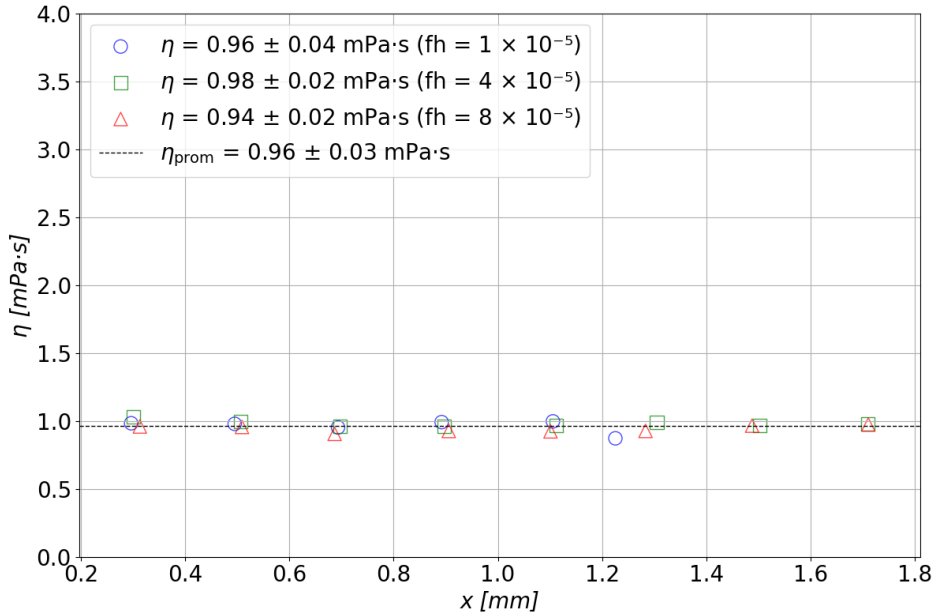

Figure 5.13: Evolution of viscosity along the 300 μm high microchannel. Average viscosity: 0.96 ± 0.03 mPa s.

ment with the theoretical dynamic viscosity of water at 20°C (1.00 mPa s). The small variations observed along the channel fall within acceptable numerical precision limits for SPH simulations.

Importantly, no significant variation in viscosity is observed along the length of either channel (see table 5.3), indicating that changes in shear rate do not affect viscosity, as expected for Newtonian fluids. Furthermore, the relatively low standard deviations observed confirm the consistency and reliability of the numerical approach across different flow conditions and geometries.

Table 5.3: Viscosity values obtained for different f_h in each microchannel

Microchannel Height (μm)	f_h ($\times 10^{-5}$)	**Viscosity** ($\eta \pm \Delta\eta$) **(mPa·s)**	**Viscosity Average (mPa·s)**
150	1	1.02 ± 0.10	1.02 ± 0.08
	4	1.04 ± 0.08	
	8	1.01 ± 0.07	
300	1	0.96 ± 0.04	0.96 ± 0.03
	4	0.98 ± 0.02	
	8	0.94 ± 0.02	

To further validate the SPH simulation framework, the viscosity was analyzed for different Newtonian fluids: water, ethanol, and ethylene glycol. Each of these fluids

possesses distinct molecular properties that influence their dynamic viscosity, and verifying that the simulations capture these differences accurately is essential to assess the model's versatility.

At 20°C, the theoretical dynamic viscosity is approximately 1.00 mPa s for water, 1.20 mPa s for ethanol, and 16.1 mPa s for ethylene glycol[124]. The local dynamic viscosity was calculated along the microchannel for each fluid using the same methodology applied in the water simulations. The resulting profiles were evaluated to assess spatial consistency and confirm that each fluid maintained the expected constant viscosity.

Fig. 5.14 presents the viscosity distribution for water, ethanol, and ethylene glycol along the 300 μm high microchannel. In this plot, circles denote water, asterisks represent ethanol, and crosses correspond to ethylene glycol. The horizontal axis shows the position along the channel in millimeters, while the vertical axis displays the computed viscosity in mPa s.

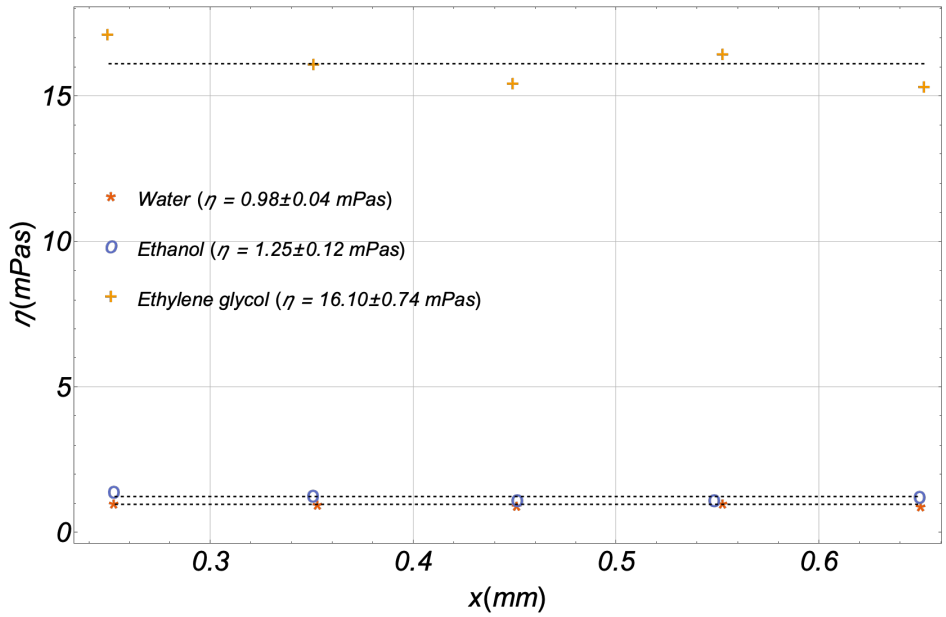

Figure 5.14: Viscosity evolution along the 300 μm high microchannel for water, ethanol, and ethylene glycol. The dotted lines indicate the mean viscosity values obtained from the simulations for each fluid.

The results show that water maintains a viscosity close to 1.00 mPa s along the channel with minimal variation. Ethanol exhibits a slightly higher viscosity, consistent with its known rheological properties, while ethylene glycol shows a significantly higher viscosity (approximately an order of magnitude greater) corresponding well with theoretical expectations. In all cases, the viscosity remains stable along the length of the microchannel, confirming the absence of shear-rate dependence. The consistency of these profiles reinforces the Newtonian behavior of the fluids under the simulated

conditions, and minor fluctuations observed are within acceptable numerical resolution limits, not affecting the overall trends.

The viscosity measurements confirm that the fluid maintains a constant viscosity along the microchannel, consistent with Newtonian fluid behavior. The SPH simulations accurately reproduce the expected rheological properties, validating the model's robustness for studying microfluidic flows under a range of operational conditions. The viscosity analysis for different fluids confirms that the SPH framework accurately captures the distinct rheological properties of Newtonian fluids with varying viscosities.

5.3 Nonlinear Behavior Analysis

The aim of this analysis is to characterize the nonlinear behavior of the fluid front as it advances through microchannels under different applied pressures. In pressure-driven microfluidic systems, the evolution of the front position over time is governed by a balance between driving pressure and hydrodynamic resistance due to viscous dissipation.

Washburn's law [83] provides a theoretical framework for this behavior, predicting that in a viscous-dominated regime, the front position x scales with the square root of time t, i.e., $x \sim t^{0.5}$. Verifying this scaling behavior in the simulations is essential for confirming that the fluid dynamics are correctly captured, especially under varying pressure gradients and channel geometries.

The maximum front position along the x-axis was recorded as a function of time for different applied pressure conditions, which were controlled by adjusting the height factor f_h. To analyze the dynamics of the fluid front, a power-law model of the form $x(t) = A\,t^n$ was fitted to the simulation data, allowing extraction of the scaling exponent n and prefactor A under each experimental condition.

Fig. 5.15 presents the resulting fits for a range of pressure values and microchannel heights. The left column corresponds to microchannels with a height of 150 μm, while the right column displays data for microchannels with a height of 300 μm. Within each column, the rows represent increasing inlet pressure values, specifically $f_{h1} = 1 \times 10^{-5}$ (top), $f_{h4} = 4 \times 10^{-5}$ (middle), and $f_{h8} = 8 \times 10^{-5}(bottom)$. Each subplot includes gray markers that indicate the simulated data points for the fluid front position over time, and a red line representing the corresponding power-law fit. The equation of the fitted curve is also displayed within each plot for reference.

The fitted results demonstrate a clear trend in the evolution of the scaling exponent n as a function of pressure. At low inlet pressures ($f_h = 1 \times 10^{-5}$), the exponent is close to 0.88 for the 150 μm channel and 0.87 for the 300 μm channel, indicating near-linear advancement of the fluid front with limited viscous resistance. As the applied pressure increases, the exponent gradually decreases, approaching values closer to 0.5. Under the highest applied pressure conditions ($f_h = 8 \times 10^{-5}$), the exponent reaches approximately 0.58 in the 150 μm channel and 0.65 in the 300 μm channel.

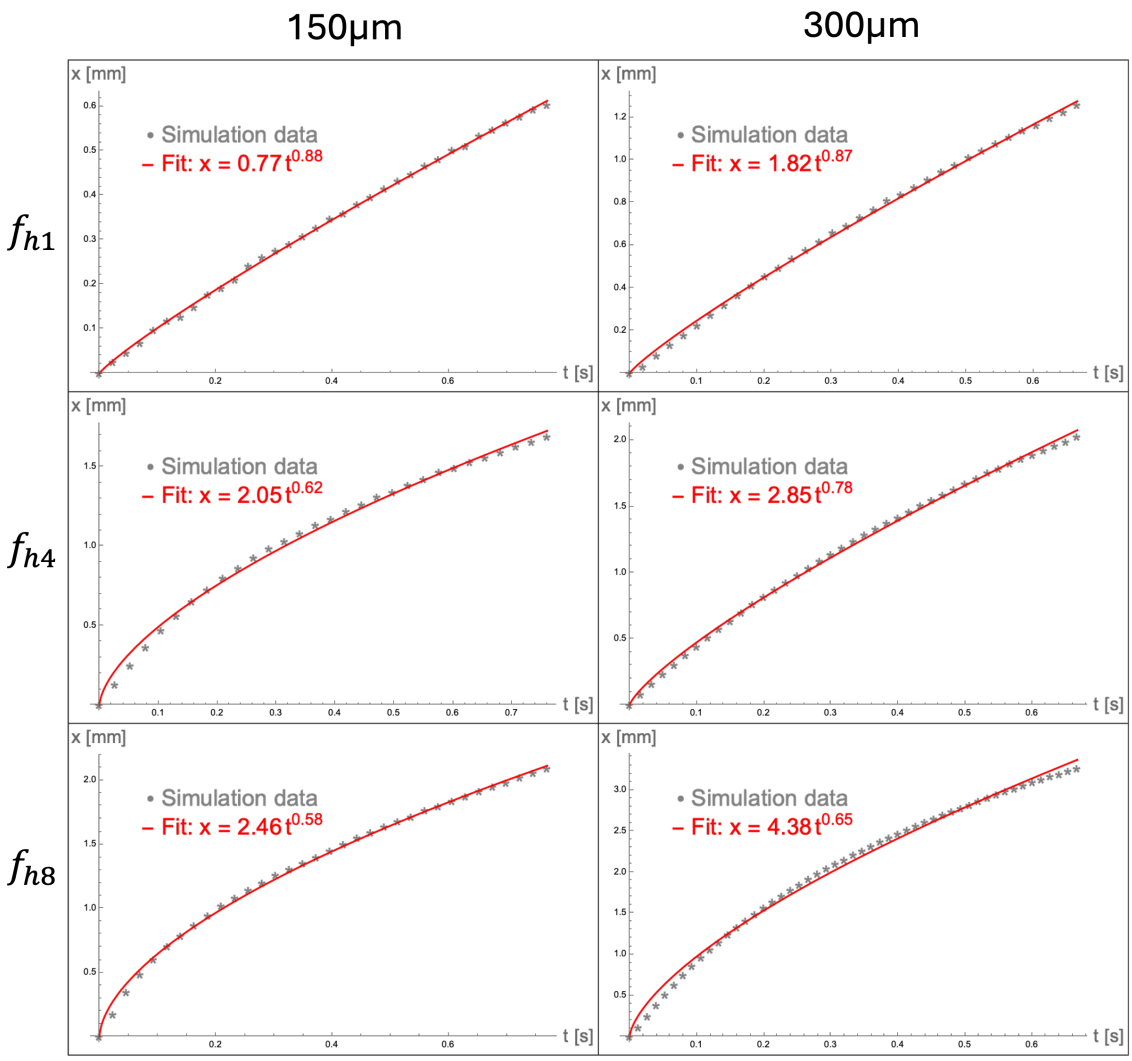

Figure 5.15: Empirical fits of fluid front evolution as a function of time under different pressures and channel heights. Left column: 150 μm height; Right column: 300 μm height. Rows correspond to increasing pressure (top to bottom).

This trend highlights the growing influence of viscous dissipation on the system dynamics. At low velocities, corresponding to low inlet pressures, viscous energy losses are minimal, allowing the fluid to advance more freely and linearly. In contrast, at higher velocities, the increased velocity gradients enhance viscous forces, resulting in greater energy dissipation. This shift in flow regime corresponds to a transition toward the behavior described by Washburn's law, where the front position follows a square-root dependence on time ($x \sim t^{0.5}$).

The comparison between microchannels of different heights further supports this interpretation. For the same applied pressure, the taller channels (300 μm) consistently exhibit higher fluid front positions and larger prefactor values A in the fitted equations, reflecting their lower hydraulic resistance relative to the 150 μm channels. However, the overall trend in the exponents n remains consistent between the two channel heights, confirming that the scaling behavior is predominantly governed by viscous effects rather than by geometric parameters alone.

The nonlinear behavior analysis demonstrates a clear transition toward the viscous regime predicted by Washburn's law as the driving pressure increases. The SPH simulations successfully capture the progressive influence of hydrodynamic resistance and validate the scaling relationship $x \sim t^{0.5}$ in microfluidic channels. These findings confirm that the numerical framework reliably reproduces the complex dynamics of viscous flow in confined geometries under different pressure conditions.

5.4 Conclusion

The presented numerical model successfully reproduces the fluid filling process in microchannels, demonstrating strong agreement with theoretical predictions. The SPH simulations confirm that modifying the pressure factor (f_h) results in corresponding changes in fluid velocity while maintaining a constant viscosity, as expected for Newtonian fluids. Additionally, the Washburn effect was observed in the simulations, a consequence of the negligible connecting tube in the model. This led to all energy dissipation occurring within the microchannel. These findings suggest that increasing the tube radius in experiments could help isolate energy dissipation effects within the channel itself.

The simulations also validated the SPH method for modeling different Newtonian fluids, including water, ethanol, and ethylene glycol. The results confirm that viscosity remains constant despite variations in pressure, reinforcing the assumption of Newtonian behavior under the studied conditions. This consistency highlights the robustness of the SPH approach for capturing microfluidic flow dynamics, particularly in pressure-driven systems where confinement effects and surface interactions play a crucial role.

Furthermore, the study reveals that microfluidic flows exhibit non-uniform velocity distributions along the channel, emphasizing the importance of considering local flow

variations when designing microfluidic systems. This observation is particularly relevant for applications requiring precise control over flow rates and shear conditions, such as lab-on-a-chip devices and biomedical diagnostics.

A key implication of this work is the demonstration that a single microchannel can simultaneously experience multiple shear rate and stress conditions. This opens new possibilities for microfluidic rheometry, allowing for in situ viscosity measurements without the need for complex channel geometries or additional experimental setups. By leveraging these variations, local viscosity can be determined within a uniform microchannel, providing valuable insights into fluid behavior under different shear conditions.

The analysis of the simulation results further indicates that the evolution of the fluid front is strongly influenced by inlet pressure, hydrodynamic resistance, and viscous dissipation. At low pressures, inertia dominates, leading to higher propagation exponents. However, as pressure increases, internal friction and hydrodynamic resistance intensify, stabilizing the flow and reducing the exponent to values near 0.5, characteristic of the Washburn regime. This transition confirms the theoretical expectations and provides a quantitative interpretation of how channel geometry and pressure impact filling dynamics—key aspects for optimizing microfluidic system design.

6 Microfluidic experiments

In this chapter, we employed a method based on an hydrostatics pressure driven flow [81] to validate the numerical results obtained in the previous chapter, incorporating an injection or suction pump to generate the pressure gradient required for fluid movement. Using image analysis, implemented through a Python-based algorithm, the fluid front propagation will be tracked to determine its velocity. This data will be used to construct stress versus shear rate curves, which will subsequently allow the calculation of the viscosity of the studied fluid. The collected experimental data will be compared with the simulations presented in Chapter 5.

Additionally, experiments will be conducted to minimize the effect of the connecting tube between the pressure generation source (reservoir or pump) and the microchannel. The goal is to reduce flow losses associated with the connector to observe nonlinear behavior, specifically the Washburn phenomenon. This approach will help evaluate the feasibility of conducting rheometry within the same microchannel without altering its geometry. For Newtonian fluids, viscosity should remain constant regardless of velocity variations (and consequently shear rate) along the channel. However, for non-Newtonian fluids, viscosity is expected to change as a function of these parameters. This study aims to validate this effect and assess the potential of performing in-channel rheometry for various fluid types.

6.1 Fabrication of the Microchannel

Microfluidic device fabrication requires precision and reproducibility to ensure accurate experimental results. The fabrication process employed in this study consists of several stages, including microchannel design, master mold fabrication via high-resolution 3D printing, PDMS molding, and final device assembly. The methodology adopted allows for the creation of reliable and high-fidelity microchannels suitable for fluid dynamics experiments.

6.1.1 Design of the Microchannel

The microchannels were designed using Autodesk Inventor, a professional-grade 3D CAD software that provides precise control over dimensions, structural details, and compatibility with additive manufacturing techniques. The design process prioritized geometrical accuracy to ensure compatibility with the resin-based 3D printing process,

optimizing both resolution and structural integrity of the microchannel walls. The dimensions were carefully chosen to balance fluidic behavior representation and manufacturability. Two distinct microchannel geometries were created, both with a width of $1\,mm$ and a length of $40\,mm$, but with different heights of $150\,\mu m$ and $300\,\mu m$, respectively (see Fig.6.1).

6.1.2 3D Printing of the Master Mold

The designed microchannels were fabricated using a *Prusa SL1S* resin-based 3D printer, which offers high-resolution printing capabilities ($50\,\mu m$) suitable for microfluidic applications. The photopolymer resin used in this process was specifically selected for its fine detail reproduction, low shrinkage, good mechanical stability after curing, and chemical resistance. These properties ensure dimensional accuracy, structural integrity, and compatibility with subsequent soft lithography steps. The resin polymerizes under a wavelength of 405 nm, ensuring that the microchannel features are well-defined and stable upon solidification.

After printing, the master molds underwent a post-processing step consisting of washing and UV curing. The printed parts were first washed in isopropyl alcohol to remove any uncured resin from the surface, using either ultrasonic agitation or a mechanical wash station. Subsequently, the parts were fully cured under UV light to complete polymerization and improve mechanical strength and thermal resistance.

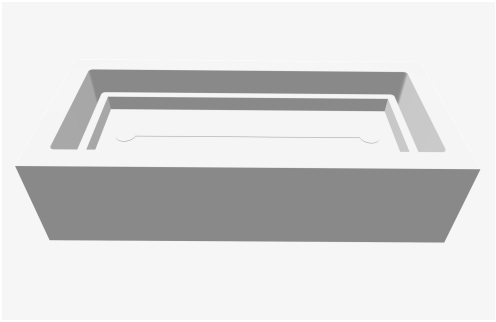

(a) $150\,\mu m$ height and $1\,mm$ width 3D-printed microchannel.

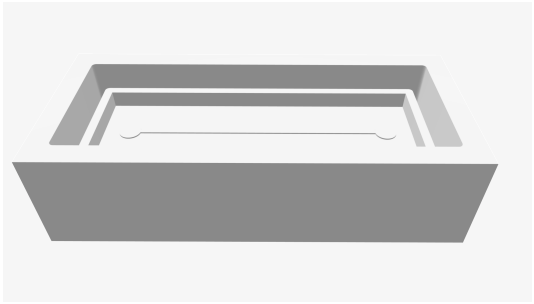

(b) $300\,\mu m$ height and $1\,mm$ width 3D-printed microchannel.

Figure 6.1: Microchannels designed in *Autodesk Inventor* and fabricated using a high-resolution resin-based 3D printer.

Post-processing of the printed master mold involved washing the structure thoroughly with detergent (Quix) to remove any residual uncured resin. The mold was then placed in an oven at $70°C$ for 3 hours to ensure complete evaporation of any remaining solvents used in the resin curing process. This step is essential to prevent unwanted chemical interactions between residual solvents and the reactants used in the subsequent PDMS molding process.

6.1.3 PDMS Molding

Once the resin master mold was fully prepared and post-cured, *Polydimethylsiloxane* (PDMS) was poured over its surface to create a negative mold of the microchannel geometry. PDMS is widely used in microfluidics due to its excellent optical transparency, biocompatibility, chemical resistance, and ease of fabrication [43].

The PDMS prepolymer mixture was prepared by combining the base elastomer with the curing agent in a 10:1 weight ratio. The mixture was thoroughly mixed to ensure uniform dispersion and then degassed in a vacuum chamber to eliminate air bubbles, which could otherwise create defects in the mold. This degassing step is critical for obtaining high-fidelity replicas of the microchannel geometry, as air bubbles could distort the fine microchannel features.

6.1.4 PDMS Curing

The degassed PDMS mixture was carefully poured over the resin master mold and placed in an oven for thermal curing. The curing process was carried out at $65°C$ for 2 hours, allowing for complete cross-linking of the polymer network. This step results in a robust yet flexible elastomeric structure that accurately preserves the fine details of the original 3D-printed master mold.

After curing, the PDMS layer was carefully peeled off from the resin master mold, ensuring that the microchannel features remained intact. The PDMS replica was then trimmed to remove excess material and improve its handling during the subsequent bonding step.

6.1.5 Demolding and Bonding

To create a functional microfluidic device, the demolded PDMS microchannel was permanently bonded to a glass substrate. This bonding process was achieved using a Corona Surface heater by Electro tech products, which enhances surface hydrophilicity and facilitates irreversible adhesion between PDMS and glass [125].

The bonding process consisted of exposing both the PDMS and glass surfaces to an oxygen plasma treatment for 20 seconds, followed by immediate contact between the treated surfaces. This process ensures a strong, durable bond while maintaining optical transparency, allowing for high-quality microscopy-based flow visualization.

The steps from 6.1.3 through 6.1.5 can be repeated using the same resin master mold, enabling the fabrication of multiple identical microchannels with high reproducibility.

The fabricated microfluidic devices were subsequently subjected to quality control tests, including microscopic inspection to verify channel integrity and dimensional accuracy. The final devices were then used in experimental setups for fluid dynamics analysis, ensuring that the microchannels met the required specifications for high-resolution flow experiments.

6.2 Experimental Set up

The experimental setup consists of a precision microfluidic pump (TTP Ventus) connected through a tube to a modified 2.5 ml Eppendorf tube with a hole drilled in the bottom. A microtube (Cole Parmer's Tygon) with inner and outer radii of $125\,\mu m$ and $250\,\mu m$, respectively, is inserted through this hole and connects the Eppendorf tube to the microchannel. The microchannel itself has a height of $150\,\mu m$ or $300\,\mu m$, depending on the experimental setup, with a width of $1mm$ and length of $4cm$.

The microchannel is placed under an inverted microscope (Optek BDS300 Series), which is equipped with a high-speed camera (AOS X-PRI). This camera captures images at frame rates ranging from 32 to 1000 frames per second, allowing for a detailed analysis of the fluid dynamics within the microchannel. The overall setup is illustrated in Fig. 6.2.

The inlet and outlet of the microchannel are placed as perpendicular orifices at opposite ends of the channel. The fluid is injected into the microchannel by a pressure-driven flow, which is regulated by varying the inlet pressure in the TTP-Ventus Pump control app software (Lee Company Software) at several different levels of injection of Pressure: $P_{in} = 300\,Pa, 400\,Pa, 500\,Pa$, and $700\,Pa$, following the methodology described in [81] adapted to injection with the pressure pump.

Fig. 6.3 presents a representative image of the fluid front propagation captured during the experimental phase using a high-speed camera. This visualization provides a detailed view of the fluid-air interface as it advances through the microchannel under controlled pressure-driven conditions. The experimental setup employs a $4\times$ optical magnification and an image resolution of 800×600 pixels, allowing precise observation of the flow dynamics and the evolution of the fluid front over time. This graphical representation is essential for understanding the channel-filling process and serves as a critical reference for validating the numerical simulation results.

6.3 Image Processing

The position x and velocity v of the fluid-air interface front are determined using an advanced image processing algorithm implemented in Python. The methodology involves a series of preprocessing and analytical steps to ensure accuracy and reproducibility in the extracted measurements.

First, a background subtraction technique is applied using the Mixture of Gaussians (MOG2) method, which effectively isolates the motion of the fluid front and enhances the dynamic region of interest by removing static elements from the image sequence (as we can see at the left side of the Fig. 6.4). This preprocessing step is crucial for improving the robustness of the contour detection process by reducing noise and eliminating non-moving artifacts.

Once the background is removed, the algorithm identifies the external contours in the processed images using OpenCV's `findContours` function; this function identifies

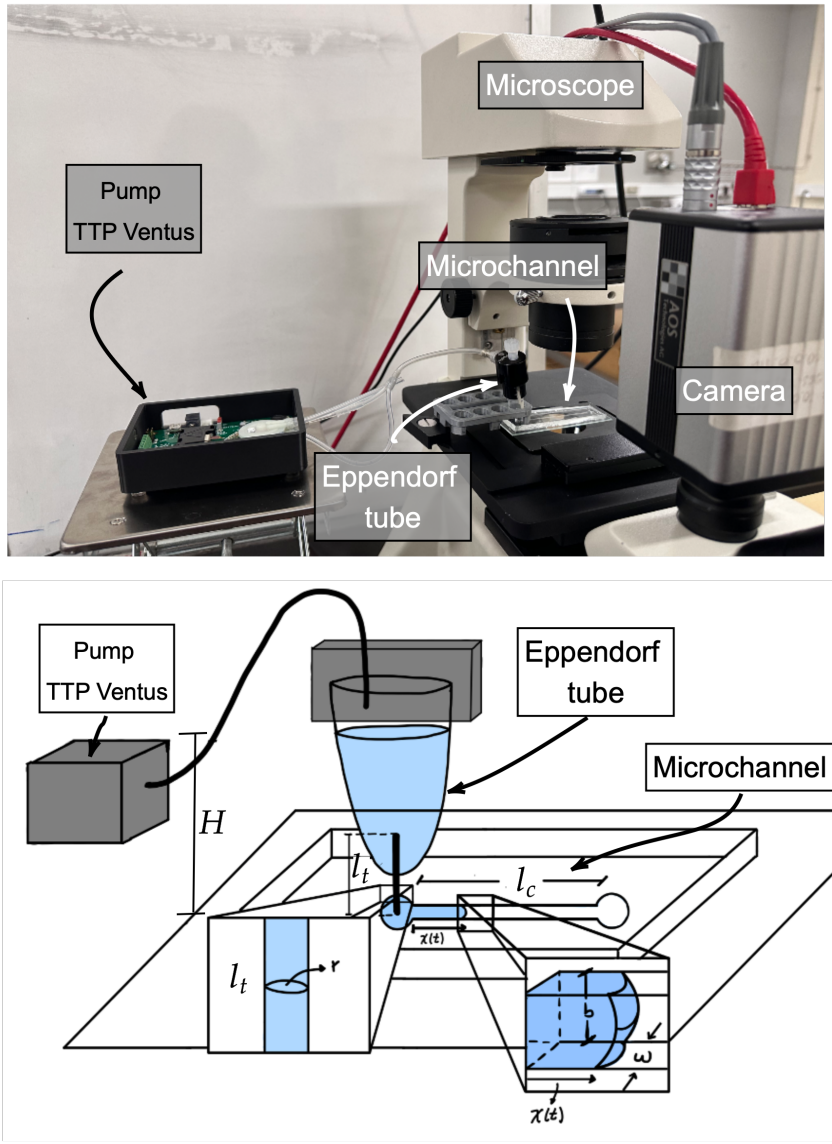

Figure 6.2: Schematic description of the exprimental setup, where H is the height from the microchannel to the top of the fluid column, r is the radius of the tube, l_t is the length of the tube, l_c is the length of the microchannel, b is the hiegth of the microchannel, w is the width of the microchannel and $x(t)$ is the position of the fluid-air interface as a function of time.

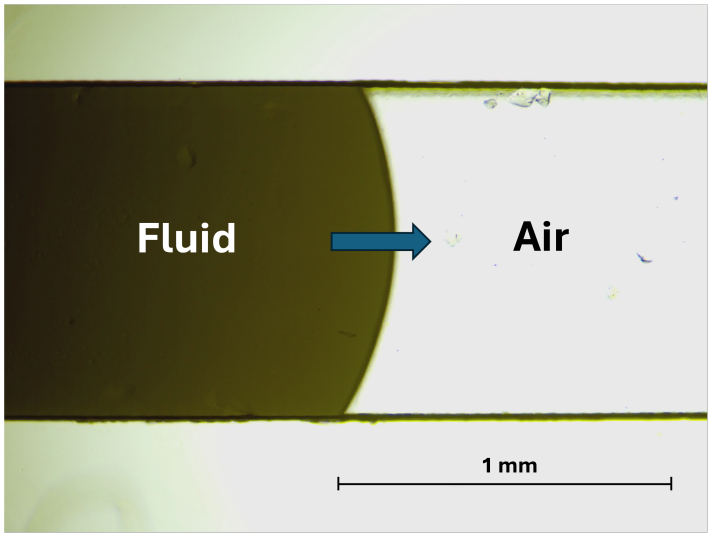

Figure 6.3: Representative image of the fluid front propagation captured during the experiment using a high-speed camera. The visualization, obtained with 4× optical magnification and an image resolution of 800×600 pixels, shows the fluid-air interface advancing through the microchannel.

all the contours in the image. Among all detected contours, the one with the largest area is selected, assuming it corresponds to the advancing fluid front (as shown on the right side of the Fig.6.4). This assumption is validated by ensuring consistency across consecutive frames.

To determine the front position, the maximum x-coordinate of the selected contour is extracted, representing the leading edge of the interface. The vertical coordinate y is estimated as the midpoint between the minimum and maximum values of the contour in the vertical direction. The displacement of the front is computed by converting pixel values to millimeters using a predefined scale factor calibrated from the experimental setup (approximately 200 pixels per millimeter). The velocity of the front is then calculated using the formula:

$$v = \frac{x_2 - x_1}{t_2 - t_1} \tag{6.1}$$

where x_1 and x_2 are the front positions at two consecutive time steps t_1 and t_2, respectively.

To ensure statistical reliability and reproducibility, the measurements are conducted across at least three independent video recordings for each experimental condition. These repetitions allow evaluating the variability of the measurements and improve the robustness of the results. For each time step, the mean and standard deviation of the front position and velocity are computed across all recorded videos, ensuring that the data capture intrinsic fluctuations while maintaining statistical consistency.

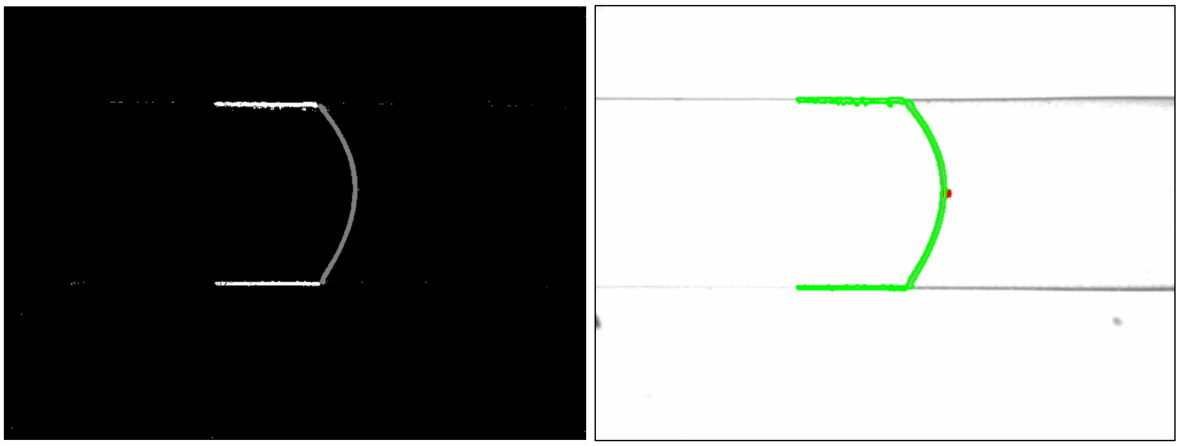

Figure 6.4: Image analysis of the fluid front. On the left the background subtraction is shown and on the right, the contour with the red analysis point is shown.

The final graphical representation of the results includes the averaged displacement and velocity of the fluid front over time, along with error bars representing the standard deviation at each measurement point. This approach ensures that the reported values are not only representative of a single experiment but are also statistically significant, accounting for experimental uncertainties and measurement noise.

6.4 Experiments results

6.4.1 Newtonian Results

6.4.1.1 Position vs Time

The relationship between the position of the fluid front and time was experimentally evaluated with water using two different microchannel heights: $150\,\mu m$ and $300\,\mu m$. The experiments were performed under three different applied pressures: $300Pa$, $400Pa$, and $500Pa$. The fluid used was water, and its front progression was recorded using a high-speed camera mounted on an inverted microscope. The front position was determined via advanced image processing that extracted the maximum x-coordinate of the fluid-air interface.

Each data point in Fig. 6.5 and 6.6 represents the position of the fluid front at a specific time, averaged over at least three independent measurements per condition. Error bars indicate the standard deviation, providing insight into experimental reproducibility and uncertainty. The experimental results are compared with the theoretical prediction derived from pressure-driven laminar flow, using the same equation applied in the simulation section (Eq. 2.37).

$$x(t) = \frac{b^3 w \left(1 - 0.63\,\frac{b}{w}\right)}{12} \left\{ \left[\left(\frac{8}{\pi} \frac{l}{r^4} + \frac{12}{b^3 w \left(1 - 0.63\,\frac{b}{w}\right)} x_0 \right)^2 + \frac{24}{b^3 w^2 \left(1 - 0.63\,\frac{b}{w}\right)} \frac{\Delta p}{\eta} (t - t_0) \right]^{1/2} - \frac{8}{\pi} \frac{l}{r^4} \right\}$$

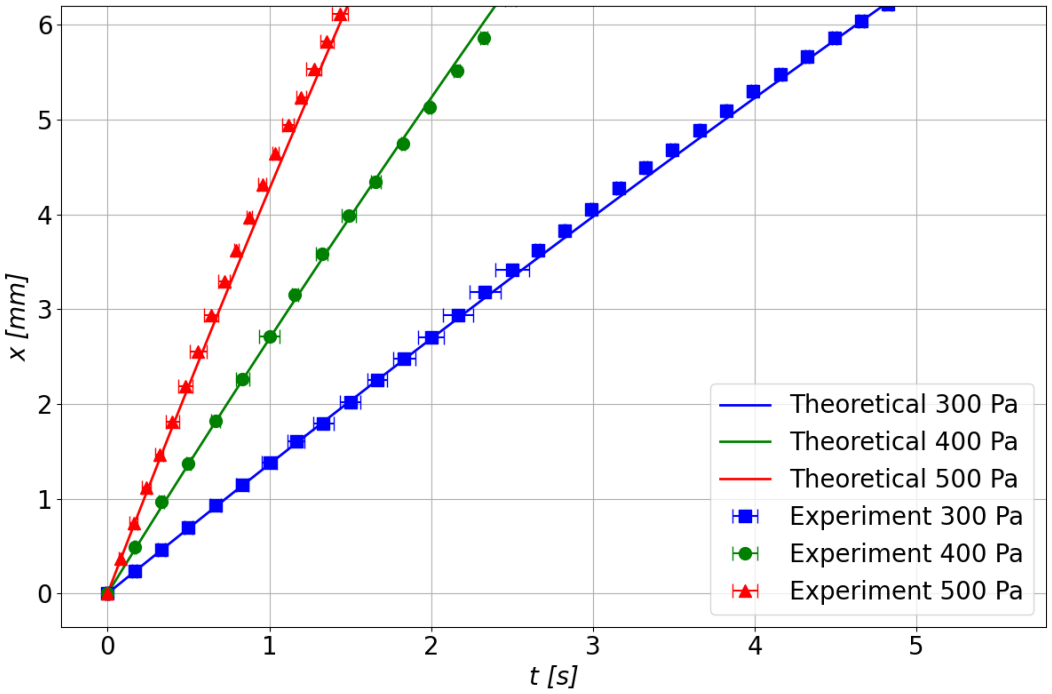

Figure 6.5: Experimental and theoretical front position over time for the 150 μm microchannel under 300, 400, and 500 Pa.

The Fig. 6.5 and 6.6 show that, for both microchannel heights, the front progresses faster at higher pressures. This is consistent with theoretical predictions: increasing the driving pressure reduces hydraulic resistance, resulting in faster fluid propagation. Notably, the 300 μm channel exhibits significantly higher front velocities than the 150 μm channel under equivalent pressure conditions. This difference reflects the lower hydraulic resistance associated with taller channels, which allows for enhanced volumetric flow and front advancement.

The hydraulic resistance values presented in Table 6.1 provide quantitative support for the trends observed in Fig. 6.5 and 6.6. For both microchannel heights, it is evident that the hydraulic resistance increases as the fluid advances, which aligns with the theoretical expectation that resistance is directly proportional to the front position x(t).

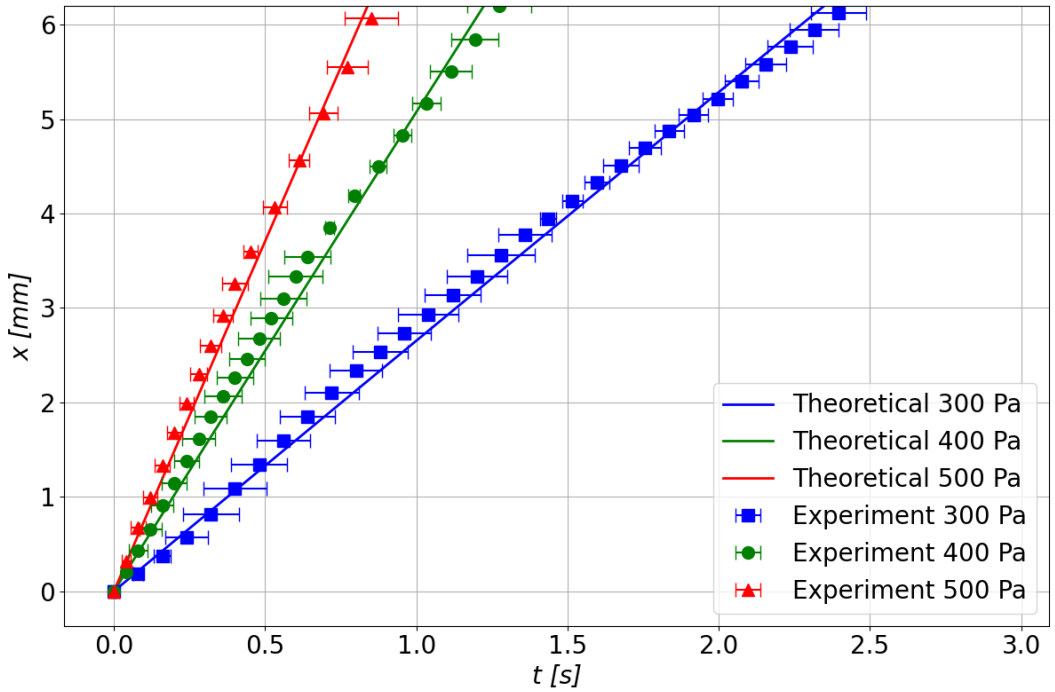

Figure 6.6: Experimental and theoretical front position over time for the 300 μm microchannel under 300, 400, and 500 Pa.

In the case of the 150 μm microchannel, the hydraulic resistance begins at $3.93 \times 10^9\,\mathrm{Pa\,s/m^3}$ when the front has traveled 1, mm, and increases substantially to $1.96 \times 10^{10}\,\mathrm{Pa\,s/m^3}$ at 5 mm. This significant rise in resistance illustrates the growing opposition to flow as the fluid traverses the channel length. Conversely, in the 300 μm microchannel, the resistance values remain much lower throughout the evaluated positions, starting at $5.48 \times 10^8\,\mathrm{Pa\,s/m^3}$ at 1 mm and reaching $2.74 \times 10^9\,\mathrm{Pa\,s/m^3}$ at 5 mm.

Table 6.1: Hydraulic Resistance in Microchannels

Microchannel Height (μm)	**Position x(t)** (mm)	**Resistance** ($Pa\,s/m^3$)
150	1.0	3.93×10^9
150	3.0	1.18×10^{10}
150	5.0	1.96×10^{10}
300	1.0	5.48×10^8
300	3.0	1.64×10^9
300	5.0	2.74×10^9

The comparative data in Table 6.1 highlight that, at equivalent positions, the hydraulic resistance in the 300 μm channel is significantly lower than that in the 150 μm

channel. This explains why, as shown in Fig. 6.5 and 6.6, the fluid front advances more rapidly in the taller channel. The lower hydraulic resistance in the $300\,\mu m$ configuration reduces the opposition to flow, facilitating faster fluid propagation under the same driving pressures.

The experimental data generally align well with the theoretical curves, validating the underlying model. Minor deviations between measured and predicted values can be attributed to experimental imperfections, such as non-uniform wetting, slight channel geometry variations, or minor flow disturbances. These small discrepancies highlight the complexity of replicating ideal conditions in real microfluidic environments, where surface tension and interactions with channel walls can subtly influence the flow dynamics.

The experimental data closely follow the theoretical predictions. To quantitatively assess the agreement, the Mean Squared Error (MSE) and the coefficient of determination (R^2) were calculated for each pressure condition. The results for the $150\,\mu m$ microchannel are in Table 6.2, while those for the $300\,\mu m$ microchannel are presented in Table 6.3.

Table 6.2: Error metrics for the $150\,\mu m$ microchannel.

Pressure (Pa)	**MSE (mm^2)**	**R^2**
300	0.0037	0.9991
400	0.0054	0.9985
500	0.0204	0.9947

For the $150\,\mu m$ channel, the MSE values ranged from $0.0037\,mm^2$ at $300Pa$ to $0.0204\,mm^2$ at $500Pa$, with corresponding R^2 values of 0.9991, 0.9985, and 0.9947. For the $300\,\mu m$ channel, the MSE ranged from $0.0220\,mm^2$ at $300Pa$ to $0.0297\,mm^2$ at $500Pa$, with R^2 values of 0.9950, 0.9905, and 0.9908.

Table 6.3: Error metrics for the $300\,\mu m$ microchannel.

Pressure (Pa)	**MSE (mm^2)**	**R^2**
300	0.0220	0.9950
400	0.0345	0.9905
500	0.0297	0.9908

These high R^2 values in both microchannel configurations confirm the strong predictive capacity of the theoretical model and validate its applicability in describing the fluid front dynamics during channel filling. The relatively low MSE values indicate minimal dispersion between experimental measurements and theoretical predictions.

It is observed that the MSE tends to increase at higher pressures, particularly in the $150\,\mu m$ channel. This may be attributed to minor experimental uncertainties such

as slight geometric variations, wetting inconsistencies, or image processing sensitivity at faster propagation velocities. In the $300\,\mu m$ channel, the MSE values are slightly higher overall, which could be explained by increased experimental variability at larger channel heights where the velocity profiles are less confined and subject to more local fluctuations.

In conclusion, this section confirms that the experimental system reproduces the expected pressure-position relationship for Newtonian flow in rectangular microchannels. The observed trends reinforce the role of both pressure magnitude and channel geometry in defining the fluid front dynamics. The experimental agreement with theoretical models supports the use of the current setup and methodology for further flow characterization and model validation.

6.4.1.2 Velocity vs Position

To investigate the internal flow dynamics within the microchannel, a segmented analysis of velocity as a function of position was performed. This approach was motivated by the observation that the fluid front did not advance at a uniform velocity, particularly at higher pressure conditions. The segmented velocity was determined over five sections of 1 mm each, corresponding to the first 6 mm of the microchannel length. The results for both the $150\,\mu$m and $300\,\mu$m channel heights are shown in Fig. 6.7 and 6.8.

The Fig. 6.7 and 6.8 represent the average velocity of the fluid front within a given segment, while the error bars reflect the standard deviation obtained from at least three repeated experiments. Three inlet pressures were tested: 300 Pa, 400 Pa, and 500 Pa. As expected, higher pressures yielded higher front velocities throughout the channel for both geometries.

The $300\,\mu$m channel showed a more significant velocity drop along its length compared to the $150\,\mu$m channel, due to the lower hydraulic resistance and higher initial velocities attained. This pattern indicates that energy dissipation becomes more pronounced as the fluid advances and interacts with the channel walls, particularly under higher-pressure conditions.

Additionally, the velocity profiles demonstrate a decreasing trend with increasing position. This is more evident for the highest inlet pressure (500 Pa), where the gradient is steeper. These observations are consistent with theoretical expectations, as the flow loses kinetic energy due to viscous dissipation and increasing hydrodynamic resistance with displacement.

This spatial variation in velocity provides strong evidence that the system is not in steady state, and that internal gradients in velocity are present along the flow path. Such conditions highlight the importance of local analysis when characterizing microfluidic flows, particularly in contexts where uniform shear or constant velocity assumptions may not hold.

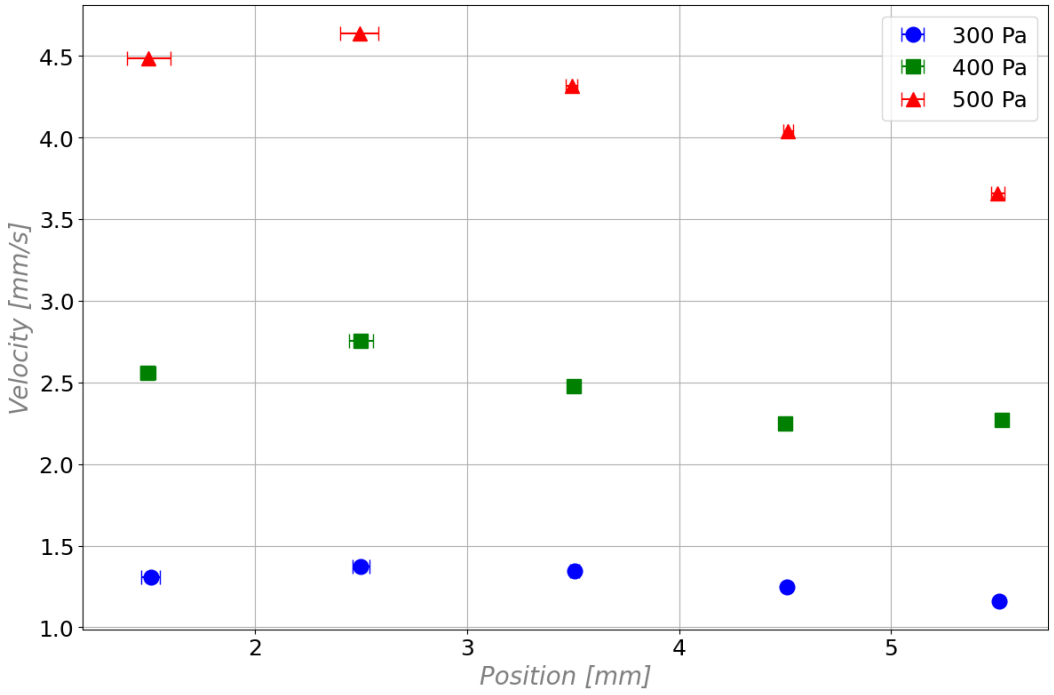

Figure 6.7: Segmented velocity vs position for 150 μm microchannel at three inlet pressures.

6.4.1.3 Shear Stress vs Shear Rate

To investigate the local rheological behavior of the fluid within the microchannel, an analysis of shear stress (τ) versus shear rate ($\dot{\gamma}$) was performed for both channel heights: 150 μm and 300 μm. The shear stress was computed using the following expression:

$$\tau = \frac{\Delta p}{\left[\frac{4}{3\pi}\left(\frac{Lb^2w}{r^4}\right) + \frac{2x(t)}{b\left(1-0.63\frac{b}{w}\right)}\right]}$$

where ΔP is the applied inlet pressure, L is the length of the inlet tubing, b and w are the microchannel height and width, respectively, r is the internal radius of the connecting tube, and $x(t)$ is the instantaneous penetration depth of the fluid front.

The local shear rate was estimated using the average velocity of the fluid front over each section, divided by the microchannel height, as described by:

$$\dot{\gamma} = 6\frac{||\vec{v}||}{b}$$

Measurements were conducted across the first 6 mm of the microchannel and divided into five sections. Within each section, local values of velocity and penetration depth were obtained through image processing, enabling calculation of both shear rate and

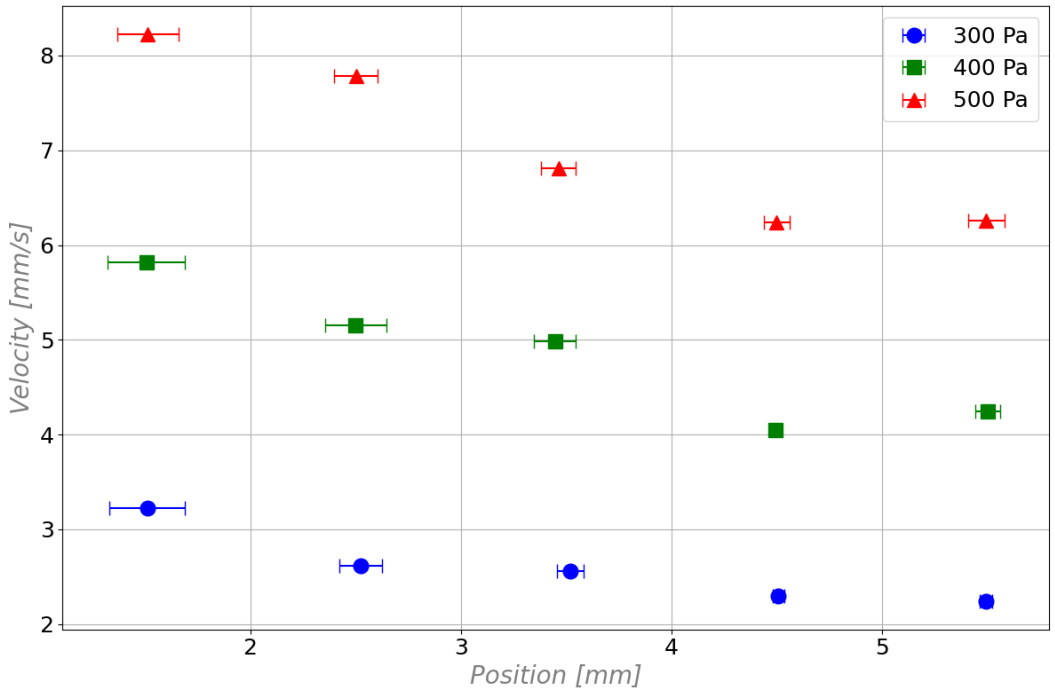

Figure 6.8: Segmented velocity vs position for 300 μm microchannel at three inlet pressures.

shear stress. Each data point on the graph represents a local value averaged within a 1 mm segment.

Fig. 6.9 and 6.10 display the resulting shear stress versus shear rate data for the 150 μm and 300 μm microchannels, respectively. Each color and marker type denotes a distinct inlet pressure condition: blue circles for 300 Pa, green squares for 400 Pa, and red triangles for 500 Pa.

Each data point on the graph corresponds to a specific measurement section along the microchannel. Importantly, the points with the highest shear rate values in each pressure group correspond to the measurements taken closest to the inlet, specifically at the 1 mm position. This is consistent with theoretical expectations, as shear rate tends to decrease along the length of the microchannel due to the reduction in fluid velocity as it progresses downstream.

The data reveal that within a single pressure condition, a range of shear stress and shear rate values is obtained along the channel length. This variation arises from the dependence of stress on the penetration depth $x(t)$, which increases over time, and the simultaneous decrease in velocity due to progressive energy dissipation from hydraulic resistance. Consequently, even at a fixed inlet pressure, the local flow conditions evolve, producing spatial variations in the rheological state of the fluid.

Notably, the 300 μm channel exhibits relatively stable stress values across different sections, a behavior attributable to its lower hydraulic resistance compared to the

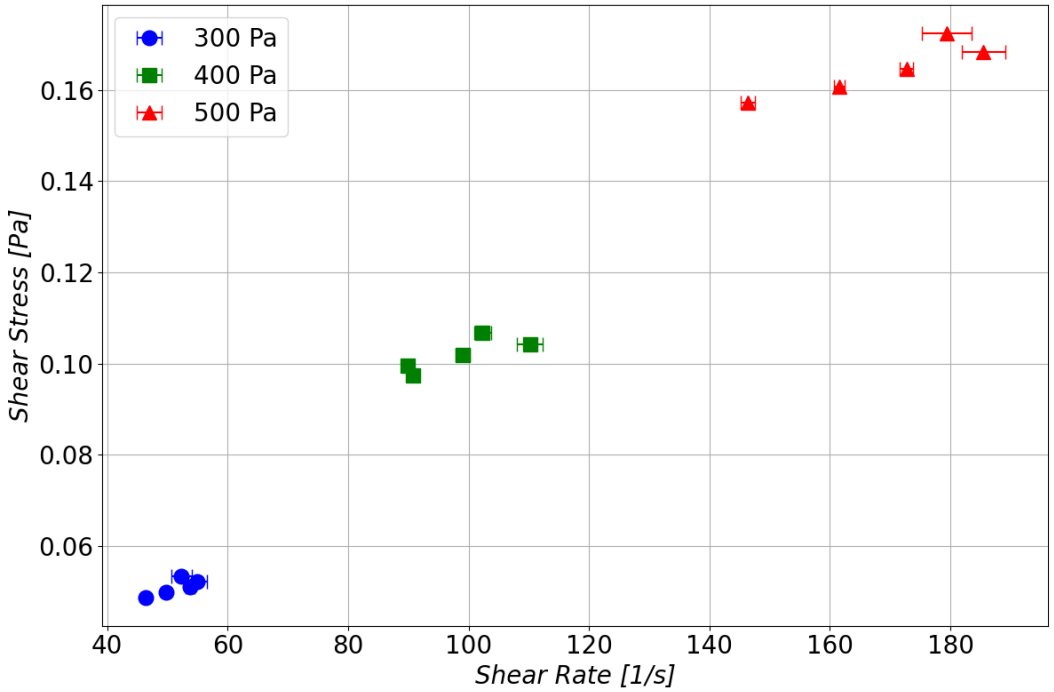

Figure 6.9: Experimental shear stress vs. shear rate in the 150 μm microchannel.

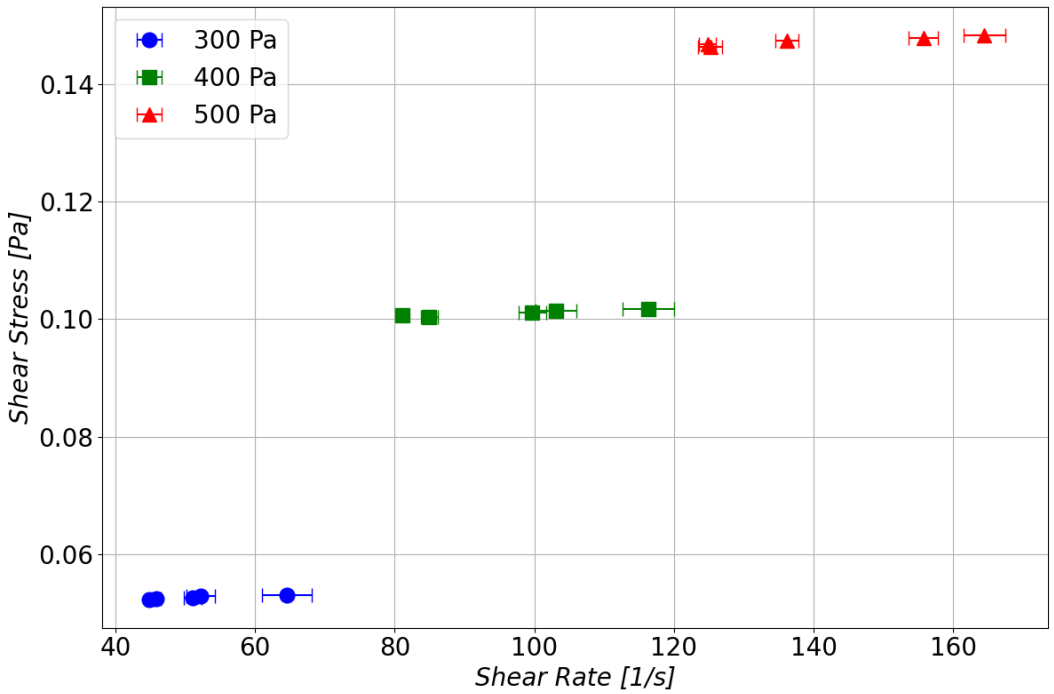

Figure 6.10: Experimental shear stress vs. shear rate in the 300 μm microchannel.

150 μm channel. The taller channel dissipates less energy over the same penetration depth, resulting in more uniform stress distributions. Conversely, the 150 μm channel shows a more marked decrease in shear rate, indicating greater energy loss and stronger interaction with channel walls.

This analysis underscores the fact that pressure-driven flow in microchannels does not produce uniform shear conditions along the flow path. The observed spread of τ and $\dot{\gamma}$ values within each pressure setting suggests that microfluidic systems inherently support multiple shear environments simultaneously, even without altering the geometry or inlet conditions. These findings support the potential use of simple straight channels for microfluidic rheometry under well-controlled experimental conditions.

6.4.1.4 Viscosity

To evaluate the rheological behavior of the fluid under experimental conditions, the dynamic viscosity was calculated as a function of the axial position along the microchannel. This was done for both channel heights (150 μm and 300 μm) and for three different inlet pressures (300 Pa, 400 Pa, or 500 Pa). The viscosity η at each position x was computed using the following expression:

$$\eta = \frac{\Delta P}{\left(\dot{x(t)}\right)\left[\frac{8}{\pi}\left(\frac{Lb^2w}{r^4}\right) + \frac{12x(t)}{b^2\left(1-0.63\frac{b}{w}\right)}\right]}$$

Here, ΔP is the inlet pressure (300 Pa, 400 Pa, or 500 Pa), $\dot{\gamma}(x)$ is the local shear rate estimated from the fluid velocity in each segment using Eq. 2.23, and x is the distance traveled by the fluid front. The term in brackets accounts for both the hydraulic resistance of the connecting tube and the variable resistance in the microchannel as the fluid advances. Each data point represents the average viscosity over a 1 mm section of the microchannel, and the error bars indicate the standard deviation computed from a minimum of three experimental replicates.

The results shown in Fig. 6.11 and 6.12 confirm the Newtonian behavior of water under all tested conditions. Despite variations in shear stress and shear rate across the channel, the viscosity remains consistent along the flow path. The average viscosity values for the 150 μm channel are $\eta = 1.00 \pm 0.04\,mPa\,s$, $1.05 \pm 0.06\,mPa\,s$, and $0.99 \pm 0.06\,mPa\,s$ for 300 Pa, 400 Pa, and 500 Pa respectively. For the 300 μm channel, the values are slightly higher and show more variation: $\eta = 1.04 \pm 0.12\,mPa\,s$, $1.06 \pm 0.14\,mPa\,s$, and $1.06 \pm 0.11\,mPa\,s$.

The mean viscosity across all conditions and positions is approximately $1.01 \pm 0.05\,mPa\,s$ for the 150 μm channel and $1.05 \pm 0.12\,mPa\,s$ for the 300 μm channel, values that are in excellent agreement with the theoretical viscosity of pure water at 20°C (approximately $1.00\,mPa\,s$).

This consistency validates the assumption that the fluid behaves as a Newtonian liquid under the studied conditions, further reinforcing the accuracy of the experimental

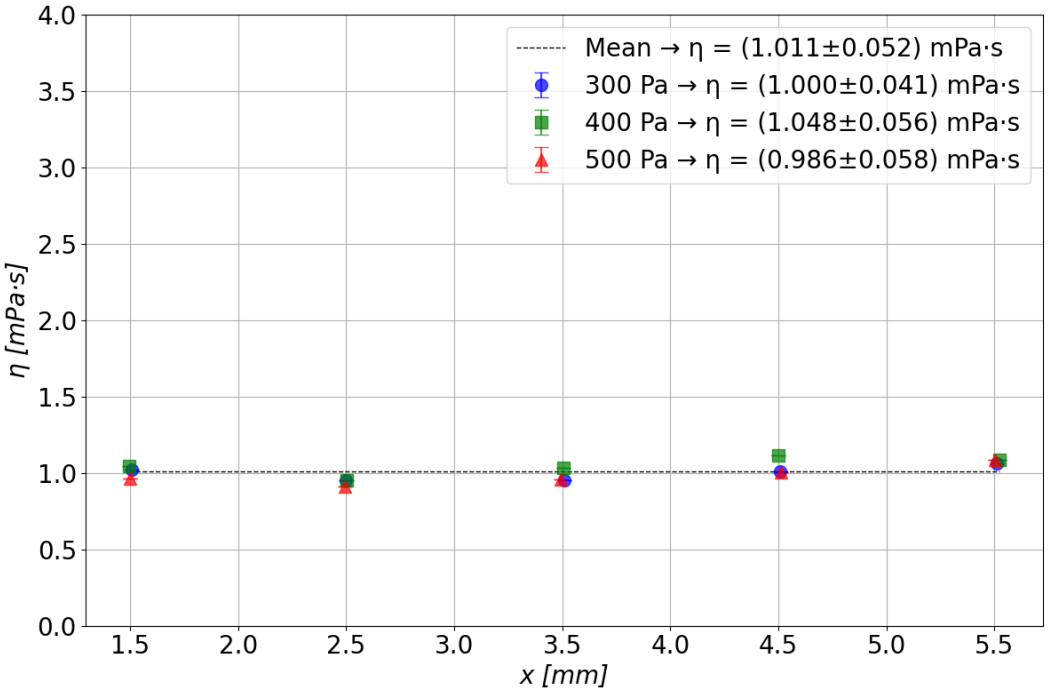

Figure 6.11: Experimental viscosity along the 150, μm microchannel.

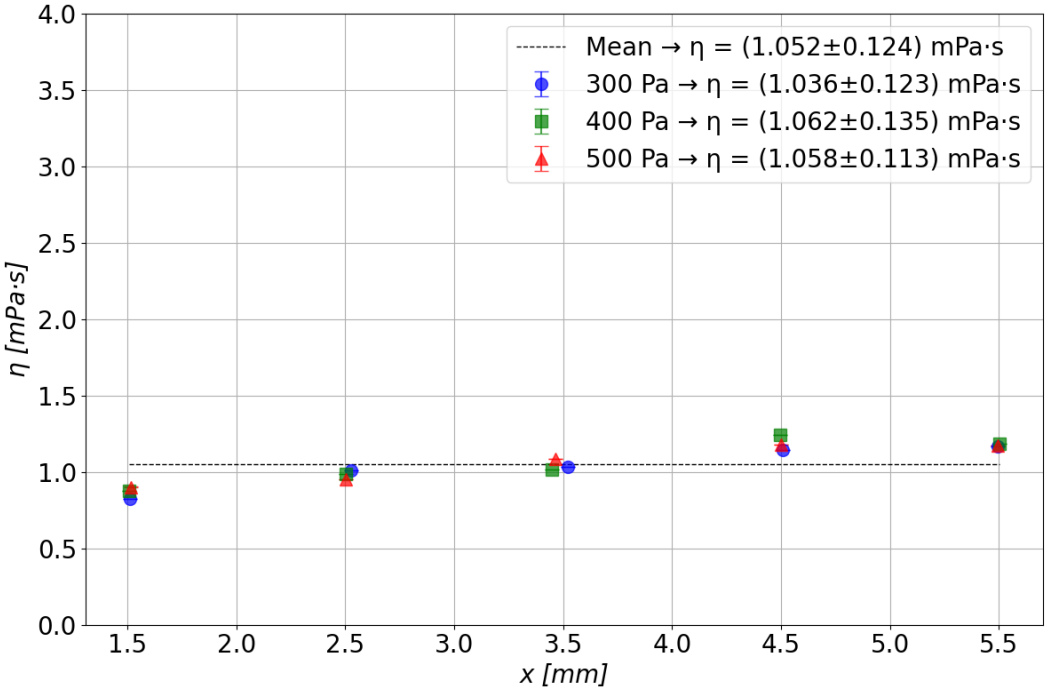

Figure 6.12: Experimental viscosity along the 300, μm microchannel.

methodology and image processing techniques used. The minor variations observed can be attributed to measurement uncertainties, but they do not indicate any significant deviation from the expected behavior.

Additionally, this analysis supports the feasibility of using microchannels for rheological measurements, as it demonstrates that key fluid properties, such as viscosity, can be reliably extracted from microfluidic experiments. The ability to maintain constant viscosity while observing variations in shear rate is a crucial confirmation that the flow dynamics are well-characterized and that the system operates within the expected theoretical framework.

6.4.2 Non Newtonian Results

The study of blood rheology is essential for understanding hemodynamic phenomena under physiological and pathological conditions. However, the complexity of human blood, which exhibits non-Newtonian behavior due to the presence of red blood cells, makes direct experimental and computational modeling challenging. To overcome these difficulties, various synthetic fluids have been proposed as *blood analogs* to replicate the viscoelastic properties and shear-thinning behavior of blood. The works of Brookshier et al. 1993 [126] and Mann et al. 1990 [127] have demonstrated that an aqueous solution of xanthan gum and glycerin serves as an excellent blood analog fluid. Xanthan gum, a polysaccharide with viscoelastic properties, provides shear-thinning behavior similar to blood, where viscosity decreases with increasing shear rate. Glycerin, on the other hand, allows for density adjustment, closely matching that of human blood (approximately $1050\,\mathrm{kg/m^3}$), ensuring accurate inertial effects in hemodynamic studies.

Brookshier and Tarbell [126] investigated xanthan gum and glycerin solutions over a shear rate range of 1 s^{-1} to 1000 s^{-1} and demonstrated that these solutions closely mimic the complex viscosity of blood at 2 s^{-1}. Additionally, their optical transparency makes them well-suited for experimental techniques such as Particle Image Velocimetry (PIV). Similarly, Mann and Tarbell [127] used non-Newtonian blood analogs in rigid artery models, highlighting that incorporating viscoelastic components provides a more accurate representation of blood flow dynamics in large arteries and bifurcations.

Since blood is a non-Newtonian fluid whose behavior varies with hematocrit and shear rate, it is essential to use analogs that mimic these properties. The combination of xanthan gum and glycerin in aqueous solution has been experimentally validated as a reliable substitute, commonly used in fluid mechanics research involving artificial vascular systems. Its ease of preparation, stability, and similarity to blood rheological properties make it an optimal choice for in vitro hemodynamic studies.

6.4.2.1 Position vs Time

The propagation of a blood-analog fluid composed of 0.03 % xanthan gum and 30 % glycerin was experimentally analyzed in a microchannel with a height of $300\,\mu m$ and

a width of $1\,mm$. The position of the fluid front was measured at each time step for three inlet pressures: $300\,Pa$, $500\,Pa$, and $700\,Pa$. Each point corresponds to the instantaneous location of the fluid front until a total displacement of approximately $16\,mm$ was reached.

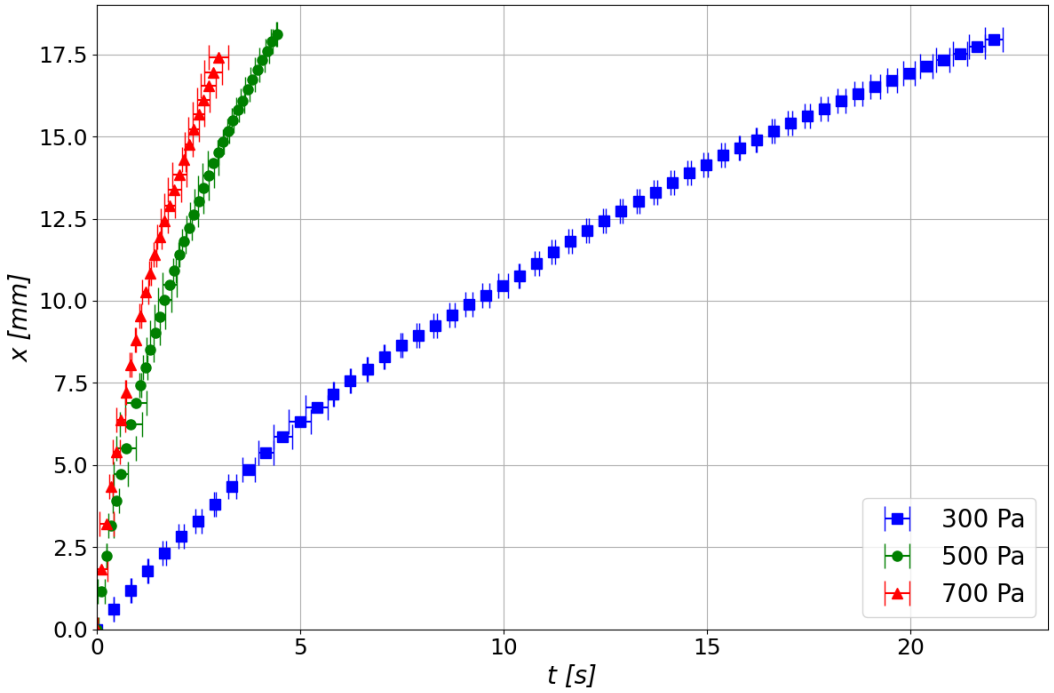

Figure 6.13: Experimental results showing the non-linear advancement of the xanthan gum and glycerin solution in a $300\,\mu m$ high microchannel

Fig. 6.13 presents the position of the fluid front as a function of time under the three pressure conditions. Asterisks represent measurements at $300\,Pa$, blue circles at $500\,Pa$, and yellow plus signs at $700\,Pa$.

While the xanthan solution is non-Newtonian by nature, the nonlinear propagation observed here is not attributed solely to its rheological complexity. Instead, the non-linearity arises predominantly from progressive energy dissipation due to increasing hydrodynamic resistance as the fluid advances.

As the fluid front moves forward, the effective flow resistance increases—both from the cumulative length of fluid in the channel and the greater surface area in contact with the walls. This additional resistance causes a loss in kinetic energy, reducing the local velocity.

Because the xanthan solution is a shear-thinning fluid, its viscosity is not constant but decreases with increasing shear rate. At the beginning of the experiment, the fluid is driven at higher speeds, generating larger shear rates and, consequently, lower effective viscosity. However, as energy is lost and shear rate decreases, the viscosity

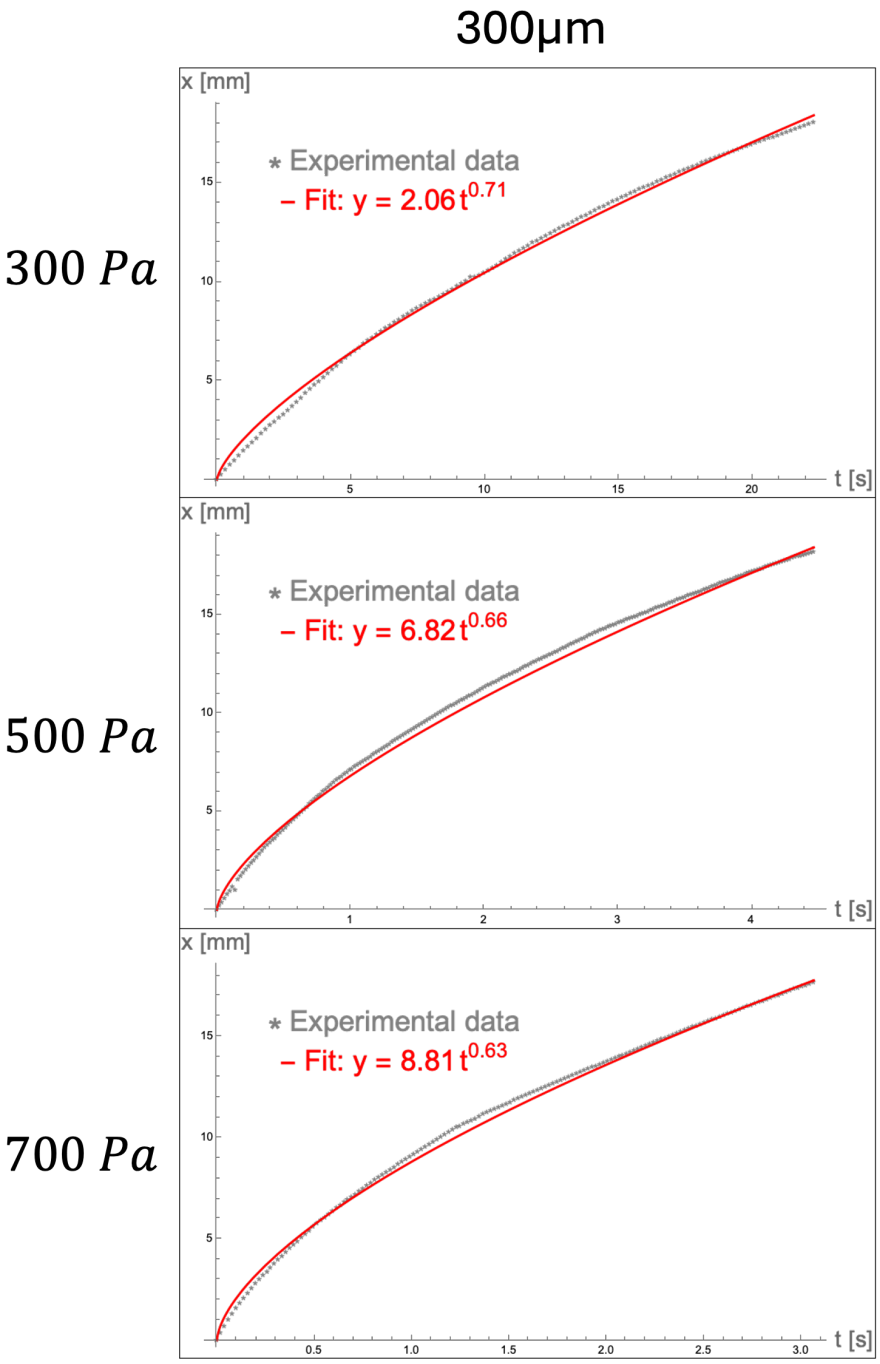

Figure 6.14: Experimental progression of the xanthan gum and glycerin solution under varying inlet pressures. The observed decrease in the power-law exponent suggests a transition toward the Washburn regime at higher pressures.

increases again, further amplifying the resistance to flow and slowing down the fluid advance.

This feedback mechanism (where kinetic energy loss leads to a reduced shear rate and increased viscosity) explains the observed sublinear propagation trend, even without invoking complex viscoelastic effects.

Fig. 6.14 presents the same datasets fitted using a power-law model, each curve was fitted using a power-law expression of the form:

$$x(t) = At^m, \tag{6.2}$$

where m is the propagation exponent and A is a fitting parameter related to the fluid and channel characteristics. Our experimental results confirm that the fitted exponents m decrease with increasing pressure: from 0.534 at $300\,Pa$, to 0.408 at $500\,Pa$, and 0.367 at $700\,Pa$. This trend suggests a transition toward a Washburn-like regime, where flow becomes increasingly governed by viscous dissipation. Initially, the xanthan-gum-based solution experiences lower resistance due to shear-thinning effects, which reduce its viscosity at higher shear rates. As the front advances and velocity gradients decrease, the flow stabilizes and becomes more resistive, leading to a slower propagation rate.

The experimental findings confirm that the xanthan–glycerin solution exhibits a nonlinear propagation behavior, accurately described by a power-law model in which the exponent decreases with increasing inlet pressure. This trend highlights the dominant role of viscous energy dissipation and shear-thinning effects in confined microchannel flows. As the fluid advances, rising hydrodynamic resistance leads to kinetic energy loss, reducing the local shear rate and increasing the apparent viscosity—thereby limiting further acceleration. The coupled evolution of viscosity and velocity supports the interpretation that the observed behavior is governed by the fluid's rheological response to flow conditions, rather than solely by its non-Newtonian nature.

Nonetheless, additional experiments are needed to confirm this interpretation. In particular, control tests using a 30% glycerin solution without xanthan gum should be performed to isolate the effect of shear-thinning behavior from pure viscous dissipation. Such comparisons would help clarify whether the observed nonlinearity stems from pressure-dependent viscosity changes or solely from hydrodynamic resistance in the microchannel.

6.4.2.2 Velocity vs Position

In this section, the local velocity of a xanthan gum and glycerin (30%) solution was measured along the microchannel at different positions. The measurements were carried out under three pressure conditions ($300\,Pa$, $500\,Pa$, and $700\,Pa$) in a $300\,\mu m$-high channel. The velocity at each point corresponds to the mean value within a $1\,mm$ segment, and error bars represent the standard deviation obtained from at least three experimental repetitions.

Fig. 6.15 displays the velocity of the fluid as a function of position for each applied pressure. Circles represent data for 500 Pa, crosses for 300 Pa, and plus signs for 700 Pa. Each curve shows the spatial evolution of the front velocity as the fluid propagates through the channel.

The results reveal a distinct non-linear evolution of velocity along the microchannel. For all pressures, the velocity decreases as the front advances, indicating increasing resistance over distance. This behavior suggests a loss of kinetic energy as the fluid progresses, which can be attributed to the cumulative hydrodynamic resistance in the channel.

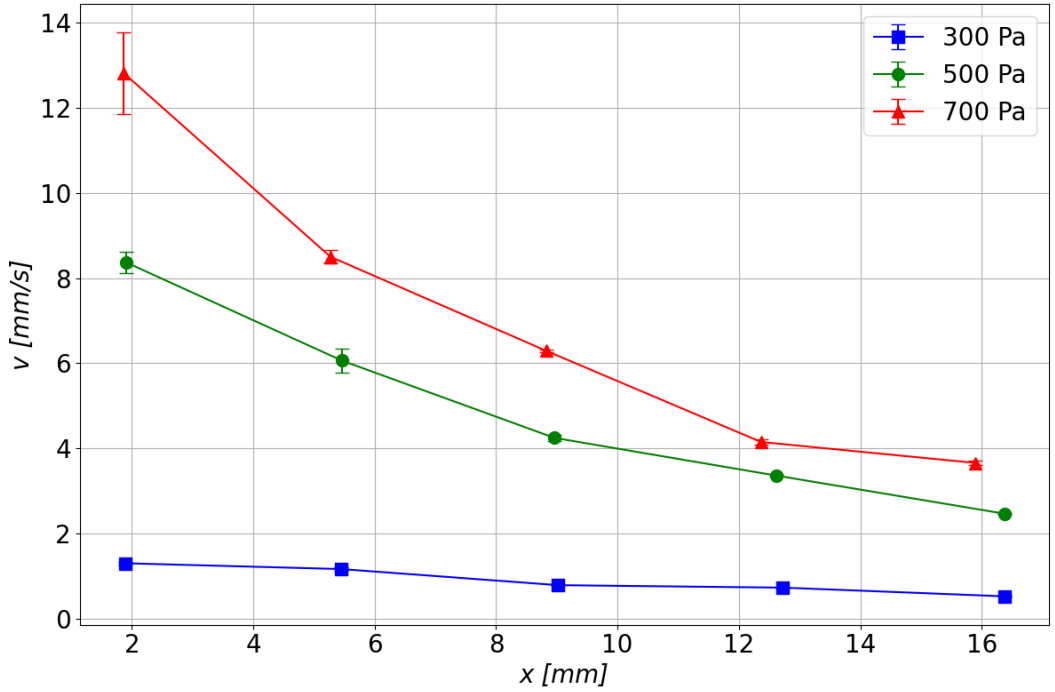

Figure 6.15: Velocity evolution as a function of position for a xanthan gum and glycerin solution in a 300-μm high microchannel. The initial slope of the velocity profile increases with higher pressure, but gradually diminishes over time, indicating the influence of non-Newtonian shear-thinning effects.

Importantly, while the xanthan-glycerin solution is a known shear-thinning fluid, the reduction in velocity is not solely due to its non-Newtonian nature. Instead, it reflects the energy dissipation caused by increased resistance. As the fluid slows down, the local shear rate decreases, and for a shear-thinning fluid, this leads to an increase in apparent viscosity further enhancing resistance in a feedback loop. Therefore, the velocity gradient flattening along the channel can be interpreted as the result of a progressive loss of kinetic energy rather than a viscoelastic effect.

The spatial variation in velocity supports the hypothesis that the nonlinear flow behavior of the xanthan-glycerin solution is primarily driven by energy dissipation and

resistance buildup rather than intrinsic non-Newtonian effects alone. The self-regulated decrease in velocity is tightly coupled with the evolving shear rate and viscosity, reinforcing the importance of flow resistance in microfluidic propagation dynamics.

6.4.2.3 Shear Stress vs Shear Rate

The local shear stress and shear rate were experimentally determined for a xanthan gum (0.03%) and glycerin (30%) solution flowing through a $300\,\mu m$ high microchannel under three applied pressures: $300\,Pa$, $500\,Pa$, and $700\,Pa$. Each point in the plot represents an averaged measurement over the same segment of the channel used in the previous section, and error bars indicate the standard deviation from at least three experimental repetitions.

The local shear stress (τ) at each measurement point was calculated using the following equation:

$$\tau = \frac{\Delta P}{\left[\frac{4}{3\pi}\left(\frac{Lb^2w}{r^4}\right) + \frac{2x(t)}{b\left(1-0.63\frac{b}{w}\right)}\right]}$$

This expression considers both the hydraulic resistance of the inlet tubing and the microchannel segment traversed by the fluid at each time step. The pressure drop (ΔP) applied at the inlet is balanced by the total system resistance, which includes the fixed resistance of the tubing and the dynamic resistance of the microchannel that varies with the fluid front position $x(t)$. This methodology allows the calculation of local stress as the fluid progressively fills the channel.

The shear rate ($\dot{\gamma}_w$) at the channel wall was estimated using a corrected form derived from the power-law model for non-Newtonian fluids:

$$\dot{\gamma}_w = \frac{1}{3}\dot{\gamma}_a\left[\frac{2n+1}{3n}\right]$$

Here, $\dot{\gamma}_a$ represents the apparent shear rate, calculated as six times the average velocity divided by the channel height. Since the apparent shear rate does not directly account for the velocity profile flattening observed in shear-thinning fluids, a correction factor based on the flow behavior index (n) is applied to approximate the true wall shear rate. In this study, a commonly accepted value of $n = 0.8$ [128, 129], frequently used for blood analog fluids, was adopted for the correction.

Fig. 6.16 shows the experimental relationship between shear stress and shear rate for the three pressure conditions. The data are fitted with a power-law function of the form $\tau = k\dot{\gamma}^n$, where the exponent n reflects the degree of nonlinearity in the fluid's response. The fit yielded decreasing values of n with increasing pressure: $n = 0.534$ ($300\,Pa$), $n = 0.408$ ($500\,Pa$), and $n = 0.367$ ($700\,Pa$), confirming the shear-thinning nature of the fluid.

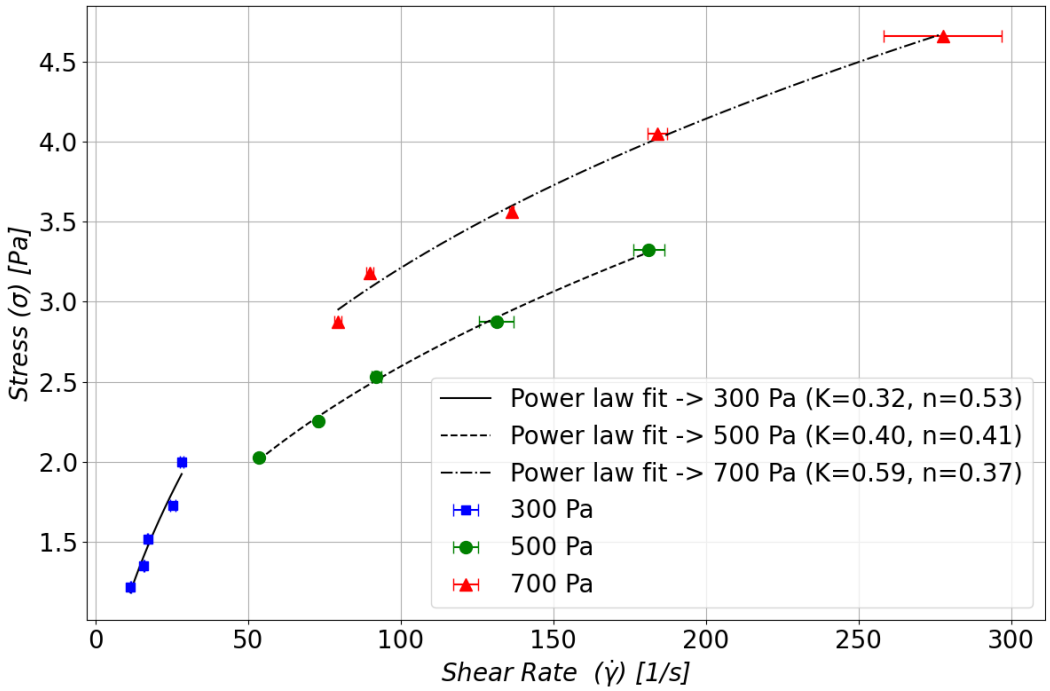

Figure 6.16: Shear stress as a function of shear rate for a xanthan gum and glycerin solution in a 300 μm high microchannel.

The decreasing values of n with pressure suggest that the shear-thinning behavior of the xanthan–glycerin solution becomes more pronounced at higher pressures. This is likely due to enhanced alignment of the polymer chains in the direction of flow, facilitated by stronger shear fields. The fluid, initially more resistant to deformation at low pressures, becomes progressively less viscous as it flows under higher stress, characteristic of shear-thinning fluids.

However, this behavior is not solely a material property; it is strongly coupled to the spatial dynamics of the system. As the fluid front advances through the microchannel, local stress naturally decreases due to increasing hydrodynamic resistance, which scales with distance. According to the relation $\tau \propto 1/x_f$, where x_f is the position of the fluid front, the reduction in stress leads to a corresponding decrease in shear rate. This dynamic evolution reinforces the observed nonlinear trend without requiring viscoelastic effects.

The result is a feedback mechanism: energy dissipation through hydrodynamic resistance causes a drop in stress and shear rate, which in turn alters the local viscosity of the shear-thinning solution. The effective rheological response is therefore not only a function of the fluid's material properties but also of the propagation mechanics within the confined geometry.

The experimental stress–shear rate data confirm that the xanthan–glycerin solution exhibits pronounced shear-thinning behavior, with the flow exponent n decreasing

as pressure increases. This indicates a stronger deviation from Newtonian behavior at higher pressures. Moreover, the results reveal that spatially evolving flow conditions—particularly stress reduction along the advancing front—play a key role in shaping the apparent rheological response of the fluid. The measured nonlinearity is not only a property of the fluid but also a consequence of its propagation through a resistance-dominated microchannel system.

6.5 Conclusion

The experimental results successfully illustrate the fundamental principles of pressure-driven flow in microchannels and validate the theoretical model describing fluid front dynamics.The comparison between experimental data and theoretical predictions shows strong agreement, reinforcing the reliability of the theoretical model. However, minor deviations were observed, likely due to wetting effects, geometric imperfections, or experimental uncertainties. These discrepancies highlight the complexity of real microfluidic systems, where interactions between the fluid and channel walls can introduce slight modifications to the expected behavior.

The findings confirm that the velocity of the advancing fluid front increases with the applied pressure, as expected from classical fluid dynamics. Additionally, the results demonstrate that the $300\,\mu m$ microchannel exhibits higher velocities than the $150\,\mu m$ microchannel under the same pressure conditions, which is attributed to the lower hydraulic resistance in the larger channel.

The velocity analysis as a function of pressure confirmed the Newtonian behavior of water within the studied microchannels. The nearly perfect linearity between pressure and velocity supports the theoretical assumption that water's viscosity remains constant regardless of the driving pressure. Furthermore, segmenting the analysis into 1 mm sections revealed variations in velocity along the microchannel, particularly at higher pressures. This suggests that energy dissipation effects become more pronounced as pressure increases, leading to greater velocity differences along the channel.

The stress versus shear rate analysis further confirmed variations in local shear conditions within the channel. Different shear rates were observed at the same inlet pressure, indicating that the flow profile is not entirely uniform along the microchannel length. However, the stress variations align well with the expected Newtonian behavior, where stress is directly proportional to the shear rate which is consistent with the microfluidic simulations .

To verify that viscosity remained constant despite variations in shear rate, an experimental viscosity analysis was performed along the microchannel. The results demonstrated that viscosity remained stable across the studied sections, confirming that water behaves as a Newtonian fluid under these conditions. Any minor fluctuations in viscosity can be attributed to experimental uncertainties or slight variations in local flow conditions.

The experiments conducted with a xanthan gum and glycerin solution demonstrate the nonlinear dynamics of shear-thinning fluids in confined microfluidic geometries. The observed position–time behavior follows a power-law relationship, where the propagation exponent decreases with increasing pressure, indicating a transition toward the Washburn regime. This trend is consistent with the interplay between increasing hydrodynamic resistance and the shear-dependent viscosity of the fluid. Rather than being purely a consequence of the fluid's non-Newtonian nature, the nonlinear propagation is strongly influenced by progressive energy dissipation along the microchannel, which reduces the local shear rate and increases the apparent viscosity.

Importantly, the experimental results validate the potential of microchannels to serve as in-situ rheometers, enabling localized, simultaneous measurements of shear stress and shear rate under well-controlled flow conditions. This capability offers a powerful approach for characterizing the rheological behavior of non-Newtonian fluids without requiring complex setups. The findings contribute to the understanding of pressure-driven microfluidic transport and provide a foundation for the development of diagnostic and analytical tools in biomedical and soft matter research.

However, to fully confirm the interpretations proposed in the blood analogue section, further experimental validation is necessary. Future work should include control experiments with Newtonian fluids of similar viscosity, such as glycerin-only solutions, and expanded measurements across a wider range of pressures and concentrations. These additional tests will help isolate the effects of shear-thinning behavior from those of energy dissipation and channel geometry, strengthening the conclusions and broadening the applicability of this microfluidic rheometric approach.

7 Conclusions

This thesis presents the development and validation of a SPH framework adapted for microfluidic applications, integrating an Inter-Particle Force (IPF) model for surface tension. The proposed approach, based on the Wang potential [23], establishes a physically consistent methodology for modeling cohesive interactions among fluid particles, ensuring accurate representation of interfacial phenomena. By using the Lagrangian nature of SPH, the model accounts exclusively for internal interactions within the liquid phase, eliminating the need to explicitly simulate the surrounding gas. This refinement over traditional methods allows for a more direct connection between surface tension effects and energy minimization, providing a robust computational scheme for studying confined microfluidic flows.

The proposed SPH implementation was rigorously tested through benchmark validation cases, including droplet spherization, oscillation dynamics, and pendant drop formation. The results showed strong agreement with experimental data, with relative deviations in surface tension estimations below 1.4%, confirming the robustness of the numerical method. Moreover, the simulations accurately captured the impact of the Bond number on droplet behavior, balancing the contributions of inertial, gravitational, and capillary forces. These benchmarks support the applicability of the model across a wide range of fluid dynamics problems at small scales.

An advancement of this thesis is the efficient computational implementation of SPH for microfluidic flow simulations. Using GPU-accelerated neighbor search algorithms within the Taichi environment significantly reduced computational time, enabling high-resolution simulations of microchannel flows. This efficiency allowed for detailed analysis of velocity fields, pressure gradients, and energy dissipation mechanisms. The simulations confirmed the Newtonian behavior of water, showing a clear linear relationship between injection pressure and average fluid velocity, in agreement with classical theoretical predictions.

This thesis also contributes to the integration of experimental validation, confirming the model's accuracy in reproducing microfluidic flow under various conditions. The experimental analysis of Newtonian and non-Newtonian fluids revealed non-trivial shear rate distributions and stress-shear rate relationships, challenging conventional expectations in confined flows. Unlike macroscopic systems where laminar flow typically produces uniform shear, the results demonstrated that multiple shear and stress conditions coexist along the same microchannel, without the need to modify the geometry or forcing. This opens the possibility of using a single straight microchannel as a rheometric platform, enabling in situ viscosity measurements under variable shear

conditions.

Moreover, the stress versus shear rate curves obtained from experiments deviated from the ideal linear trend expected for Newtonian fluids; local stress variations revealed the presence of shear gradients, likely influenced by flow-wall interactions and energy dissipation effects. These findings suggest that, even for Newtonian fluids, microfluidic transport involves additional complexities such as localized shear variations that are not captured by classical models.

The experimental study of a xanthan gum and glycerin solution demonstrated a nonlinear fluid front propagation in microchannels, resulting from the combined effects of shear-thinning behavior and progressive hydrodynamic resistance. As the inlet pressure increased, the propagation exponent decreased from $m = 0.534$ at $300, Pa$ to $m = 0.367$ at $700, Pa$, indicating a transition toward a dissipation-dominated regime. Velocity profiles and stress–shear rate curves confirmed that, as the fluid advanced, local velocities and shear rates decreased, leading to an increase in apparent viscosity and reinforcing energy losses. This feedback mechanism reveals that the observed nonlinearity arises not only from the fluid's rheological properties but also from spatial variations in stress and flow resistance throughout the channel. These findings underscore the potential of microfluidic systems as versatile platforms for investigating non-Newtonian behavior and confinement-induced dissipation, with applications in biomedical diagnostics, lab-on-a-chip devices, and soft matter research.

Beyond experimental knowledge, SPH simulations provided additional insight into microfluidic dynamics. The numerical results confirmed the transition from inertia-dominated to viscous-dominated regimes, reproducing the observed scaling behavior. As pressure increased, the fluid front propagation exponent converged toward $x \sim t^{0.5}$, consistent with Washburn scaling and confirming the role of viscous dissipation in flow resistance. These findings underscore the ability of SPH to capture complex microfluidic phenomena, combining accurate surface tension modeling, localized shear variation analysis, and energy dissipation tracking within a single computational framework.

A fundamental contribution of this thesis is the integration of numerical simulations with experimental and theoretical validation, demonstrating the capacity of SPH to reproduce microfluidic behaviors with high fidelity. The synergy between computational models, experimental data, and theoretical predictions confirms the robustness of the methodology and positions this framework as a versatile tool for the design, optimization, and analysis of microfluidic systems.

Despite the strengths of this study, some limitations must be acknowledged. First, the simulations focused primarily on Newtonian and simple shear-thinning fluids; extending the model to viscoelastic or multi-phase flows remains an open avenue. Additionally, while the current setup minimized the influence of the connecting tube, entrance effects and wall interactions could still introduce deviations from idealized behavior. Future work should include control experiments with Newtonian fluids of similar viscosity, such as pure glycerin, to isolate the role of non-Newtonian properties. Further refinements may involve adaptive resolution techniques or coupling SPH with

experimental data in real-time for closed-loop microfluidic control systems.

The findings of this thesis have significant implications for the design and optimization of microfluidic devices, particularly in applications requiring precise control over shear conditions, interfacial dynamics, and flow resistance. The demonstration that multiple rheological conditions can be achieved within a single microchannel opens new possibilities for microfluidic rheometry and soft matter characterization. Furthermore, the integration of numerical and experimental approaches provides a robust framework for advancing the field of microfluidics, with potential applications in biomedicine, materials science, and chemical engineering.

7.1 Furture Work

The results of this thesis highlight the potential of SPH-based simulations for microfluidic applications, particularly in scenarios where experimental measurements present significant challenges. The integration of numerical and experimental approaches has provided a powerful framework for optimizing microfluidic device design, with applications ranging from lab-on-a-chip technologies to biomedical diagnostics and chemical processing. However, several aspects require further investigation to enhance the accuracy and applicability of the proposed model.

A key area for future research involves improving the interaction between solid and fluid phases to achieve more realistic simulations that better reflect experimental conditions using glass and PDMS microchannels. In the current model, increasing the applied pressure can lead to fluid particles penetrating the solid boundaries, introducing inconsistencies in the results. To address this limitation, more advanced solid-fluid interaction models should be implemented to ensure accurate boundary behavior, particularly in high-pressure regimes.

Additionally, expanding the SPH framework to simulate non-Newtonian fluids is crucial for further exploring multiphase interactions in microfluidic environments. The incorporation of shear-thinning and shear-thickening behaviors would allow the study of complex rheological properties, such as those observed in biological fluids and polymeric solutions, providing deeper insight into shear-dependent viscosity variations. Therefore, it is necessary to modify the code to accommodate non-Newtonian fluids, and investigating deviations from the linear flow regime in microchannels with constant (as in these theses) or variable geometries could further improve SPH prediction capabilities in microfluidic applications.

Another important aspect that requires further exploration is the development of a theoretical model to explain the nonlinear relationship observed in non-Newtonian fluids. Experimental results demonstrated the expected behavior of stress versus shear rate, but this behavior changes as a function of applied pressure. A refined theoretical framework capable of describing this behavior would allow a more accurate calculation of viscosity as a function of shear rate, improving numerical and experimental

interpretations of fluid behavior in confined microfluidic systems.

7.2 Products and publications

- Santacruz-Yunga, E., Guerrero-Rodríguez, B., Silva-Rojas, P., Pérez-Roa, R., Sigalotti, L. D. G., Trejo, C., & Plaza, E. (2025). A pair potential force model for surface tension calculations with smoothed particle hydrodynamics. Computational Particle Mechanics. https://doi.org/10.1007/s40571-025-00948-7

- Plaza, E., Santacruz, E., Aguila, D., Cobos, R., Angulo, W., Di G Sigalotti, L., & Klapp, J. (2025). Consistency and errors in Smoothed Particle Hydrodynamics using several approaches in a 2D pipe. Revista Mexicana de Física, 71(2 Mar-Apr). https://doi.org/10.31349/revmexfis.71.020602

- E. Santacruz-Yunga, P. Silva-Rojas, E. Plaza, and C. Trejo-Soto. A Smoothed Particle Hydrodynamics Modeling and Experimental Validation of Pressure-Driven Microchannel Filling (Accepted in Physics of Fluids)

- P. Silva-Rojas, E. Santacruz-Yunga, E. Plaza, and C. Trejo-Soto. A pairwise force model using SPH to simulate microfluidics channel systems: viscosity measures (Pre print)

- Growing Up Project: "Development of a Portable Viscometer for Low-Volume Samples" - GROWII23-06

8 Resumen en castellano

La presente tesis doctoral aborda el estudio de las propiedades reológicas de fluidos, mediante el desarrollo de metodologías numéricas y experimentales aplicadas a sistemas micrométricos. La investigación combina simulaciones avanzadas utilizando la técnica de Smoothed Particle Hydrodynamics (SPH) con validaciones experimentales, buscando una caracterización precisa del comportamiento de los fluidos en condiciones de baja escala y alta sensibilidad a los efectos de superficie.

El trabajo se inicia con el desarrollo de un código numérico propio basado en SPH, que permite la simulación tridimensional del flujo de fluidos con superficies libres. Este código fue construido, considerando la eficiente distribución de partículas, la optimización de los algoritmos de búsqueda de vecinos y la correcta implementación de las ecuaciones de estado, densidad y viscosidad para resolver el movimiento de partículas en un contexto lagrangiano. La estructura del código garantiza estabilidad numérica y tiempos de simulación competitivos para sistemas con alta densidad de partículas.

Uno de los principales aportes de la tesis es la implementación de un modelo numérico para simular la tensión superficial sin necesidad de incluir la fase gaseosa, mejorando así la eficiencia computacional. Para ello, se propuso el uso de fuerzas de interacción por pares (pair potential force), adaptadas a la metodología SPH, que permiten replicar de manera realista los efectos de cohesión interna en la fase líquida. Estas fuerzas fueron calibradas mediante la ecuación de Young-Laplace para lograr que el modelo reproduzca con precisión el fenómeno de esferización de gotas. Se realizaron pruebas a diferentes escalas de discretización y volúmenes, confirmando que la metodología es estable y reproducible en diferentes condiciones.

La validación del modelo incluyó simulaciones de formación de gotas desde una configuración inicial cúbica, observando la evolución hacia una forma esférica como resultado de la acción de las fuerzas internas. Durante este proceso, se monitorizó la velocidad y la densidad de las partículas, evidenciando un proceso de estabilización que tiende a minimizar la energía del sistema. Los resultados obtenidos fueron comparados con valores teóricos y bibliográficos de tensión superficial para diferentes fluidos, incluyendo agua, etanol y etilenglicol, mostrando errores relativos inferiores al 2.7% en la mayoría de los casos.

Para ampliar la validación, se realizaron experimentos de caída libre de gotas sobre superficies planas, simulando condiciones hidrofóbicas. Estos ensayos se llevaron a cabo para volúmenes de $2\,\mu L$ y $2\,mL$, representando casos donde la tensión superficial domina (Bond número < 1) y donde la gravedad supera a las fuerzas internas (Bond número > 1). Las simulaciones reprodujeron adecuadamente ambos regímenes, mostrando es-

ferización y expansión del fluido sobre la superficie según correspondía. Además, se demostró que la metodología conserva propiedades fundamentales como densidad y tensión superficial incluso al modificar la cantidad de partículas en la simulación, lo que valida su escalabilidad y robustez.

Un aspecto destacado de la tesis es la comparación entre las simulaciones numéricas y modelos teóricos de oscilación de gotas. Se utilizó como referencia un modelo tridimensional propuesto por Aalilija, que describe el comportamiento de oscilaciones amortiguadas en líquidos newtonianos. Las simulaciones SPH replicaron las oscilaciones inducidas por perturbaciones iniciales, mostrando períodos de oscilación similares a los teóricos y confirmando la capacidad del modelo para representar fenómenos dinámicos de superficies libres.

Se realizaron experimentos de tensión superficial mediante el método de Tate para tres fluidos diferentes. Los resultados experimentales mostraron buena concordancia con los valores bibliográficos, con errores aceptables considerando la volatilidad y viscosidad de los fluidos estudiados. Además, se validó la geometría de las gotas formadas experimentalmente con las obtenidas en las simulaciones, mostrando excelente correlación en el parámetro geométrico D/d, que relaciona el diámetro de la gota con el diámetro del tubo. Los resultados anteriores se encuentran en la siguiente publicación:[https://doi.org/10.1007/s40571-025-00948-7]

Adicionalmente, se realizaron simulaciones del proceso de llenado en microcanales utilizando el modelo previamente validado. Para ello, se implementó una presión hidrostática modificada que permitió simular la fuerza impulsora sin necesidad de establecer condiciones de frontera específicas en la entrada y salida del canal. Los resultados obtenidos para microcanales de $150\,\mu m$ y $300\,\mu m$ de altura, $1\,mm$ de ancho y $6\,mm$ de largo mostraron que el modelo numérico reproduce con alta precisión la propagación del frente de fluido bajo diferentes condiciones de presión aplicada. El análisis cuantitativo mediante el cálculo del error cuadrático medio (ECM) y del coeficiente de determinación (R^2) demostró una excelente correlación entre las simulaciones y las predicciones teóricas, con errores mínimos y ajustes superiores al 99% en la mayoría de los casos. Además, se exploró la relación entre la presión diferencial y la velocidad promedio del fluido, observando una clara tendencia lineal que valida la hipótesis de flujo laminar y cuasi-estacionario, incluso durante el proceso transitorio de llenado. Este comportamiento es coherente con las bajas velocidades observadas y los números de Reynolds cercanos a la unidad, lo que permite asumir que los efectos inerciales son despreciables.

En el componente experimental, se diseñaron y fabricaron microcanales con alturas de $150\,\mu m$ y $300\,\mu m$, ancho de $1\,mm$ y largo de $40\,mm$. Estos microcanales fueron utilizados para estudiar la propagación de frentes de fluidos bajo diferentes presiones aplicadas. Los experimentos se llevaron a cabo utilizando agua, como fluido newtoniano de referencia, y soluciones de goma xantana al 0.03% en combinación con glicerina al 30%, que actúan como análogos reológicos de la sangre. A través de técnicas de procesamiento de imágenes, se obtuvieron datos experimentales de posición y tiempo

del frente de fluido, lo que permitió calcular la velocidad de propagación y, a partir de ella, determinar el esfuerzo cortante y la tasa de deformación en diferentes secciones del microcanal.

Con estos datos, se calculó la viscosidad local del fluido mediante la relación entre el esfuerzo cortante y la tasa de cizalla en cada tramo del canal. Para el caso del agua, se comprobó que la viscosidad se mantuvo prácticamente constante en todas las condiciones de presión y a lo largo de la longitud del canal, confirmando su comportamiento newtoniano y validando la metodología experimental, computacional y teórica. Este resultado demuestra que, a pesar de las variaciones en el esfuerzo cortante y la tasa de deformación impuestas por los diferentes gradientes de presión, la viscosidad permanece invariable, como se espera para un fluido newtoniano.

En el caso del análogo de sangre (solución de goma xantana y glicerina), se evidenció que el avance del fluido no sigue una relación estrictamente lineal con el tiempo (lo que se habia observado previamente en las simulaciones). Esto se atribuye a la pérdida progresiva de energía durante la propagación, lo que genera un aumento en la resistencia hidráulica conforme el frente del fluido avanza. Esta dinámica acoplada afecta simultáneamente a la velocidad y a la viscosidad local del fluido, lo que implica que la viscosidad es dependiente de la tasa de deformación. El análisis experimental permitió ajustar los datos a una ley de potencia de la forma $x(t) = At^m$, observándose que el exponente de propagación m disminuye a medida que se incrementa la presión aplicada, lo que indica una aproximación progresiva al régimen descrito por la ley de Washburn.

En conclusión, la tesis demuestra que es posible modelar de manera precisa y eficiente las propiedades reológicas y los fenómenos de superficie libre en fluidos utilizando SPH con fuerzas internas calibradas. La metodología desarrollada es robusta, reproducible y aplicable a diferentes escalas y condiciones experimentales. Además, la integración de resultados numéricos y experimentales permite avanzar significativamente en la caracterización de flujos microfluídicos complejos, con aplicaciones potenciales en el diseño de dispositivos médicos, análisis de fluidos biológicos y optimización de procesos industriales que involucren flujos a microescala.

Bibliography

[1] B.-B. Lee, P. Ravindra, and E.-S. Chan, "A critical review: Surface and interfacial tension measurement by the drop weight method," *Chemical Engineering Communications*, vol. 195, no. 8, pp. 889–924, Apr. 2008, ISSN: 1563-5201. DOI: 10.1080/00986440801905056. [Online]. Available: http://dx.doi.org/10.1080/00986440801905056.

[2] S. J. Lind, B. D. Rogers, and P. K. Stansby, "Review of smoothed particle hydrodynamics: Towards converged lagrangian flow modelling," *Proceedings of the Royal Society A: Mathematical, Physical and Engineering Sciences*, vol. 476, no. 2241, Sep. 2020, ISSN: 1471-2946. DOI: 10.1098/rspa.2019.0801. [Online]. Available: http://dx.doi.org/10.1098/rspa.2019.0801.

[3] J. J. Monaghan, "Smoothed particle hydrodynamics," *Annual Review of Astronomy and Astrophysics*, vol. 30, pp. 543–574, Sep. 1992. DOI: doi:10.1146/annurev.aa.30.090192.002551..

[4] D. Violeau, *Fluid Mechanics and the SPH Method Theory and Applications*. United Kingdom: Oxford, University press, 2012.

[5] J. J. Monaghan, "Simulating free surface flows with sph," *Journal of Computational Physics*, vol. 110, pp. 399–406, 1994. DOI: https://doi.org/10.1006/jcph.1994.1034.

[6] A. M. Tartakovsky and A. Panchenko, "Pairwise force smoothed particle hydrodynamics model for multiphase flow: Surface tension and contact line dynamics," *Journal of Computational Physics*, vol. 305, pp. 1119–1146, 2016.

[7] Q. Yang, F. Xu, Y. Yang, and L. Wang, "A multi-phase sph model based on riemann solvers for simulation of jet breakup," *Engineering Analysis with Boundary Elements*, vol. 111, pp. 134–147, 2020.

[8] X. Hu and N. Adams, "A multi-phase sph method for macroscopic and mesoscopic flows," *Journal of Computational Physics*, vol. 213, no. 2, pp. 844–861, Apr. 2006, ISSN: 0021-9991. DOI: 10.1016/j.jcp.2005.09.001. [Online]. Available: http://dx.doi.org/10.1016/j.jcp.2005.09.001.

[9] F. H. Harlow, J. E. Welch, *et al.*, "Numerical calculation of time-dependent viscous incompressible flow of fluid with free surface," *Physics of fluids*, vol. 8, no. 12, p. 2182, 1965.

[10] H. Jasak, H. Weller, and A. Gosman, "High resolution nvd differencing scheme for arbitrarily unstructured meshes," *International Journal for Numerical Methods in Fluids*, vol. 31, no. 2, pp. 431–449, Sep. 1999, ISSN: 1097-0363. DOI: 10.1002/(sici)1097-0363(19990930)31:2<431::aid-fld884>3.0.co;2-t. [Online]. Available: http://dx.doi.org/10.1002/(SICI)1097-0363(19990930)31:2%3C431::AID-FLD884%3E3.0.CO;2-T.

[11] V. John, *Finite Element Methods for Incompressible Flow Problems*. Springer International Publishing, 2016, ISBN: 9783319457505. DOI: 10.1007/978-3-319-45750-5. [Online]. Available: http://dx.doi.org/10.1007/978-3-319-45750-5.

[12] C. Crowe, M. Sommerfeld, Y. Tsuji, *et al.*, *Multiphase flows with*. Ž, 1998, vol. 906.

[13] L. B. Lucy, "A numerical approach to the testing of the fission hypothesis," *The Astronomical Journal*, vol. 82, no. 12, pp. 1013–1024, Sep. 1977. DOI: doi:10.1086/112164.

[14] R. A. Gingold and J. J. Monaghan, "Smoothed particle hydrodynamics: Theory and application to non-spherical stars," *Monthly Notices of the Royal Astronomical Society*, vol. 181, pp. 375–389, Feb. 1977. DOI: doi:10.1093/mnras/181.3.375.

[15] Z.-B. Wang, R. Chen, H. Wang, Q. Liao, X. Zhu, and S.-Z. Li, "An overview of smoothed particle hydrodynamics for simulating multiphase flow," *Applied Mathematical Modelling*, vol. 40, no. 23–24, pp. 9625–9655, Dec. 2016, ISSN: 0307-904X. DOI: 10.1016/j.apm.2016.06.030. [Online]. Available: http://dx.doi.org/10.1016/j.apm.2016.06.030.

[16] M. Luo, X. Su, E. Kazemi, X. Jin, and A. Khayyer, "Review of smoothed particle hydrodynamics modeling of fluid flows in porous media with a focus on hydraulic, coastal, and ocean engineering applications," *Physics of Fluids*, vol. 37, no. 2, Feb. 2025, ISSN: 1089-7666. DOI: 10.1063/5.0252125. [Online]. Available: http://dx.doi.org/10.1063/5.0252125.

[17] C. Zhang, Y.-j. Zhu, D. Wu, N. A. Adams, and X. Hu, "Smoothed particle hydrodynamics: Methodology development and recent achievement," *Journal of Hydrodynamics*, vol. 34, no. 5, pp. 767–805, Oct. 2022, ISSN: 1878-0342. DOI: 10.1007/s42241-022-0052-1. [Online]. Available: http://dx.doi.org/10.1007/s42241-022-0052-1.

[18] X. Yang, S.-C. Kong, and Q. Liu, "Smoothed particle hydrodynamics with adaptive spatial resolution for multiphase flows with large density ratio," *Physical Review E*, vol. 104, no. 5, Nov. 2021, ISSN: 2470-0053. DOI: 10.1103/physreve.104.055308. [Online]. Available: http://dx.doi.org/10.1103/PhysRevE.104.055308.

[19] D. Mobius and R. Miller, *Drops and bubbles in interfacial research*. Elsevier, 1997.

[20] R. S. Burdon, *Surface tension and the spreading of liquids*. Cambridge University Press, 2014.

[21] A. Colagrossi and M. Landrini, "Numerical simulation of interfacial flows by smoothed particle hydrodynamics," *Journal of Computational Physics*, vol. 191, no. 2, pp. 448–475, Nov. 2003, ISSN: 0021-9991. DOI: 10.1016/s0021-9991(03)00324-3. [Online]. Available: http://dx.doi.org/10.1016/S0021-9991(03)00324-3.

[22] S. Marrone, A. Colagrossi, M. Antuono, G. Colicchio, and G. Graziani, "An accurate sph modeling of viscous flows around bodies at low and moderate reynolds numbers," *Journal of Computational Physics*, vol. 245, pp. 456–475, Jul. 2013, ISSN: 0021-9991. DOI: 10.1016/j.jcp.2013.03.011. [Online]. Available: http://dx.doi.org/10.1016/j.jcp.2013.03.011.

[23] X. Wang, S. Ramírez-Hinestrosa, J. Dobnikar, and D. Frenkel, "The lennard-jones potential: When (not) to use it," *Physical Chemistry Chemical Physics*, vol. 22, no. 19, pp. 10 624–10 633, 2020.

[24] Z.-B. Wang, R. Chen, H. Wang, Q. Liao, X. Zhu, and S.-Z. Li, "An overview of smoothed particle hydrodynamics for simulating multiphase flow," *Applied Mathematical Modelling*, vol. 40, no. 23-24, pp. 9625–9655, 2016.

[25] L. Yang, M. Rakhsha, and D. Negrut, "Comparison of surface tension models in smoothed particles hydrodynamics method," in *International Design Engineering Technical Conferences and Computers and Information in Engineering Conference*, American Society of Mechanical Engineers, vol. 59261, 2019.

[26] T. Ye, D. Pan, C. Huang, and M. Liu, "Smoothed particle hydrodynamics (sph) for complex fluid flows: Recent developments in methodology and applications," *Physics of Fluids*, vol. 31, no. 1, pp. 575–588, 2019.

[27] K. Broekema, "Tuning the surface tension in sph independently of the fluid rheology," 2020.

[28] E. Arai, A. Tartakovsky, G. Holt, S. Grace, and E. Ryan, "Comparison of surface tension generation methods in smoothed particle hydrodynamics for dynamic systems," *Computers and Fluids*, vol. 104540, pp. 1–13, 2020. DOI: "https://doi.org/10.1016/j.compfluid.2020.104540".

[29] A. Tartakovsky and A. Panchenko, "Pairwise force smoothed particle hydrodynamics model for multiphase flow: Surface tension and contact line dynamics," *Journal of Computational Physics*, vol. 305, pp. 1119–1146, 2016. DOI: "http://dx.doi.org/10.1016/j.jcp.2015.08.037".

[30] H. Amanda and A. Tartakovsky, "Non-local model for surface tension in fluid-fluid simulations," *Journal of Computational Physics*, vol. 109732, pp. 1119–1146, 2020. DOI: "doi:https://doi.org/10.1016/j.jcp.2020.109732".

[31] J. P. Morris, "Simulating surface tension with smoothed particle hydrodynamics," *International journal for numerical methods in fluids*, vol. 33, no. 3, pp. 333–353, 2000.

[32] M. Olejnik and J. Pozorski, "A robust method for wetting phenomena within smoothed particle hydrodynamics," *Flow, Turbulence and Combustion*, vol. 104, pp. 115–137, 2020.

[33] J.-P. Fürstenau, C. Weißenfels, and P. Wriggers, "Free surface tension in incompressible smoothed particle hydrodynamcis (isph)," *Computational Mechanics*, vol. 65, pp. 487–502, 2020.

[34] M. Blank, P. Nair, and T. Pöschel, "Modeling surface tension in smoothed particle hydrodynamics using young–laplace pressure boundary condition," *Computer Methods in Applied Mechanics and Engineering*, vol. 406, p. 115 907, 2023.

[35] L. Wen-Bin, M. Dong-Jun, Z. Ming-Yu, H. An-Min, L. Nan-Sheng, and W. Pei, "A new surface tension formulation in smoothed particle hydrodynamics for free-surface flows," *Journal of Computational Physics*, vol. 439, 2021.

[36] S. Fedir V and Y. Jack J, "A new particle method for simulating breakup of liquid jets," *Journal of Computational Physics*, vol. 231, 2012.

[37] M. Kondo and J. Matsumoto, "Surface tension and wettability calculation using density gradient potential in a physically consistent particle method," *Computer Methods in Applied Mechanics and Engineering*, vol. 385, p. 114 072, 2021.

[38] A. Tartakovsky and P. Meakin, "Modeling of surface tension and contact angles with smoothed particle hydrodynamics," *Physical Review E*, vol. 72, no. 2, p. 026 301, 2005.

[39] Q. Yang, J. Yao, Z. Huang, G. Zhu, L. Liu, and W. Song, "Pore-scale investigation of petro-physical fluid behaviours based on multiphase sph method," *Journal of Petroleum Science and Engineering*, vol. 192, p. 107 238, 2020.

[40] P. Nair and T. Pöschel, "Dynamic capillary phenomena using incompressible sph," *Chemical Engineering Science*, vol. 176, pp. 192–204, 2018.

[41] M. Yang, X. Li, Y. Liu, G. Yang, and E. Wu, "A novel surface tension formulation for sph fluid simulation," *The Visual Computer*, vol. 33, pp. 597–606, 2017.

[42] S. Champmartin, A. Ambari, and J.-Y. Le Pommelec, "New procedure to measure simultaneously the surface tension and contact angle," *Review of Scientific Instruments*, vol. 87, no. 5, 2016.

[43] G. M. Whitesides, "The origins and the future of microfluidics," *Nature*, vol. 442, no. 7101, pp. 368–373, Jul. 2006, ISSN: 1476-4687. DOI: 10.1038/nature05058. [Online]. Available: http://dx.doi.org/10.1038/nature05058.

[44] G. Gharib *et al.*, "Biomedical applications of microfluidic devices: A review," *Biosensors*, vol. 12, no. 11, p. 1023, Nov. 2022, ISSN: 2079-6374. DOI: 10.3390/bios12111023. [Online]. Available: http://dx.doi.org/10.3390/bios12111023.

[45] T. M. Squires and S. R. Quake, "Microfluidics: Fluid physics at the nanoliter scale," *Reviews of Modern Physics*, vol. 77, no. 3, pp. 977–1026, Oct. 2005, ISSN: 1539-0756. DOI: 10.1103/revmodphys.77.977. [Online]. Available: http://dx.doi.org/10.1103/RevModPhys.77.977.

[46] H. Stone, A. Stroock, and A. Ajdari, "Engineering flows in small devices: Microfluidics toward a lab-on-a-chip," *Annual Review of Fluid Mechanics*, vol. 36, no. 1, pp. 381–411, Jan. 2004, ISSN: 1545-4479. DOI: 10.1146/annurev.fluid.36.050802.122124. [Online]. Available: http://dx.doi.org/10.1146/annurev.fluid.36.050802.122124.

[47] A. B. Theberge *et al.*, "Microdroplets in microfluidics: An evolving platform for discoveries in chemistry and biology," *Angewandte Chemie International Edition*, vol. 49, no. 34, pp. 5846–5868, 2010.

[48] B. E. Debs, R. Utharala, I. V. Balyasnikova, A. D. Griffiths, and C. A. Merten, "Functional single-cell hybridoma screening using droplet-based microfluidics," *Proceedings of the National Academy of Sciences*, vol. 109, no. 29, pp. 11 570–11 575, Jul. 2012, ISSN: 1091-6490. DOI: 10.1073/pnas.1204514109. [Online]. Available: http://dx.doi.org/10.1073/pnas.1204514109.

[49] S. Park, Y. Zhang, S. Lin, T.-H. Wang, and S. Yang, "Advances in microfluidic pcr for point-of-care infectious disease diagnostics," *Biotechnology Advances*, vol. 29, no. 6, pp. 830–839, Nov. 2011, ISSN: 0734-9750. DOI: 10.1016/j.biotechadv.2011.06.017. [Online]. Available: http://dx.doi.org/10.1016/j.biotechadv.2011.06.017.

[50] S. L. Anna, N. Bontoux, and H. A. Stone, "Formation of dispersions using "flow focusing" in microchannels," *Applied physics letters*, vol. 82, no. 3, pp. 364–366, 2003.

[51] D. B. Weibel and G. M. Whitesides, "Applications of microfluidics in chemical biology," *Current opinion in chemical biology*, vol. 10, no. 6, pp. 584–591, 2006.

[52] C. Trejo-Soto, G. R. Lázaro, I. Pagonabarraga, and A. Hernández-Machado, "Microfluidics approach to the mechanical properties of red blood cell membrane and their effect on blood rheology," *Membranes*, vol. 12, no. 2, p. 217, Feb. 2022, ISSN: 2077-0375. DOI: 10.3390/membranes12020217. [Online]. Available: http://dx.doi.org/10.3390/membranes12020217.

[53] L. Méndez-Mora *et al.*, "Blood rheological characterization of -thalassemia trait and iron deficiency anemia using front microrheometry," *Frontiers in Physiology*, vol. 12, Oct. 2021, ISSN: 1664-042X. DOI: 10.3389/fphys.2021.761411. [Online]. Available: http://dx.doi.org/10.3389/fphys.2021.761411.

[54] C. Trejo-Soto and A. Hernández-Machado, "Normalization of blood viscosity according to the hematocrit and the shear rate," *Micromachines*, vol. 13, no. 3, p. 357, Feb. 2022, ISSN: 2072-666X. DOI: 10.3390/mi13030357. [Online]. Available: http://dx.doi.org/10.3390/mi13030357.

[55] S. Becker and A. Kuznetsov, *Transport in Biological Media*. Elsevier, 2013, ISBN: 9780123978493. [Online]. Available: https://books.google.cl/books?id=48KN4BFvqAAC.

[56] S. Hoath, *Fundamentals of Inkjet Printing: The Science of Inkjet and Droplets*. Wiley, 2016, ISBN: 9783527337859. [Online]. Available: https://books.google.cl/books?id=S6XpCgAAQBAJ.

[57] *Aerosols - Science and Technology*. Wiley, Jun. 2010, ISBN: 9783527630134. DOI: 10.1002/9783527630134. [Online]. Available: http://dx.doi.org/10.1002/9783527630134.

[58] K. J. Vachaparambil and K. E. Einarsrud, "Comparison of surface tension models for the volume of fluid method," *Processes*, vol. 7, no. 8, p. 542, Aug. 2019, ISSN: 2227-9717. DOI: 10.3390/pr7080542. [Online]. Available: http://dx.doi.org/10.3390/pr7080542.

[59] J. Fernández-Fidalgo, L. Cueto-Felgueroso, L. Ramírez, A. Martínez, and X. Nogueira, "Pore-scale simulation of multiphase flows using equations of state that preserve the correct surface tension," *Computer Methods in Applied Mechanics and Engineering*, vol. 428, p. 117 072, Aug. 2024, ISSN: 0045-7825. DOI: 10.1016/j.cma.2024.117072. [Online]. Available: http://dx.doi.org/10.1016/j.cma.2024.117072.

[60] M. Liu and G. Liu, "Restoring particle consistency in smoothed particle hydrodynamics," *Applied Numerical Mathematics*, vol. 56, pp. 19–36, 2006. DOI: https://doi.org/10.1016/j.apnum.2005.02.012.

[61] E. Chatzoglou, A. Liakopoulos, and F. Sofos, "Smoothed particle hydrodynamics-based study of 3d confined microflows," *Fluids*, vol. 8, no. 5, p. 137, Apr. 2023, ISSN: 2311-5521. DOI: 10.3390/fluids8050137. [Online]. Available: http://dx.doi.org/10.3390/fluids8050137.

[62] M. Bagheri, M. Mohammadi, and M. Riazi, "A review of smoothed particle hydrodynamics," *Computational Particle Mechanics*, vol. 11, no. 3, pp. 1163–1219, Nov. 2023, ISSN: 2196-4386. DOI: 10.1007/s40571-023-00679-7. [Online]. Available: http://dx.doi.org/10.1007/s40571-023-00679-7.

[63] S. Sibilla *et al.*, "Smoothed particle hydrodynamics multiphase modelling of an experimental microfluidic device for conformal coating of pancreatic islets," *Medical Engineering & Physics*, vol. 77, pp. 19–30, Mar. 2020, ISSN: 1350-4533. DOI: 10.1016/j.medengphy.2020.01.004. [Online]. Available: http://dx.doi.org/10.1016/j.medengphy.2020.01.004.

[64] R. Bird, W. Stewart, and E. Lightfoot, *Transport Phenomena* (Transport Phenomena v. 1). Wiley, 2006, ISBN: 9780470115398. [Online]. Available: https://books.google.cl/books?id=L5FnNlIaGfcC.

[65] F. White, *Viscous Fluid Flow* (McGraw-Hill international edition). McGraw-Hill Higher Education, 2006, ISBN: 9780071244930. [Online]. Available: https://books.google.cl/books?id=fl6wPwAACAAJ.

[66] P. Kundu, *Fluid Mechanics* (Fluid Mechanics). Academic Press, 2013, ISBN: 9780323140249. [Online]. Available: https://books.google.cl/books?id=uYh22vnC6NcC.

[67] L. Landau and E. Lifshitz, *Fluid Mechanics: Volume 6*. Pergamon, 2013, ISBN: 9781483140506. [Online]. Available: https://books.google.cl/books?id=CeBbAwAAQBAJ.

[68] G. K. Batchelor, *An Introduction to Fluid Dynamics*. Cambridge: Cambridge University Press, 1967.

[69] R. Mott, C. Pedraza, and A. Samaniego, *Mecánica de fluidos aplicada*. Pearson Educación, 1996, ISBN: 9789688805428. [Online]. Available: https://books.google.cl/books?id=xUavR0u66PEC.

[70] H. Bruus, *Theoretical Microfluidics* (Oxford Master Series in Physics). OUP Oxford, 2008, ISBN: 9780199235087. [Online]. Available: https://books.google.cl/books?id=FZz3j46Fq2sC.

[71] C. Mayes, H. Schlichting, E. Krause, H. Oertel, and K. Gersten, *Boundary-Layer Theory*. Springer Berlin Heidelberg, 2014, ISBN: 9783642858314. [Online]. Available: https://books.google.cl/books?id=WtIKrgEACAAJ.

[72] R. B. Bird, R. C. Armstrong, and O. Hassager, "Dynamics of polymeric liquids. vol. 1: Fluid mechanics," 1987.

[73] H. Barnes, "Shear-thickening ("dilatancy") in suspensions of nonaggregating solid particles dispersed in newtonian liquids," *Journal of Rheology*, vol. 33, no. 2, pp. 329–366, 1989.

[74] N. J. Wagner and J. F. Brady, "Shear thickening in colloidal dispersions," *Physics Today*, vol. 62, no. 10, pp. 27–32, Oct. 2009, ISSN: 1945-0699. DOI: 10.1063/1.3248476. [Online]. Available: http://dx.doi.org/10.1063/1.3248476.

[75] J. D. Goddard, "Mechanics of non-newtonian fluids.," *Journal of Fluid Mechanics*, vol. 100, no. 3, pp. 671–672, 1980. DOI: 10.1017/S0022112080221330.

[76] C. Macosko, *Rheology: Principles, Measurements, and Applications* (Advances in interfacial engineering series). VCH, 1994, ISBN: 9781560815792. [Online]. Available: https://books.google.cl/books?id=XXspAQAAMAAJ.

[77] R. Ashena, F. Badrouchi, A. Elmgerbi, S. Mishani, F. Sotoudeh, and S. Nekoeian, "Stepwise mathematical derivation of the herschel–bulkley laminar fluid flow equations—in pipes," *Journal of Petroleum Exploration and Production Technology*, vol. 13, no. 2, pp. 625–643, Oct. 2022, ISSN: 2190-0566. DOI: 10.1007/s13202-022-01566-2. [Online]. Available: http://dx.doi.org/10.1007/s13202-022-01566-2.

[78] M. M. Cross, "Rheology of non-newtonian fluids: A new flow equation for pseudoplastic systems," *Journal of Colloid Science*, vol. 20, no. 5, pp. 417–437, Jun. 1965, ISSN: 0095-8522. DOI: 10.1016/0095-8522(65)90022-x. [Online]. Available: http://dx.doi.org/10.1016/0095-8522(65)90022-X.

[79] G. Karniadakis, A. Beskok, and N. Aluru, *Microflows and Nanoflows: Fundamentals and Simulation* (Interdisciplinary Applied Mathematics). Springer New York, 2006, ISBN: 9780387286761. [Online]. Available: https://books.google.cl/books?id=vDiLnJHSqvYC.

[80] N. Nguyen, S. Wereley, and S. Shaegh, *Fundamentals and Applications of Microfluidics, Third Edition* (Artech House integrated microsystems series). Artech House, 2019, ISBN: 9781630813659. [Online]. Available: https://books.google.cl/books?id=h3iFDwAAQBAJ.

[81] C. Trejo-Soto, E. Costa-Miracle, I. Rodriguez-Villarreal, J. Cid, T. Alarcón, and A. Hernández-Machado, "Capillary filling at the microscale: Control of fluid front using geometry," *PLOS ONE*, vol. 11, no. 4, V. M. Ugaz, Ed., e0153559, Apr. 2016, ISSN: 1932-6203. DOI: 10.1371/journal.pone.0153559. [Online]. Available: http://dx.doi.org/10.1371/journal.pone.0153559.

[82] Y. Son, "Determination of shear viscosity and shear rate from pressure drop and flow rate relationship in a rectangular channel," *Polymer*, vol. 48, no. 2, pp. 632–637, Jan. 2007, ISSN: 0032-3861. DOI: 10.1016/j.polymer.2006.11.048. [Online]. Available: http://dx.doi.org/10.1016/j.polymer.2006.11.048.

[83] E. W. Washburn, "The dynamics of capillary flow," *Physical review*, vol. 17, no. 3, p. 273, 1921.

[84] D. Gosselin, J. Berthier, G. Delapierre, D. Chaussy, and N. Belgacem, "Capillary flows: Dynamics and geometry effects," in *Proceedings of the 2015 COMSOL Conference in Grenoble*, 2015.

[85] C. K. Camplisson, K. M. Schilling, W. L. Pedrotti, H. A. Stone, and A. W. Martinez, "Two-ply channels for faster wicking in paper-based microfluidic devices," *Lab on a Chip*, vol. 15, no. 23, pp. 4461–4466, 2015, ISSN: 1473-0189. DOI: 10.1039/c5lc01115a. [Online]. Available: http://dx.doi.org/10.1039/c5lc01115a.

[86] J. Berthier, D. Gosselin, and E. Berthier, "A generalization of the lucas–washburn–rideal law to composite microchannels of arbitrary cross section," *Microfluidics and Nanofluidics*, vol. 19, no. 3, pp. 497–507, May 2015, ISSN: 1613-4990. DOI: 10.1007/s10404-014-1519-3. [Online]. Available: http://dx.doi.org/10.1007/s10404-014-1519-3.

[87] D. Tabor, *Gases, liquids and solids: and other states of matter*. Cambridge university press, 1991.

[88] S. M. Skjæveland, *Derivations of the young-laplace equation*, en, 2015. DOI: 10.13140/RG.2.1.4485.5768. [Online]. Available: http://rgdoi.net/10.13140/RG.2.1.4485.5768.

[89] S. Misra and Y. Jin, "Effects of wettability of conductive and nonconductive particles on the multifrequency electromagnetic response of porous material," *Multifrequency Electromagnetic Data Interpretation for Subsurface Characterization*, p. 145, 2021.

[90] L. Zhang, Z.-D. Li, and J.-F. Zhao, "Rebound of liquid droplets caused by sudden decrease of gravity," *Interfacial Phenomena and Heat Transfer*, vol. 2, no. 1, 2014.

[91] G. R. Liu and M. B. Liu, *Smoothed Particle Hydrodynamics: A Meshfree Particle Method*. Singapore: World Scientific, 2003.

[92] H. Wendland, "Piecewise polynomial, positive definite and compactly supported radial functions of minimal degree," *Advances in computational Mathematics*, vol. 4, pp. 389–396, 1995.

[93] E. Y. Lo and S. Shao, "Simulation of near-shore solitary wave mechanics by an incompressible sph method," *Applied Ocean Research*, vol. 24, pp. 275–286, 2002. DOI: doi:10.1016/S0141-1187(03)00002-6.

[94] L. Verlet, "Computer" experiments" on classical fluids. i. thermodynamical properties of lennard-jones molecules," *Physical review*, vol. 159, no. 1, p. 98, 1967.

[95] J. J. Monaghan and A. Kos, "Solitary waves on a cretan beach," *Journal of waterway, port, coastal, and ocean engineering*, vol. 125, no. 3, pp. 145–155, 1999.

[96] Y. Hu, T.-M. Li, L. Anderson, J. Ragan-Kelley, and F. Durand, "Taichi: A language for high-performance computation on spatially sparse data structures," *ACM Transactions on Graphics (TOG)*, vol. 38, no. 6, p. 201, 2019.

[97] T. M. Inc., *Matlab version: 23.2.0.2428915 (r2023b)*, Natick, Massachusetts, United States, 2023. [Online]. Available: https://www.mathworks.com.

[98] S. Lefebvre and H. Hoppe, "Perfect spatial hashing," *ACM Trans. Graph.*, vol. 25, no. 3, pp. 579–588, Jul. 2006, ISSN: 0730-0301. DOI: 10.1145/1141911.1141926. [Online]. Available: https://doi.org/10.1145/1141911.1141926.

[99] D. Violeau and T. Fonty, "Calculating the smoothing error in sph.," *Computers and Fluids*, vol. 191, no. 104240, 2019. DOI: https://doi.org/10.1016/j.compÃ§uid.2019.104240.

[100] J. P. Morris, P. J. Fox, and Y. Zhu, "Modeling low reynolds number incompressible flows using sph.," *Journal of computational physics*, vol. 136, pp. 214–226, 1997. DOI: https://doi.org/10.1006/jcph.1997.5776.

[101] D. D. Bank, *Surface tension of water*, http://www.http://ddbonline.ddbst.com/DIPPR106SFTCalculation/DIPPR106SFTCalculationCGI.exe, 2024.

[102] Z. Chi, Z. Yujie, W. Dong, and H. Xiangyu, "Review on smoothed particle hydrodynamics: Methodology development and recent achievement," *Journal of Hydrodynamics*, vol. 34, pp. 767–805, 1995.

[103] M. C. A. and S. L. E., "The oscillations of a fluid droplet immersed in another fluid," *Journal of Fluid Mechanics*, vol. 32, pp. 417–435, 1968. DOI: "DOI:https://doi.org/10.1017/S0022112068000832".

[104] A. A., G. Ch.-A, and H. E., "On the analytical and numerical simulation of an oscillating drop in zero-gravity," *Computer and Fluids*, vol. 197, no. 104362, 2020. DOI: "https://doi.org/10.1016/j.compfluid.2019.104362".

[105] T. Tate, "Xxx. on the magnitude of a drop of liquid formed under different circumstances," *The London, Edinburgh, and Dublin Philosophical Magazine and Journal of Science*, vol. 27, no. 181, pp. 176–180, 1864. DOI: 10.1080/14786446408643645.

[106] O. E. Yildirim, Q. Xu, and O. A. Basaran, "Analysis of the drop weight method," *Physics of Fluids*, vol. 17, no. 6, 2005.

[107] P. Silva-Rojas, *Low flow syringe pump*, https://github.com/pablosilvarojas93/Low-flow-syringe-pump.git, versión 1.1.3, 2024.

[108] C. A. Schneider, W. S. Rasband, and K. W. Eliceiri, "Nih image to imagej: 25 years of image analysis," *Nature Methods*, vol. 9, no. 7, pp. 671–675, 2012.

[109] T. E. ToolBox, *Surface tension*, https://www.engineeringtoolbox.com/surface-tension-d_962.html, [Accessed 13 Aug 2024], 2005.

[110] F. A. M. M. Gonçalves *et al.*, "Pvt, viscosity, and surface tension of ethanol: New measurements and literature data evaluation," *The Journal of Chemical Thermodynamics*, vol. 42, no. 8, pp. 1039–1049, 2010.

[111] S. H. Anastasiadis, J.-K. Chen, J. T. Koberstein, A. F. Siegel, J. E. Sohn, and J. A. Emerson, "The determination of interfacial tension by video image processing of pendant fluid drops," *Journal of Colloid and Interface Science*, vol. 119, no. 1, pp. 55–66, 1987.

[112] J. C. Earnshaw, E. G. Johnson, B. J. Carroll, and P. J. Doyle, "The drop volume method for interfacial tension determination: An error analysis," *Journal of Colloid and Interface Science*, vol. 177, no. 1, pp. 150–155, 1996.

[113] C. Molina, L. Victoria, and A. Arenas, "Measuring the surface tension of a liquid–gas interface by automatic stalagmometer," *Review of Scientific Instruments*, vol. 71, no. 6, pp. 2481–2486, 2000.

[114] S. S. Yadav, B. S. Sikarwar, P. Ranjan, R. Janardhanan, and A. Goyal, "Surface tension measurement of normal human blood samples by pendant drop method," *Journal of Medical Engineering & Technology*, vol. 44, no. 5, pp. 227–236, 2020.

[115] Anushka, A. Bandopadhyay, and P. K. Das, "Paper based microfluidic devices: A review of fabrication techniques and applications," *The European Physical Journal Special Topics*, vol. 232, no. 6, pp. 781–815, Dec. 2022, ISSN: 1951-6401. DOI: 10.1140/epjs/s11734-022-00727-y. [Online]. Available: http://dx.doi.org/10.1140/epjs/s11734-022-00727-y.

[116] H. Song, Y. Wang, and K. Pant, "System-level simulation of liquid filling in microfluidic chips," *Biomicrofluidics*, vol. 5, no. 2, 2011.

[117] A. Olanrewaju, M. Beaugrand, M. Yafia, and D. Juncker, "Capillary microfluidics in microchannels: From microfluidic networks to capillaric circuits," *Lab on a Chip*, vol. 18, no. 16, pp. 2323–2347, 2018.

[118] S.-u. Hassan *et al.*, "Capillary-driven flow microfluidics combined with smartphone detection: An emerging tool for point-of-care diagnostics," *Diagnostics*, vol. 10, no. 8, p. 509, 2020.

[119] S. A. Mousavi Shaegh, N.-T. Nguyen, and S. Wereley, *Fundamentals and Applications of Microfluidics*. Feb. 2019.

[120] C.-Y. Lee, W.-T. Wang, C.-C. Liu, and L.-M. Fu, "Passive mixers in microfluidic systems: A review," *Chemical Engineering Journal*, vol. 288, pp. 146–160, 2016.

[121] B. E. Rapp, *Microfluidics: modeling, mechanics and mathematics*. William Andrew, 2016.

[122] J. Saliba, A. Daou, S. Damiati, J. Saliba, M. El-Sabban, and R. Mhanna, "Development of microplatforms to mimic the in vivo architecture of cns and pns physiology and their diseases," *Genes*, vol. 9, no. 6, p. 285, 2018.

[123] M. Saldana *et al.*, *The reynolds number: A journey from its origin to modern applications. fluids 2024, 9, 299*, 2024.

[124] J. R. Rumble, Ed., *CRC Handbook of Chemistry and Physics*, 104th. Boca Raton, FL: CRC Press, 2023, Viscosity of water at 20 °C: 1.002 mPa·s.

[125] J. C. McDonald and G. M. Whitesides, "Poly (dimethylsiloxane) as a material for fabricating microfluidic devices," *Accounts of chemical research*, vol. 35, no. 7, pp. 491–499, 2002.

[126] K. Brookshier and J. Tarbell, "Evaluation of a transparent blood analog fluid: Aqueous xanthan gum/glycerin," *Biorheology*, vol. 30, no. 2, pp. 107–116, 1993. DOI: 10.3233/BIR-1993-30202.

[127] D. Mann and J. Tarbell, "Flow of non-newtonian blood analog fluids in rigid curved and straight artery models," *Biorheology*, vol. 27, no. 5, pp. 711–733, 1990. DOI: 10.3233/BIR-1990-27508.

[128] L. Zhong, M. Oostrom, M. Truex, V. Vermeul, and J. Szecsody, "Rheological behavior of xanthan gum solution related to shear thinning fluid delivery for subsurface remediation," *Journal of Hazardous Materials*, vol. 244–245, pp. 160–170, Jan. 2013, ISSN: 0304-3894. DOI: 10.1016/j.jhazmat.2012.11.028. [Online]. Available: http://dx.doi.org/10.1016/j.jhazmat.2012.11.028.

[129] C. Completo, V. Geraldes, and V. Semiao, "Rheological and dynamical characterization of blood analogue flows in a slit," *International Journal of Heat and Fluid Flow*, vol. 46, pp. 17–28, Apr. 2014, ISSN: 0142-727X. DOI: 10.1016/j.ijheatfluidflow.2013.12.008. [Online]. Available: http://dx.doi.org/10.1016/j.ijheatfluidflow.2013.12.008.